Invited Research Article

Metasomatized eclogite xenoliths from the central Kaapvaal craton as probes of a seismic mid-lithospheric discontinuity

Katie A. Smart [a,*], Sebastian Tappe [b], Alan B. Woodland [c], Chris Harris [d], Loretta Corcoran [e], Antonio Simonetti [e]

[a] School of Geosciences, University of the Witwatersrand, Johannesburg 2050, South Africa
[b] Deep & Early Earth Processes (DEEP) Research Group, Department of Geology, University of Johannesburg, Auckland Park 2006, South Africa
[c] Institut für Geowissenschaften, Goethe-Universität, Frankfurt am Main 60438, Germany
[d] Department of Geological Sciences, University of Cape Town, Rondebosch 7701, South Africa
[e] Department of Civil and Environmental Engineering and Earth Sciences, University of Notre Dame, Notre Dame, IN 46556, USA

ARTICLE INFO

ABSTRACT

The central region of the Kaapvaal craton is relatively understudied in terms of its lithospheric mantle architecture, but is commonly believed to be significantly impacted by post-Archean magmatism such as the ca. 2056 Ma Bushveld large igneous event. We investigate a collection of 17 eclogite xenoliths from the Cretaceous Palmietfontein kimberlite at the Western Limb of the Bushveld Complex for their mineralogical compositions (major and trace elements, plus Fe^{3+} contents), as well as stable oxygen and radiogenic Pb isotopic compositions to gain further insights into the nature and evolution of the central Kaapvaal cratonic mantle lithosphere. New U/Pb age determinations on mantle-derived zircon yield a magma emplacement age of ca. 75 Ma for the Palmietfontein Group-1 kimberlite, which means that the entrained eclogite xenoliths may record a protracted metasomatic history from the Proterozoic through to most of the Phanerozoic eon.

Garnet $\delta^{18}O$ values of up to 6.9‰ and positive Eu anomalies for the bulk rocks suggest seawater-altered oceanic crustal protoliths for the Palmietfontein eclogite xenolith suite, which is typical for the eclogitic components of the Kaapvaal root and other cratonic mantle sections worldwide. However, several features of the Palmietfontein eclogites are commonly not observed in other mantle-derived eclogite xenolith suites. Firstly, the samples studied yield relatively low equilibration pressures and temperatures between 2.7 and 4.5 GPa and 740–1064 °C, indicating a relatively shallow residence between 90 and 150 km depths. Secondly, euhedral coarse amphibole is present in several eclogite nodules where it is in equilibrium with 'touching' garnet, supporting eclogite residence within the amphibole stability field at uppermost lithospheric mantle conditions. Thirdly, primary omphacitic clinopyroxene is often overgrown by diopside, and is significantly enriched in incompatible trace elements. The clinopyroxene is also characterized by elevated $^{206}Pb/^{204}Pb$ of 17.28–19.20 and $^{207}Pb/^{204}Pb$ of 15.51–16.27, and these Pb isotopic compositions overlap with those of Mesozoic Group-2 kimberlites from the Kaapvaal craton.

Our results show that eclogites reside at ~85 km depth beneath the central Kaapvaal craton as part of a layer that corresponds to an approximately 50 km thick seismically-detected mid-lithospheric discontinuity. Mid-lithospheric discontinuities have been interpreted as metasomatic fronts formed by focussed crystallization of hydrous mineral phases from enriched volatile-bearing melts, and as such the strongly overprinted amphibole-bearing eclogite xenoliths from Palmietfontein may represent a physical expression of such seismically anomalous metasomatic layer at mid-lithospheric depth. Our Pb isotope data suggest that the focussed metasomatism can be attributed to volatile-rich melts reminiscent of potassic Group-2 kimberlites, which have been invoked in MARID-style metasomatic overprinting of the lower lithospheric mantle beneath the western Kaapvaal craton. However, the relatively low fO_2 recorded by the Palmietfontein eclogites (minimum FMQ-4.5) suggests that the metasomatism at mid-lithospheric depth was less protracted compared to the more intensive and oxidizing metasomatism typically observed near the base of cratonic mantle roots. While it is possible that Proterozoic magmatic events were responsible for the focussed mid-lithospheric metasomatism of the Kaapvaal mantle, on

* Corresponding author.
  E-mail address: katie.smart2@wits.ac.za (K.A. Smart).

the basis of the Pb isotope constraints the Palmietfontein eclogites were most likely overprinted during ca. 120 Ma Group-2 kimberlite magmatism.

1. Introduction

Seismic discontinuities are detected globally in both the oceanic and continental lithospheric mantles, and are marked by a decrease in P- and S-wave velocities between ~50 to 160 km depths (Selway et al., 2015; Rader et al., 2015). Beneath the ocean basins, this velocity decrease occurs on average at depths of approximately 70 km (Rychert and Shearer, 2009) and is generally recognized as the lithosphere-asthenosphere boundary (Fisher et al., 2010). In cratonic settings that are underlain by thick mantle lithospheres lending stability for billion-year timescales, decreases in seismic velocity are found at mid-lithospheric depths between 60 and 160 km, with prominent decreases being detected between 80 and 100 km depths (Selway et al., 2015; Rader et al., 2015). The cratonic lithosphere-asthenosphere boundary can account for velocity decreases found at depths greater than 150 km (Fisher et al., 2010), but the origin of shallower "mid-lithospheric discontinuities" is less clear and the subject of much recent scientific debate (Aulbach et al., 2017a; Shaikh et al., 2020).

Seismic mid-lithospheric discontinuities have been attributed to (1) the presence of a melt-bearing layer, (2) elastically-accommodated grain boundary sliding, (3) seismic anisotropy, (4) abrupt Mg-Fe compositional changes, and (5) accumulation of low-velocity minerals such as amphiboles (Yuan and Romanowicz, 2010; Selway et al., 2015; Rader et al., 2015; Karato and Park, 2018; Thybo, 2006; Savage and Silver, 2008). Several recent studies have discussed the origins of mid-lithospheric discontinuities observed beneath continents and oceanic plateaus as "metasomatic fronts", resulting from focussed crystallization of carbonate, pyroxene, amphibole and phlogopite, which can account for the observed 3–10% drop in seismic velocity (Selway et al., 2015; Wölbern et al., 2012; Rader et al., 2015; Tharimena et al., 2016; Smart et al., 2019). The role of metasomatism in mid-lithospheric discontinuity development is based on several key pieces of evidence, including (1) the coincidence of the stability limit of pargasitic amphibole at mid-lithospheric discontinuity depths of ~90–110 km, equivalent to pressures of ~3 GPa (Selway et al., 2015; Niida and Green, 1999; Green et al., 2014), (2) the occurrence of low-velocity minerals in cratonic mantle-derived xenoliths that have calculated velocity contrasts equivalent to those observed for the mid-lithospheric discontinuity (Wölbern et al., 2012; Rader et al., 2015), and (3) the combination of results from experimental petrology and thermodynamic parameterization models, which support formation of hydrous minerals from volatile-bearing alkaline melts at mid-lithospheric depth (Aulbach et al., 2017a).

For the Kaapvaal craton of southern Africa, seismic lithospheric discontinuities are detected at depths of approximately 85 and 150 km, and are attributed to both seismic anisotropy and metasomatism-induced compositional 'layering' effects (Sodoudi et al., 2013; Wittlinger and Farra, 2007). The Kaapvaal lithospheric mantle is characterized by a prevailing refractory composition that resulted from extensive Archean melt depletion (Walker et al., 1989; Pearson et al., 1995a, 1995b; Simon et al., 2007; Shu et al., 2013), juxtaposed with pervasive metasomatic overprinting throughout its >3 billion-year evolution (Griffin et al., 2003; Lazarov et al., 2012; Shirey and Harris, 2004; Grégoire et al., 2003). Some of this metasomatic overprinting has been linked to major post-Archean mantle-derived magmatic events on the Kaapvaal craton, such as the ca. 2056 Ma Bushveld (e.g. Richardson and Shirey, 2008; Shirey and Harris, 2004) and ca. 180 Ma Karoo large igneous provinces (Rehfeldt et al., 2008); however, recurrent carbonatitic to kimberlitic low-volume magmatic events have also been argued as causes of cratonic mantle lithosphere re-enrichment (e.g., Grégoire et al., 2003; Shu and Brey, 2015; Tappe et al., 2021). The latter inference is supported by the fact that mantle xenoliths from the

Kaapvaal craton frequently exhibit mineralogical, geochemical and redox evidence of secondary enrichment by relatively oxidized $H_2O \pm CO_2$-bearing alkaline silica-poor melts (Huang et al., 2012; Grégoire et al., 2002; Jacob et al., 2009; Fitzpayne et al., 2019; Lazarov et al., 2009; Creighton et al., 2009; Woodland and Koch, 2003). This oxidative, volatile-rich metasomatism has both compositional and temporal links to widespread kimberlite magmatism on the Kaapvaal craton (Konzett et al., 1998; Giuliani et al., 2015), such as the prominent post-200 Ma pulses during the ca. 90 Ma Group-1 and 110–120 Ma Group-2 kimberlite magmatic events (Smith et al., 1985; Tappe et al., 2018a).

The phlogopite-rich Group-2 kimberlites, or "orangeites", are particularly noteworthy because of their markedly potassic character and distinctive Sr–Nd–Pb isotope signatures (Smith, 1983; Becker and le Roex, 2006). Mesozoic Group-2 kimberlite magmatism is often invoked as the driving force behind mantle metasome formation, as exemplified by formation of the "MARID" suite of xenoliths (composed of mica, amphibole, rutile, ilmenite and diopside; Dawson and Smith, 1977), which is coupled to distinctive elemental enrichments within the Kaapvaal peridotitic mantle lithosphere (e.g. Grégoire et al., 2003). The metasomatic MARID suite xenoliths, somewhat unique to the Kaapvaal craton, have overlapping Sr-Nd-Pb isotopic compositions and ages with the Group-2 kimberlites (Kramers et al., 1983; Grégoire, 2002; Konzett et al., 1998; Fitzpayne et al., 2019; Giuliani et al., 2015). Moreover, the chemical expression of this Group-2 kimberlite or MARID metasomatic event is likely responsible for distinctive Zr-Hf enrichments in certain mantle-derived materials that were brought to surface by subsequent pulses of ca. 90 Ma Group-1 kimberlites (Kobussen et al., 2012; Griffin et al., 2003). Also, the MARID metasomatic event is thought to have an oxidizing nature and it may have been responsible for the destruction of previously existing lithospheric diamonds (Creighton et al., 2009).

Here we investigate a suite of 17 metasomatized eclogite xenoliths and one zircon megacryst from the ca. 75 Ma Palmietfontein Group-1 kimberlite on the central Kaapvaal craton in South Africa. This poorly studied kimberlite is located at the western margin of the ca. 2056 Ma Bushveld Complex in close proximity to the ca. 1395 Ma Pilanesberg alkaline complex (Fig. 1). The Palmietfontein eclogite nodules are distinct from many other kimberlite-borne cratonic eclogite xenolith suites worldwide in their unusually shallow equilibration depths of <110 km, the presence of equilibrium amphibole, ubiquitous incompatible trace element enrichments and relatively radiogenic Pb isotopic compositions. Our results demonstrate that the Palmietfontein eclogite xenoliths have been strongly overprinted by Group-2 kimberlite or MARID-type metasomatism, and that this potassic melt-related mantle metasomatism had been focussed at the top of a known mid-lithospheric discontinuity within the Kaapvaal continental root.

2. Geologic setting

The ca. 75 Ma Palmietfontein Group-1 kimberlite is located approximately 150 km northwest of Johannesburg, South Africa, in the central region of the Kaapvaal craton (Jelsma et al., 2004; Da Costa, 1989; Fig. 1). The Palmietfontein kimberlite intrudes the southwest margin of the ca. 1395 Ma Pilanesburg alkaline complex (Elburg and Cawthorn, 2017), which is located at the western margin of the ca. 2056 Ma Bushveld Complex (Zeh et al., 2015), the largest known continental mafic-ultramafic layered intrusion. Relatively little is known about the lithospheric mantle of the central Kaapvaal craton, but seismic tomography of the craton has indicated that the mantle in the area of the 2056 Ma Bushveld complex underwent significant thermal and geochemical overprinting, most likely in response to the Proterozoic magmatic episode (Shirey and Harris, 2004). Currently, information is currently

limited to pressure-temperature arrays obtained from kimberlite-derived garnet xenocrysts (Kobussen et al. (2012)). For the Palmietfontein area, a pressure-temperature array based on 187 peridotitic garnet xenocrysts by Kobussen et al. (2012), using the Ni- and Cr-in-garnet thermobarometry method, places the LAB at approximately 175–200 km depths. Garnet xenocryst Ti contents and Mg-numbers indicate that the uppermost lithospheric mantle down to approximately 100 km depth is characterized by refractory harzburgitic compositions typical of depleted cratonic mantle. At >100 km depth, Zr-Ti-Fe-enriched lherzolitic compositions are found, possibly related to melt metasomatism during Group-2 kimberlite or MARID-style events (the so-called "phlogopite-style" metasomatism; Kobussen et al., 2012). Garnet xenocrysts from earlier Group-2 kimberlites on the central Kaapvaal craton, such as the ca. 140 Ma Swartruggens dykes, show similar trends of strong enrichments in Fe and Ti (but not Zr) with increasing depth (Kobussen et al., 2012). This regional pattern may reflect that the central Kaapvaal mantle lithosphere underwent melt metasomatism and associated Fe-addition possibly related to the Bushveld event, whereas phlogopite introduction occurred probably during the 140–120 Ma Group-2 kimberlite magmatic pulses (Kobussen et al., 2012), sampled subsequently by Group-1 kimberlite eruptions at 90–75 Ma.

3. Palmietfontein eclogite xenoliths petrography

Seventeen eclogite xenoliths were collected from the Palmietfontein kimberlite tailings dumps for petrographic and geochemical examination. The xenolith samples measure between 1 and 2 cm in the longest dimension and are medium- to coarse-grained with garnet crystals of up to 0.5 cm in diameter (excluding Palm-7 with fine- to medium-grained textures). The studied eclogite xenoliths feature dominantly massive interlocking textures (Fig. 2a-b). Several samples (Palm-7, −16, −22, −23) display layered and foliated textures (Fig. 2c). Palm-13 contains significant garnet exsolution in clinopyroxene (Figure A1). The eclogites are composed primarily of sub-equal amounts of garnet and clinopyroxene, but samples Palm-10, −12 and − 18 contain between 5 and 10 vol% euhedral amphibole, which forms part of the interlocking texture suggestive of textural equilibrium with surrounding garnet and clinopyroxene (Fig. 2b; Figure A1). Some eclogite samples (Palm-6, −8, −10, −13, −14) contain secondary diopside occurring as irregular rims and overgrowths on primary omphacitic clinopyroxene (Table 1; Figure A1). Trace amounts of rutile, nepheline (Palm-7), sulphide and calcite (Palm-23, −24, −28) were also observed.

4. Methods

4.1. Zircon U-Pb geochronology

In situ zircon U/Pb isotope ratio measurements were performed by laser ablation multi-collector inductively coupled plasma mass spectrometry (LA-MC-ICP-MS) at the Department of Geology, University of Johannesburg, in October 2017. The LA-MC-ICP-MS setup consists of a RESOlution SE 193 nm excimer laser ablation system (Australian Scientific Instruments) that is coupled to a Nu Plasma-II mass spectrometer (Nu Instruments, U.K.). The sensitivity of the MC-ICP-MS instrument
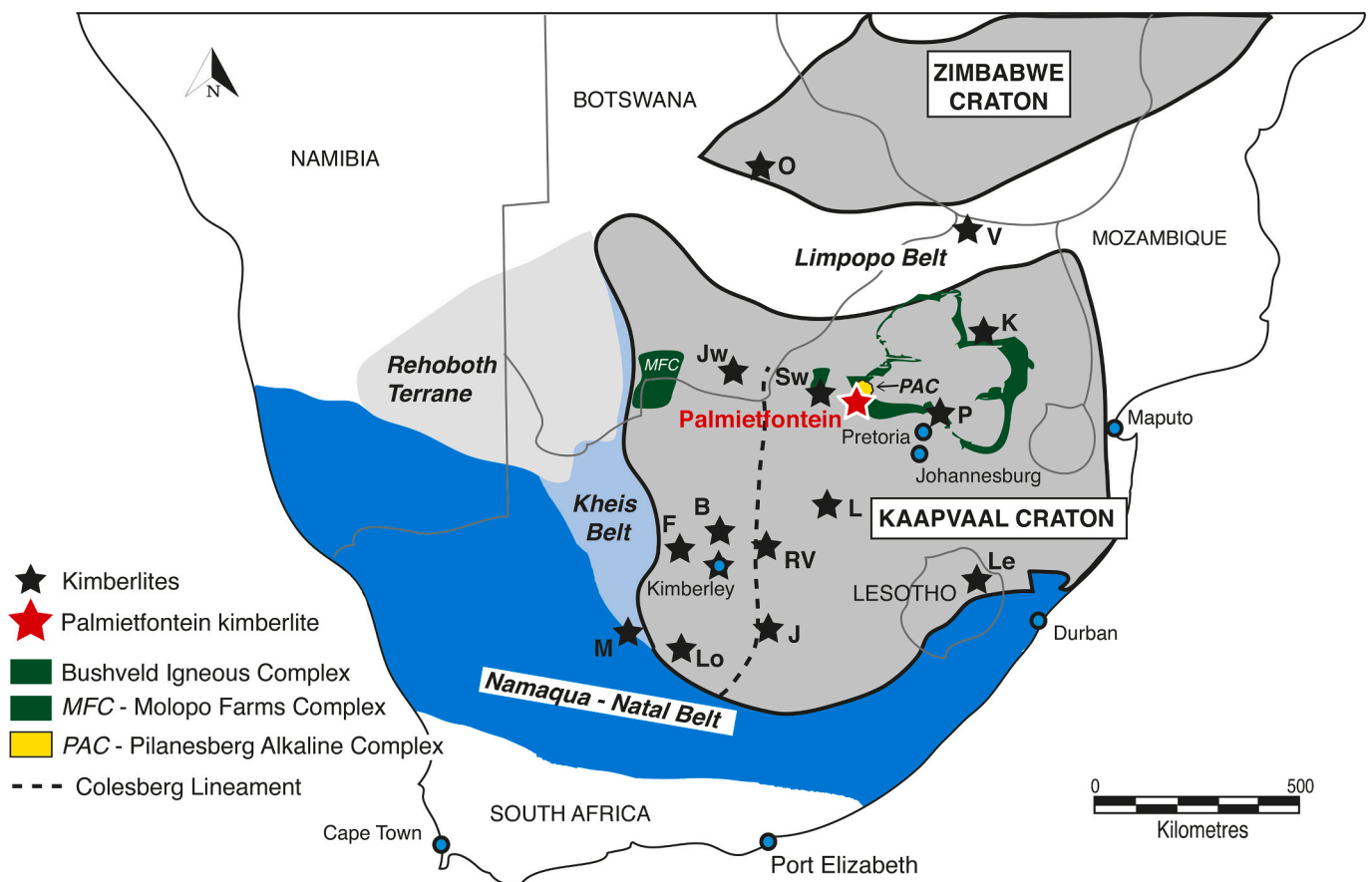
Fig. 1. Simplified geologic map of the Kaapvaal and Zimbabwe cratons, with surrounding Archean to Proterozoic terranes, showing the occurrence of the 75 Ma Palmietfontein kimberlite in the eastern half of the Kaapvaal craton. The Palmietfontein kimberlite is located at the western margin of both the ~2.1 Ga Bushveld and ~ 1.4 Ga Pilanesberg igneous complexes. The locations of select kimberlites are shown with black stars, including: O, Orapa; V, Venetia; Jw, Jwaneng; K, Klipspringer; Sw, Swartruggens; P, Premier; L, Lace; RV, Roberts Victor; B, Bellsbank; F, Finsch; J, Jagersfontein; Le, Letsang; M, Markt; Lo, Lovedale. Map is redrawn after Burness et al. (2020).

Fig. 2. Images of representative Palmietfontein eclogite xenoliths. **(a) Palm-8** shows medium-grained interlocking pink-red garnet and pale green clinopyroxene. **(b) Palm-10** is medium-grained and contains dark green-brown amphibole that has interlocking grain boundaries with red-orange garnet and forest-green clinopyroxene. **(c) Palm-7** displays a banded, fine-grained texture with alternating layers of orange garnet- 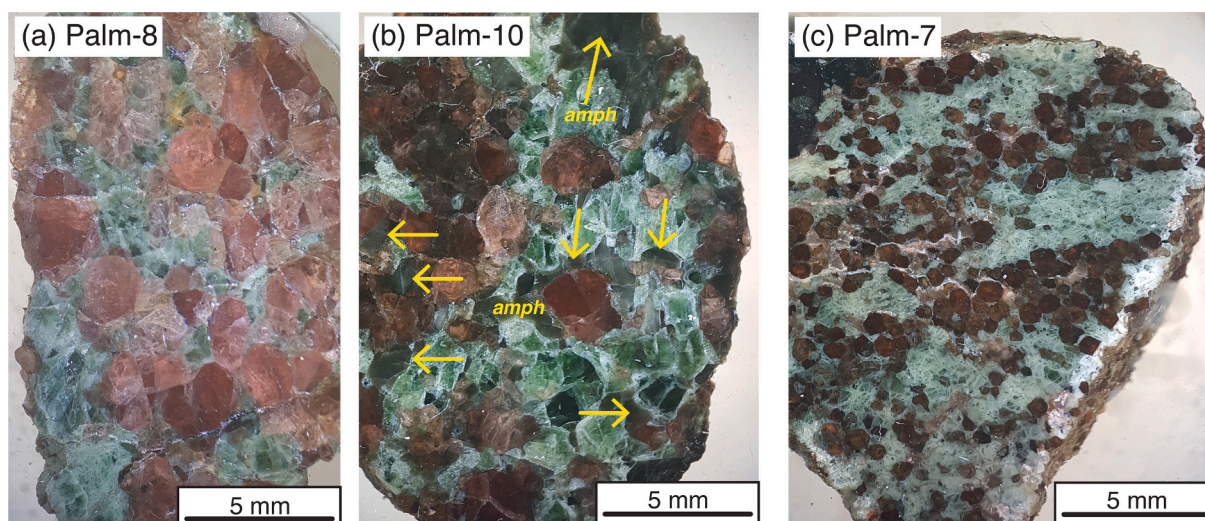and altered whitish-coloured clinopyroxene. (For interpretation of the references to colour in this figure legend, the reader is referred to the web version of this article.)

was optimized during continuous 35 μm wide line ablations on an in-house zircon standard applying a laser energy of 4 mJ and a 4 Hz repetition rate at a scan speed of 0.003 mm/s. Sample ablations were performed within a polished epoxy grain mount in a Laurin Technic dual-volume cell under a helium atmosphere (0.25 l/min gas flow). The helium sample gas was mixed with argon carrier gas (0.80 l/min gas flow) prior to entering the plasma-generating torch of the ICP-MS instrument.

Approximately 100 μm wide ablation pits were drilled with the excimer laser at a relatively low laser fluence of 1.17 J/cm^2, equivalent to a nominal energy of <4 mJ at an attenuator setting of 12.5%. This conservative setting was selected to reduce laser induced element fractionation. Background ion signal levels ('blank') were measured on-peak for 20 s prior to ablation. Natural zircon mineral standards and the unknowns were ablated and analyzed for 50 s applying identical analytical conditions. The integration time was set to 0.2 s. Prior to each spot measurement, grain surfaces were 'cleaned' with two pre-ablation laser pulses. The intensities of the ^{238}U (H8) and ^{232}Th (H7) ion beams were measured with Faraday detectors, whereas atomic masses ^{208}Pb (IC0), ^{207}Pb (IC1), ^{206}Pb (IC2), ^{204}Pb + ^{204}Hg (IC3), and ^{202}Hg (IC4) were measured with ion counters. Ion counter signals were kept significantly below 10^7 counts per second to protect the multipliers from excessive beams and to ensure linearity with the Faraday cups (Simonetti et al., 2006). Calculations of isotope ratios and U-Th-Pb ages were performed with reference to two primary zircon calibration standards (GJ-1 of Jackson et al., 2004; and Plesovice of Slama et al., 2008) using a standard-sample- bracketing approach (i.e., 5 calibration standard analyses before and after 10 to 15 unknowns) and VB Excel based in-house data reduction software. The Excel 'Add-In' Isoplot (v. 4.15) was used for age calculations and data visualization. The recommended decay constants of 4.9475 × 10^{-11} a^{-1} for ^{232}Th, 9.8485 × 10^{-10} a^{-1} for ^{235}U, and 1.55125 × 10^{-10} a^{-1} for ^{238}U were applied (Steiger and Jäger, 1977).

The presence of common lead in excess of the ^{204}Pb baseline level, as determined by repeated measurements of GJ-1 and Plesovice zircon standards, was corrected using the terrestrial lead isotope evolution model of Stacey and Kramers (1975). Accurate and precise ^{204}Pb measurements were achieved by monitoring of ^{202}Hg, which allowed for corrections of small isobaric interferences of ^{204}Hg on ^{204}Pb as typically encountered in LA-ICP-MS studies (Storey et al., 2006; Tappe and Simonetti, 2012). Temora-2 zircon served as an independent secondary

standard to assess data quality. During the analytical session on 17 October 2017, four spot measurements of Temora-2 zircon yielded a weighted average ^{206}Pb/^{238}U age of 406.4 ± 7.2 Ma (2-sigma), which is in agreement with the recommended crystallization age of 416.1 ± 1.2 Ma (Black et al., 2004).

4.2. Mineral major and minor element analyses

Quantitative mineral chemical analyses were obtained for garnet, clinopyroxene, and amphibole using a JEOL JXA-8230 electron probe micro-analyzer (EPMA) at Rhodes University, South Africa, in 2015. Operating conditions were adjusted to 15 kV accelerating potential, 15 nA beam current, and 10 μm electron beam spot size. All elements of interest were measured on K-alpha peaks, with peak and background counting times of 10 s. Instrument calibration was done using commercial SPI standards including kaersutite (Fe), Cr-metal (Cr), plagioclase (Ca), albite (Na), almandine (Fe, Al, Mg, Si), rutile (Ti), and rhodonite (Mn). The data were collected with JEOL software and an automated ZAF matrix algorithm was applied to correct for differential matrix effects. EPMA-determined mineral compositions are presented in Table 2 and Table A1.

4.3. Mineral trace element analyses

In-situ trace element compositions of garnet, clinopyroxene and amphibole were obtained using laser ablation inductively coupled plasma mass spectrometry (LA-ICP-MS) at the Central Analytical Facility of Stellenbosch University in 2015. A 193 nm Resonetics Resolution S155 laser system coupled to an Agilent 7500ce quadrupole ICP-MS instrument was employed using a spot diameter of 100 μm. The internal standard was ^{29}Si, and external calibration was conducted by analysing the NIST SRM 612 standard reference glass (n = 15) every 10 unknowns. The data were reduced off-line using the GLITTER software package (Van Achterbergh et al., 2001). Mineral trace element compositions are presented in Table 3 (garnet and clinopyroxene) and Table A1 (amphibole). The measured NIST 612 SRM values have standard errors of 1.1–3.6%, relative, median lower limits of detection of 0.007 ppm, and differ from the NIST 612 values reported by Jochum et al. (2011) by less than 5.6% (reported in Table A2).

Table 1

U-Th-Pb isotope systematics of mantle zircon ST17-50-1 from the Palmietfontein kimberlite, central Kaapvaal craton, South Africa (−25.3058 S, 26.9558 E).

Zircon	Run – ID	$U[ppm]$	$Th[ppm]$	$^{206}Pb/^{204}Pb$	$^{207}Pb/^{206}Pb$	ISE	$^{208}Pb/^{206}Pb$	ISE	$^{207}Pb/^{235}U$	ISE	$^{206}Pb/^{238}U$	ISE	Rho	$^{208}Pb/^{232}Th$	ISE	207/206	ISE	207/235	ISE	206/238	ISE	208/232	ISE	$^{238}U/^{206}Pb$	ISE	$^{207}Pb/^{206}Pb$	ISE
Palmietfontein (ST17-50-1)	#1	6	0.3	6	0.05331	0.00267	0.01905	0.00158	0.08782	0.00461	0.01195	0.00019	0.295	0.00403	0.00013	342	111	85	4	77	1	81	3	83.706	1.297	0.05331	0.00267
Palmietfontein (ST17-50-1)	#2	6	0.4	6	0.05315	0.00241	0.01878	0.00157	0.08686	0.00414	0.01185	0.00017	0.309	0.00386	0.00013	335	105	85	4	76	1	78	3	84.377	1.242	0.05315	0.00241
Palmietfontein (ST17-50-1)	#3	6	0.3	6	0.05107	0.00243	0.01686	0.00145	0.08313	0.00415	0.01181	0.00018	0.302	0.00347	0.00013	244	108	81	4	76	1	70	3	84.703	1.275	0.05107	0.00243
Palmietfontein (ST17-50-1)	#4	7	0.4	6	0.05488	0.00253	0.0192	0.00153	0.08741	0.00426	0.01155	0.00018	0.319	0.00376	0.00012	407	100	85	4	74	1	76	2	86.570	1.344	0.05488	0.00253
Palmietfontein (ST17-50-1)	#5	8	0.4	7	0.05315	0.00239	0.01827	0.00154	0.08446	0.00402	0.01152	0.00018	0.325	0.00366	0.00011	335	101	82	4	74	1	74	2	86.769	1.344	0.05315	0.00239
Palmietfontein (ST17-50-1)	#6	7	0.4	6	0.05765	0.00275	0.01859	0.00164	0.09164	0.00464	0.01153	0.00019	0.328	0.00365	0.00016	516	105	89	4	74	1	74	3	86.738	1.439	0.05765	0.00275
Palmietfontein (ST17-50-1)	#7	8	0.5	6	0.0536	0.00237	0.02111	0.00163	0.08639	0.00406	0.01169	0.00018	0.334	0.00406	0.00011	354	94	84	4	75	1	82	2	85.543	1.342	0.05360	0.00237
Palmietfontein (ST17-50-1)	#8	8	0.5	7	0.05855	0.00284	0.02371	0.00208	0.09593	0.00486	0.01188	0.00017	0.29	0.00469	0.00017	550	99	93	5	76	1	94	3	84.159	1.236	0.05855	0.00284
Palmietfontein (ST17-50-1)	#9	8	0.5	7	0.05183	0.0023	0.02039	0.00176	0.08228	0.00387	0.01151	0.00018	0.33	0.00408	0.00013	278	103	80	4	74	1	82	3	86.851	1.346	0.05183	0.00230
Palmietfontein (ST17-50-1)	#10	17	1	16	0.05266	0.00224	0.01829	0.00157	0.08488	0.00384	0.01169	0.00018	0.339	0.00369	0.00009	314	95	83	4	75	1	74	2	85.535	1.312	0.05266	0.00224
Palmietfontein (ST17-50-1)	#11	6	0.3	6	0.05186	0.0023	0.01709	0.00146	0.08529	0.00401	0.01193	0.00019	0.33	0.00356	0.00012	279	103	83	4	76	1	72	2	83.831	1.301	0.05186	0.00230
Palmietfontein (ST17-50-1)	#12	7	0.4	6	0.0528	0.00229	0.01882	0.00154	0.08632	0.004	0.01186	0.00019	0.347	0.0038	0.00013	320	100	84	4	76	1	77	3	84.328	1.356	0.05280	0.00229
Palmietfontein (ST17-50-1)	#13	6	0.4	6	0.05032	0.00236	0.01797	0.0016	0.08207	0.00407	0.01183	0.00019	0.327	0.00372	0.00014	210	110	80	4	76	1	75	3	84.532	1.372	0.05032	0.00236
Palmietfontein (ST17-50-1)	#14	7	0.4	6	0.05246	0.00298	0.02093	0.00215	0.0851	0.00502	0.01177	0.00019	0.27	0.00433	0.00029	306	123	83	5	75	1	87	6	84.994	1.356	0.05246	0.00298
Palmietfontein (ST17-50-1)	#15	10	0.7	10	0.05019	0.00211	0.0213	0.00168	0.08071	0.00363	0.01166	0.00018	0.351	0.00369	0.00009	204	98	79	3	75	1	74	2	85.744	1.354	0.05019	0.00211
Palmietfontein (ST17-50-1)	#16	9	0.6	9	0.05143	0.00226	0.02121	0.00177	0.08278	0.00387	0.01167	0.00019	0.341	0.00383	0.00011	260	99	81	4	75	1	77	2	85.655	1.364	0.05143	0.00226
Palmietfontein (ST17-50-1)	#17	9	0.6	9	0.0539	0.00243	0.02234	0.00184	0.08764	0.00418	0.01179	0.00018	0.325	0.00389	0.00011	367	100	85	4	76	1	78	2	84.799	1.313	0.05390	0.00243
Palmietfontein (ST17-50-1)	#18	10	0.6	10	0.05458	0.00444	0.02118	0.00295	0.08885	0.00738	0.01181	0.0002	0.201	0.00398	0.00046	395	175	86	7	76	1	80	9	84.692	1.417	0.05458	0.00444
Palmietfontein (ST17-50-1)	#19	10	0.7	8	0.05094	0.00212	0.0204	0.00166	0.08233	0.00367	0.01172	0.00019	0.362	0.00355	0.00009	238	94	80	3	75	1	72	2	85.319	1.375	0.05094	0.00212
Palmietfontein (ST17-50-1)	#20	10	0.6	9	0.02625	0.00142	0.00815	0.00078	0.04068	0.00229	0.01124	0.00018	0.28	0.00143	0.00009							72	1	88.981	1.401	0.02625	0.00142
*Temora-2	#1	200	28	845	0.05613	0.00231	0.04498	0.00404	0.49995	0.02225	0.06461	0.0011	0.383	0.02066	0.00049	457	86	412	15	404	7	413	10	15.479	0.264	0.05613	0.00231
*Temora-2	#2	249	25.2	1021	0.05588	0.00229	0.03261	0.00334	0.5015	0.02224	0.06509	0.0011	0.382	0.02082	0.00049	448	89	413	15	407	7	417	10	15.363	0.260	0.05588	0.00229
*Temora-2	#3	296	40.5	1252	0.05694	0.00237	0.04581	0.00482	0.51808	0.02368	0.06599	0.00124	0.412	0.02191	0.00057	489	89	424	16	412	8	438	11	15.153	0.285	0.05694	0.00237
*Temora-2	#4	250	26.6	992	0.05625	0.00233	0.03481	0.00374	0.50209	0.02278	0.06474	0.00121	0.411	0.02099	0.00054	462	89	413	15	404	7	420	11	15.447	0.288	0.05625	0.00233

Table 2
Major and minor element composition of garnet and clinopyroxene from Palmietfontein eclogite xenoliths.

	Palm-2	Palm-6	Palm-7	Palm-8	Palm-10	Palm-12	Palm-13	Palm-14	Palm-15	Palm-16	Palm-17	Palm-18	Palm-20	Palm-22	Palm-23	Palm-24	Palm-28
main phases:	grt + cpx	grt + cpx	grt + cpx	grt + cpx	grt + cpx + 10% amph	grt + cpx + 5% amph	grt + cpx	grt + cpx	grt + cpx	grt + cpx	grt + cpx	grt + cpx + 5% amph	grt + cpx	grt + cpx	grt + cpx	grt + cpx	grt + cpx
trace phases:		2nd diopside	rt; neph	2nd diopside	2nd diopside	rt	2nd diopside; rt	2nd diopside	sulph	amph		rt			cc; suplh	cc	rt; cc
Texture and comments:	massive	massive	layered & foliated; altered cpx	massive; altered	massive; euhedral amph	massive; euhedral amph	massive; thick cpx rims; 2nd grt exsolution	massive; thick cpx rims	massive	foliated	massive; altered	massive; euhedral amph	massive	foliated	foliated	massive	massive
	Grt	**Grt**	**Grt**	**Grt**	**Grt**	**Grt**	**Grt**	**Grt**	**Grt**	**Grt**	**Grt**	**Grt**	**Grt**	**Grt**	**Grt**	**Grt**	**Grt**
SiO_2	41.7	41.3	38.9	41.6	41.1	41.6	40.8	40.6	40.9	40.6	40.7	41.7	41.0	40.7	40.4	40.2	41.4
TiO_2	0.05	0.03	0.06	0.03	0.04	0.06	0.04	0.07	0.04	0.07	0.03	0.06	0.02	0.05	0.05	0.06	0.04
Al_2O_3	22.7	23.0	21.6	23.3	22.7	23.1	22.7	22.6	22.7	22.7	22.8	23.2	22.9	22.8	22.6	22.4	23.1
Cr_2O_3	0.06	0.09	0.03	0.05	0.18	0.21	0.02	0.11	0.19	0.13	0.11	0.22	0.05	0.04	0.06	0.07	0.09
FeO	15.7	13.1	21.6	13.7	15.6	12.6	15.3	14.6	15.2	13.7	14.5	12.8	17.6	13.1	16.4	16.9	12.2
MnO	0.36	0.32	0.56	0.29	0.44	0.35	0.38	0.34	0.33	0.34	0.28	0.34	0.4	0.32	0.44	0.46	0.34
MgO	13.7	16.8	7.92	17.3	15.3	18.0	15.3	11.3	14.5	14.9	14.0	17.9	14.3	13.5	12.6	10.8	17.8
CaO	7.26	5.04	8.26	4.30	4.74	3.93	4.69	10.4	5.75	6.5	6.91	3.94	4.17	8.61	6.87	8.88	4.33
Na_2O	0.01	0.01	0.007	0.005	bd	0.01	bd	0.01	bd	0.01	0.01	0.01	0.01	bd	0.01	0.01	bd
Total	99.4	99.6	99.0	100.5	100.1	99.8	99.3	99.9	99.5	98.9	99.4	100.2	100.5	99.2	99.3	99.7	99.3
Mg#	0.61	0.70	0.40	0.69	0.64	0.72	0.64	0.58	0.63	0.66	0.63	0.71	0.59	0.65	0.58	0.53	0.72
Ca#	0.19	0.13	0.23	0.11	0.12	0.10	0.12	0.27	0.15	0.17	0.18	0.10	0.11	0.23	0.18	0.24	0.11
$Fe^{3+}/\sum Fe$*	0.015	0.017	0.036	0.023	0.018		0.026	0.014	0.016	0.019	0.009	0.021	0.017	0.023	0.015	0.017	0.020
Garnet Class.	high-Mg	high-Mg	high-Ca	high-Mg	high-Mg	high-Mg	high-Mg	high-Ca	high-Mg	high-Mg	high-Mg	high-Mg	low-Mg	high-Ca	low-Mg	high-Ca	high-Mg
	Palm-2	Palm-6	Palm-7	Palm-8	Palm-10	Palm-12	Palm-13	Palm-14	Palm-15	Palm-16	Palm-17	Palm-18	Palm-20	Palm-22	Palm-23	Palm-24	Palm-28
	Cpx	**Cpx**	**Cpx**	**Cpx**	**Cpx**	**Cpx**	**Cpx**	**Cpx**	**Cpx**	**Cpx**	**Cpx**	**Cpx**	**Cpx**	**Cpx**	**Cpx**	**Cpx**	**Cpx**
SiO_2	54.5	54.5	55.0	55.2	54.7	54.9	54.6	54.3	54.5	54.2	54.9	55.0	55.1	54.2	54.4	54.3	54.5
TiO_2	0.26	0.26	0.16	0.24	0.12	0.25	0.24	0.34	0.23	0.30	0.22	0.24	0.21	0.29	0.26	0.29	0.23
Al_2O_3	8.57	7.72	11.15	7.41	5.15	5.40	6.61	11.53	6.39	7.83	9.60	5.41	6.58	8.75	7.35	8.55	4.63
Cr_2O_3	0.09	0.13	0.03	0.09	0.20	0.23	0.06	0.10	0.27	0.13	0.14	0.21	0.07	0.09	0.05	0.09	0.15
FeO	3.08	3.03	4.47	3.23	3.71	3.12	3.78	3.26	3.60	3.07	2.44	3.19	4.52	2.69	3.84	3.94	2.65
MnO	0.02	0.02	0.03	0.03	0.04	0.04	0.03	0.02	0.03	0.03	0.02	0.04	0.04	0.02	0.04	0.02	0.04
MgO	11.7	12.2	8.43	12.6	13.8	14.0	12.6	9.47	12.7	14.3	11.1	14.0	12.3	11.8	11.9	11.1	14.6
CaO	17.0	17.0	13.3	16.8	19.4	18.5	17.6	14.8	18.0	17.3	16.3	18.5	16.8	17.4	17.4	16.8	19.9
Na_2O	4.43	4.25	6.52	4.21	2.87	3.22	3.85	5.75	3.64	4.18	4.76	3.15	4.17	4.22	3.98	4.53	2.62
Total	99.5	99.1	99.1	99.8	99.9	99.7	99.4	99.6	99.4	98.9	99.5	100.2	100.5	99.4	99.3	99.6	99.3
Mg#	87	88	77	87	87	89	86	84	86	89	89	89	83	89	85	83	91
Jd	0.29	0.28	0.44	0.28	0.19	0.20	0.26	0.38	0.24	0.27	0.31	0.20	0.28	0.28	0.26	0.30	0.17

Mg# = Mg/(Mg + total Fe) and Ca# = Ca/(Ca + Mg + total Fe + Mn) calculated using molar cation abundances; bd = below detection; * determined by Mössbauer spectroscopy, overall errors are ±0.01.
Grt = garnet; cpx = clinopyroxene; amph = amphibole; cc = calcite; rt. = rutile; neph = nepheline; sulph = sulphide.
Garnet classification discussed in section 5.2 and Fig. 4.
Major element contents in wt%.

Table 3

Trace element compositions of garnet and clinopyroxene from Palmietfontein eclogite xenoliths.

	Palm-2	Palm-6	Palm-7	Palm-8	Palm-10	Palm-12	Palm-13	Palm-14	Palm-15	Palm-16	Palm-17	Palm-18	Palm-20	Palm-22	Palm-23	Palm-24	Palm-28
	Grt	Grt	Grt	Grt	Grt	Grt	Grt	Grt	Grt	Grt	Grt	Grt	Grt	Grt	Grt	Grt	Grt
V	56	50	158	43	53	55	65	80	89	53	43	67	52	49	127	151	60
Ni	11.9	14.5	5.2	14.9	11.8	8.8	9.2	5.8	13.7	13.0	23.1	16.0	13.7	14.3	4.0	3.8	19.6
Sc	69	51	45	43	56	47	48	68	52	67	47	54	64	58	81	70	40
Rb	0.05	0.04	0.04	0.03	bd	bd	0.06	0.01	0.09	0.05	0.04	bd	0.03	bd	0.36	0.04	bd
Ba	0.04	bd	bd	bd	bd	0.05	bd	0.03	0.06	0.09	0.06	0.05	0.03	0.08	0.25	0.04	0.12
Th	0.003	0.01	0.003	0.004	0.01	0.01	0.003	0.003	0.003	0.01	0.01	0.005	0.01	0.01	0.06	0.02	0.01
U	0.02	0.01	0.002	0.01	0.05	0.01	0.01	0.06	0.01	0.04	0.02	0.05	0.02	0.03	0.11	0.05	0.01
Nb	0.02	0.03	0.004	0.004	0.01	bd	bd	0.03	0.02	0.03	0.06	0.01	0.004	0.01	0.18	0.04	0.01
Ta	bd	0.004	0.002	bd	bd	0.002	bd	0.001	0.001	0.002	0.002	0.001	0.02	0.001	0.01	0.002	0.004
La	0.01	0.01	0.002	0.01	0.01	0.01	0.01	0.01	0.01	0.02	0.01	0.01	0.02	0.02	0.18	0.02	0.01
Ce	0.11	0.10	0.02	0.04	0.10	0.10	0.07	0.15	0.08	0.19	0.05	0.15	0.09	0.17	0.56	0.20	0.11
Pr	0.03	0.05	0.03	0.02	0.02	0.04	0.04	0.09	0.02	0.04	0.02	0.05	0.04	0.05	0.13	0.11	0.03
Pb	0.02	0.01	0.02	bd	bd	0.01	bd	bd	0.01	0.02	0.02	0.02	0.02	0.01	bd	0.02	0.10
Sr	0.14	0.15	0.10	0.09	0.05	0.10	0.10	0.50	0.14	0.16	0.05	0.18	0.13	0.24	0.39	0.33	0.27
Nd	0.40	0.71	0.93	0.15	0.31	0.39	0.31	1.29	0.27	0.36	0.18	0.55	0.42	0.61	1.62	1.64	0.35
Sm	0.36	0.61	2.58	0.21	0.44	0.69	0.31	1.06	0.23	0.27	0.42	0.54	0.47	0.44	1.61	1.78	0.39
Zr	1.0	2.9	3.6	3.9	0.8	11.7	1.3	6.3	3.6	1.2	2.5	1.9	1.7	2.5	7.5	3.9	5.6
Hf	0.02	0.06	0.11	0.05	0.02	0.10	0.02	0.08	0.04	0.03	0.03	0.03	0.01	0.04	0.06	0.03	0.06
Eu	0.23	0.44	1.32	0.20	0.25	0.36	0.19	0.52	0.21	0.23	0.24	0.33	0.33	0.36	0.86	0.86	0.34
Ti	289	230	432	187	143	279	258	367	226	260	232	375	543	297	291	348	316
Gd	0.9	1.3	5.4	1.4	1.2	2.1	0.8	2.5	0.9	0.7	1.1	1.3	1.3	1.0	3.8	3.6	1.3
Tb	0.20	0.25	0.94	0.40	0.31	0.59	0.26	0.59	0.21	0.21	0.18	0.24	0.36	0.20	0.94	0.74	0.28
Dy	1.8	1.8	6.8	3.4	2.7	5.7	2.2	5.7	2.0	1.8	1.3	1.8	3.4	1.6	8.2	6.3	2.2
Y	12	11	37	22	17	38	16	40	15	12	7	10	26	9	57	42	13
Ho	0.47	0.42	1.41	0.81	0.64	1.44	0.54	1.46	0.54	0.43	0.29	0.42	0.97	0.35	2.10	1.57	0.49
Er	1.4	1.2	3.8	2.6	1.8	4.6	1.9	5.0	1.9	1.5	0.8	1.2	3.4	1.0	7.1	5.0	1.4
Tm	0.21	0.19	0.53	0.40	0.29	0.72	0.32	0.83	0.31	0.23	0.12	0.18	0.56	0.15	1.20	0.83	0.21
Yb	1.6	1.3	3.4	2.8	2.0	5.0	2.4	6.1	2.4	1.6	0.8	1.3	4.2	1.0	9.2	6.2	1.4
Lu	0.24	0.17	0.45	0.40	0.29	0.74	0.36	0.95	0.39	0.26	0.14	0.20	0.67	0.16	1.49	0.98	0.21
Eu*	1.17	1.49	1.06	0.82	0.97	0.84	1.12	0.94	1.26	1.46	1.07	1.14	1.19	1.67	1.02	1.01	1.33
Lu/Gd	2.15	1.12	0.67	2.31	1.94	2.81	3.72	3.09	3.65	2.87	1.05	1.23	4.10	1.32	3.14	2.20	1.32

	Palm-2	Palm-6	Palm-7	Palm-8	Palm-10	Palm-12	Palm-13	Palm-14	Palm-15	Palm-16	Palm-17	Palm-18	Palm-20	Palm-22	Palm-23	Palm-24	Palm-28
	Cpx	Cpx	Cpx	Cpx	Cpx	Cpx	Cpx	Cpx	Cpx	Cpx	Cpx	Cpx	Cpx	Cpx	Cpx	Cpx	Cpx
V	418	408	389	442	480	431	465	688	878	416	349	418	568	368	975	1052	342
Ni	256	259	174	321	279	154	192	96	280	270	424	313	288	271	83	80	376
Sc	26	20	26	20	32	29	23	22	25	24	16	20	34	20	43	32	22
Rb	0.05	0.03	0.19	0.03	0.02	0.07	bd	0.01	0.01	0.28	0.03	0.02	0.03	0.02	0.16	0.1	0.04
Ba	0.1	0.1	0.1	0.1	0.3	0.3	0.1	0.1	0.4	0.1	0.1	0.4	bd	bd	0.6	0.2	0.2
Th	0.11	0.37	bd	0.52	0.36	0.81	0.27	0.03	0.11	0.15	0.09	0.29	0.17	0.06	0.13	0.07	0.76
U	0.12	0.06	bd	0.14	0.08	0.08	0.11	0.05	0.07	0.14	0.05	0.14	0.05	0.06	0.12	0.10	0.09
Nb	0.61	0.02	0.01	0.02	0.07	0.01	0.03	0.42	0.04	0.51	bd	0.10	0.02	0.02	0.26	0.22	0.07
Ta	0.035	0.002	bd	bd	0.007	0.014	0.002	0.012	0.002	0.023	0.003	0.003	bd	bd	0.008	0.005	bd
La	3.3	5.5	bd	8.5	7.5	17.1	8.0	0.9	4.8	3.2	1.5	7.2	8.3	3.2	4.9	3.0	14.2
Ce	10	19	bd	20	16	37	20	3.1	14	8.7	3.5	18	22	8.5	19	12	35
Pr	1.4	3.0	bd	2.1	2.0	4.1	2.6	0.6	1.6	1.3	0.4	2.0	2.8	1.1	3.3	2.0	3.9
Pb	1.3	1.6	0.3	2.3	3.3	1.8	2.0	1.0	1.9	1.9	0.7	1.8	2.1	1.4	2.0	1.0	1.3
Sr	248	410	72	509	422	490	407	291	352	227	125	438	404	279	340	301	475
Nd	6.1	12.7	0.3	7.1	8.2	16.6	11.0	3.1	5.1	4.4	1.8	6.9	11.2	4.3	16.3	10.1	14.0
Sm	1.1	1.9	0.2	1.2	1.6	3.6	1.8	0.6	0.7	0.7	0.6	1.2	1.8	0.6	2.9	2.0	2.2
Zr	6	11	13	22	6	72	12	10	16	4	12	9	12	6	23	15	32
Hf	0.2	0.4	1.5	0.9	0.2	2.4	0.4	0.6	0.7	0.2	0.5	0.2	0.5	0.3	0.8	0.4	1.0
Eu	0.31	0.62	0.10	0.43	0.47	1.0	0.48	0.17	0.25	0.23	0.17	0.33	0.56	0.21	0.65	0.47	0.79
Ti	1785	1764	1045	1911	1075	1715	1615	2452	1586	1773	1402	2039	1467	1972	1902	1995	1487
Gd	0.6	1.0	0.3	1.3	1.2	3.0	1.1	0.5	0.5	0.5	0.4	0.8	1.2	0.3	1.7	1.2	1.5
Tb	0.06	0.08	0.08	0.15	0.14	0.34	0.10	0.05	0.05	0.04	0.04	0.06	0.14	0.03	0.16	0.11	0.15
Dy	0.3	0.3	0.5	0.7	0.6	1.6	0.4	0.3	0.2	0.2	0.1	0.2	0.6	0.1	0.8	0.5	0.6
Y	0.7	0.8	1.7	2.0	1.6	4.9	1.2	1.2	0.9	0.6	0.3	0.7	2.0	0.3	2.6	1.6	1.3
Ho	0.03	0.03	0.07	0.09	0.06	0.20	0.06	0.05	0.04	0.03	0.01	0.03	0.08	0.02	0.10	0.06	0.07
Er	0.05	0.05	0.14	0.16	0.13	0.37	0.08	0.11	0.07	0.04	0.02	0.04	0.16	0.02	0.22	0.12	0.10
Tm	0.004	0.01	0.02	0.01	0.01	0.03	0.01	0.01	0.01	0.01	0.002	0.004	0.01	0.002	0.02	0.01	0.01
Yb	0.03	0.02	0.05	0.08	0.06	0.15	0.03	0.06	0.04	0.08	0.02	0.02	0.07	0.01	0.11	0.05	0.04
Lu	0.004	0.002	0.009	0.006	0.005	0.01	0.004	0.009	0.005	0.002	bd	0.003	0.009	0.003	0.01	0.008	0.004
Eu*	1.14	1.31	1.24	1.11	1.07	0.94	1.05	1.04	1.26	1.21	1.04	1.04	1.16	1.46	0.87	0.92	1.29
La/Sm	1.93	1.81	0.04	4.40	2.92	2.93	2.82	0.95	4.13	2.82	1.59	3.90	2.85	3.45	1.06	0.97	3.97

b.d. = below detection limit; 1σ standard errors are found in Table A.2.

Eu*, Lu/Gd, La/Sm calculated using N-MORB normalized values (normalization from Gale et al., 2013).

Trace element concentrations in ppm.

Table 4

Palmietfontein clinopyroxene Pb isotope and garnet O isotope compositions.

	$^{206}Pb/^{204}Pb$	2σ	$^{207}Pb/^{204}Pb$	2σ	$^{208}Pb/^{204}Pb$	2σ	$\delta^{18}O$ (‰)
Palm-2	17.47	0.05	15.64	0.04	37.4	0.09	5.57
Palm-6	17.42	0.11	15.55	0.09	37.6	0.23	5.73
Palm-7	–	–	–	–	–	–	5.87
Palm-8	17.99	0.09	15.77	0.08	39.0	0.22	6.03
Palm-10	17.86	0.05	15.56	0.05	38.9	0.14	6.28
Palm-12	19.20	0.10	15.73	0.08	38.7	0.22	5.83
Palm-13	17.57	0.09	15.54	0.07	38.0	0.19	5.95
Palm-14	18.49	0.22	15.84	0.18	38.9	0.45	5.98
Palm-15	17.52	0.06	15.58	0.05	37.9	0.14	6.88
Palm-16	–	–	–	–	–	–	5.76
Palm-17	18.14	0.22	16.27	0.20	38.3	0.47	5.89
Palm-18	–	–	–	–	–	–	6.09
Palm-20	17.34	0.07	15.52	0.06	37.7	0.17	5.96
Palm-22	17.51	0.12	15.71	0.10	37.5	0.26	
Palm-23	–	–	–	–	–	–	5.91
Palm-24	17.71	0.18	15.58	0.15	37.1	0.36	5.60
Palm-28	17.28	0.12	15.51	0.10	37.2	0.25	5.47

Pb isotope compostions are present-day values, and represent averages of analyses from 5 individual clinopyroxene grains. The full Pb dataset can be found in Table A3.

4.4. Clinopyroxene in-situ Pb isotopic compositions

The in-situ Pb isotopic compositions of clear, inclusion- and crack-free clinopyroxene crystals from 13 Palmietfontein eclogite xenoliths were determined in grain mounts at the MITERAC ICP-MS Facility of the University of Notre Dame, U.S.A. Multiple Pb isotope ratios were measured using a NWR193 nm laser ablation system coupled to a Nu Plasma II MC-ICP-MS instrument. Clinopyroxene analyses involved spot analyses with a 150 μm laser beam at a repetition rate of 7–12 Hz and an energy density of 10–12 J/cm^3. Every six unknown analyses were bracketed by four measurements of the NIST SRM 614 glass (Baker et al., 2004) to monitor and correct for instrumental drift and mass bias, following the procedure outlined in Chen and Simonetti (2015). In total, the NIST SRM 614 glass was analysed 44 times and yielded average 2σ (RSD) external reproducibilities of ±0.85% for $^{208}Pb/^{204}Pb$, ±0.57% for $^{207}Pb/^{204}Pb$, ±0.49% for $^{206}Pb/^{204}Pb$, ±0.34% for $^{207}Pb/^{206}Pb$ and ±0.54% for $^{208}Pb/^{206}Pb$. Five clinopyroxene grains per eclogite were analysed, and averaged Pb isotopic compositions for Palmietfontein clinopyroxene mineral separates can be found in Table 4. The full data set plus NIST-SRM 614 results can be found in Table A3.

4.5. Garnet Fe^{3+}/ΣFe determination

Garnet mineral separates were analysed for Fe^{3+} contents by Mössbauer spectroscopy at the Goethe Universität, Frankfurt, Germany. Optically clean, inclusion and crack-free garnet from 16 Palmietfontein xenoliths were ground in acetone, mixed with sugar (Fe-free filler), packed into a hole drilled into a 1 mm thick Pb disc and covered with tape. In order to minimize saturation effects, sample thicknesses of <5 mg/cm^2 were obtained by both varying sample diameter and the amount of garnet sample used (~ 2–10 mg). Spectra were obtained at room temperature in constant acceleration mode and a velocity ramp of ±5 mm/s and a 50 mCi ^{57}Co in Rh source. Mirror-image spectra were collected over 512 channels until more than 2×10^6 counts per channel were reached. Spectra calibration was performed with respect to α-Fe metal. Fitting and folding of spectra followed Woodland and Koch (2003), including correction for differing recoil free fractions of Fe^{3+} and Fe^{2+} in garnet (Woodland and Ross, 1994). The corrected Fe^{3+}/ΣFe values are reported in Table 2 and have absolute uncertainties of ±0.01.

4.6. Garnet oxygen isotopic compositions

Garnet crystals from 16 Palmietfontein eclogite xenoliths were analysed for oxygen isotope composition by laser fluorination and dual-inlet mass spectrometry at the University of Cape Town, South Africa, following Harris and Vogeli (2010). Clean garnet mineral separates

(between 1 and 4 grains, weighing 1–3 mg) were used for the analyses. Oxygen isotope ratios were measured offline on O$_2$ gas using a Finnigan Delta XP MS in dual-inlet mode, where yields were determined by comparing the sample weight to the measured gas pressure at the MS inlet at constant volume and were close to 100% for all analyses. The data reported here were normalized to the internal garnet standard MON-GT ($\delta^{18}O = 5.38‰$; Harris and Vogeli, 2010), which was run twice for every 10 unknown Palmietfontein garnets and has a long-term reproducibility of 0.077‰ (1σ,n = 283). Garnet $\delta^{18}O$ values are presented in Table 4.

5. Results

5.1. Mantle zircon U/Pb age constraints

An approximately 1 cm large, light brown mantle zircon crystal (ST17-50-1) was recovered from heavy mineral concentrate of the Palmietfontein kimberlite pipe at the University of Johannesburg in 2017. The mantle zircon was embedded into epoxy resin and polished to expose a flat crystal surface suitable for laser ablation analysis. A total of 20 individual spot measurements were performed on zircon ST17-50-1 along a core-rim traverse by LA-MC-ICP-MS analysis. The U and Th contents range between 6 and 10 ppm (outlier at 17 ppm) and 0.3–0.7 ppm (outlier at 1 ppm), respectively, and these low U and Th concentrations are typical for mantle-derived zircon (Belousova et al., 1998; Sun et al., 2018).

The measured isotope ratios along the zircon core-rim traverse are relatively uniform, yielding a weighted average $^{206}Pb/^{238}U$ age of 75.2 ± 0.5 Ma (2-sigma) for the 20 spot analyses, which is in excellent agreement with the lower intercept age of 74.7 ± 0.5 Ma (2-sigma) obtained in Tera-Wasserburg Concordia space (Fig. 3). This lower intercept age with Concordia is defined by a regression line that was forced through the complete U/Pb dataset and an upper intercept $^{207}Pb/^{206}Pb$ value of 0.8406 for a minute common Pb component, as guided by the Stacey and Kramers (1975) terrestrial Pb isotope evolution model. In general, it has been demonstrated that mantle xenocryst zircon U/Pb ages and ages determined for the host kimberlite by the groundmass perovskite U/Pb method are typically overlapping within their analytical uncertainties, with only small or no age discrepancies between these contrasting materials (Griffin et al., 2014; Woodhead et al., 2017; Sun et al., 2018; Tappe et al., 2018a). Hence, it is reasonable to infer that the mantle zircon U/Pb age of ca. 75 Ma reflects the timing of Group-1 kimberlite magmatism in the Palmietfontein area on the northern Kaapvaal craton in the vicinity of the ca. 1395 Ma Pilanesberg alkaline complex and the ca. 2056 Ma Bushveld Complex (Fig. 1). The newly obtained high-precision U/Pb zircon age is slightly younger than
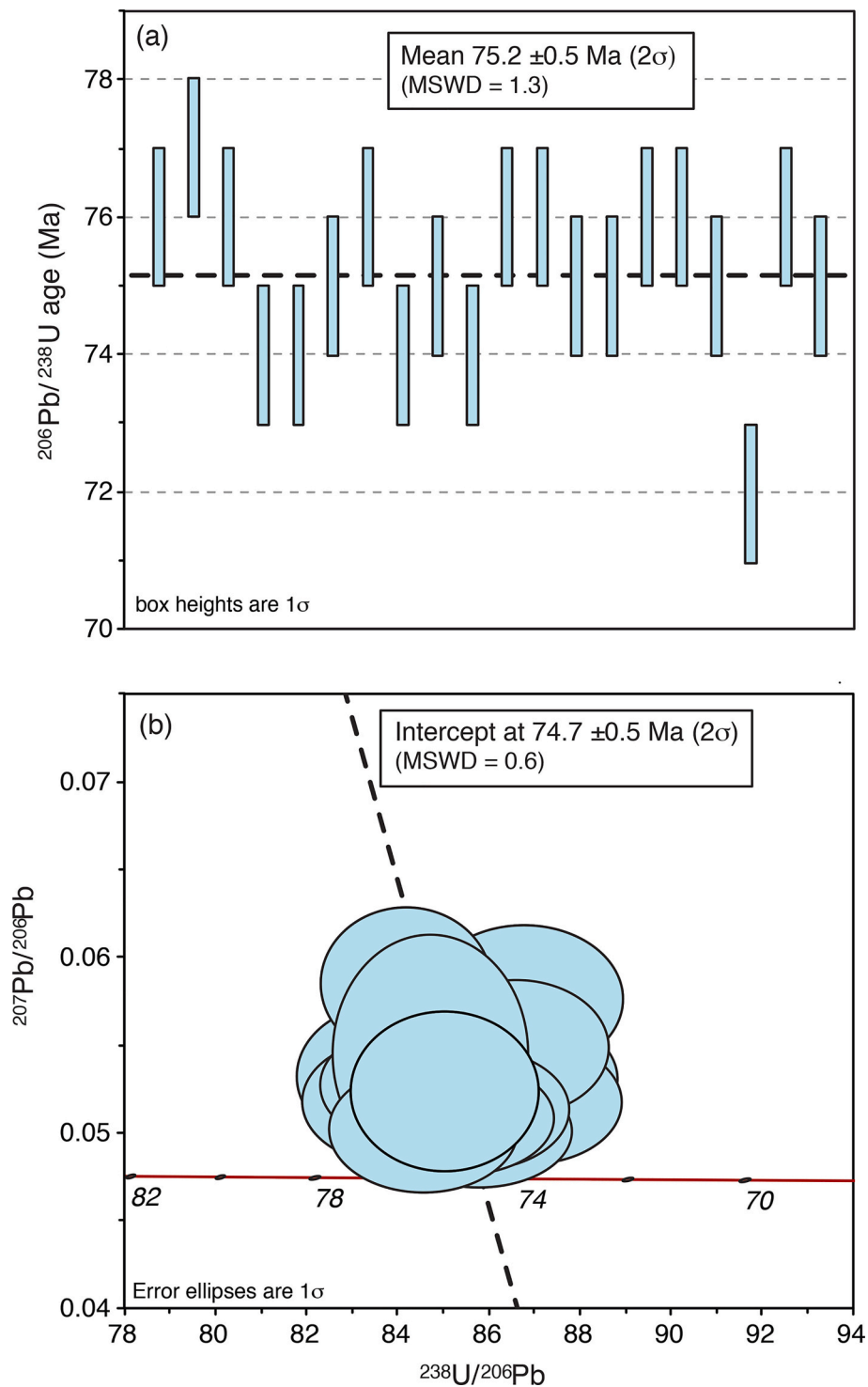
Fig. 3. (a) Weighted average $^{206}Pb/^{238}U$ age of 75.2 ± 0.5 Ma (2 σ) for 20 spot measurements of mantle zircon ST17-50-1 recovered from the Palmietfontein kimberlite. **(b)** Tera-Wasserburg concordia diagram showing the lower intercept age of 74.7 ± 0.5 Ma (2 σ) for the Palmietfontein mantle zircon. Details of the age determinations can be found in **Section 5.1**. Ages are calculated using Isoplot (Ludwig, 2000).

the age previously reported for the Palmietfontein kimberlite in geochronology databases (ca. 92 Ma; Skinner, 1989; Jelsma et al., 2009; Tappe et al., 2018a), but in the absence of scrutinized data and results for standards it is impossible to evaluate the quality and significance of this date. Regardless, the Late Cretaceous pulse of bona fide kimberlite magmatism (>20 kimberlite pipes are known from the Palmietfontein area) may thus represent the youngest igneous activity that affected the Kaapvaal craton, with time equivalent kimberlite magmatism known

from the Proterozoic Rehoboth Terrane in Namibia (e.g., the ca. 73 Ma Gibeon kimberlite cluster; Tappe et al., 2018a).

5.2. Mineral compositions

Garnet from the Palmietfontein eclogite xenoliths have low Cr_2O_3 contents of 0.03–0.22 wt%, with 7.9–18 wt% MgO, 12.2–21.6 wt% FeO, and 3.9–10.4 wt% CaO (Table 2). The garnets have Mg-numbers (Mg#
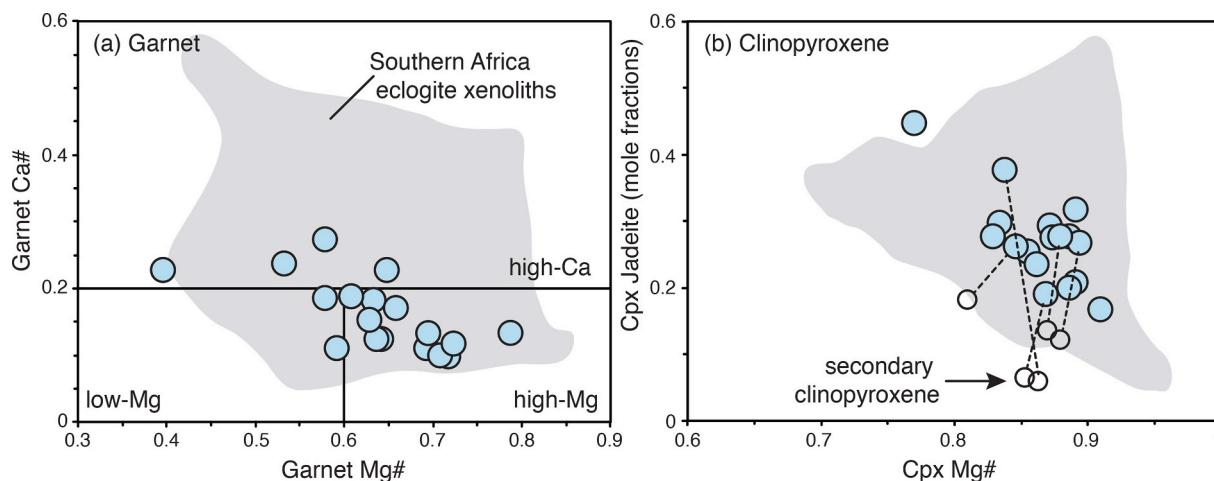
Fig. 4. Composition of **(a)** garnet and **(b)** clinopyroxene from the Palmietfontein eclogite xenoliths. Garnet Ca#, Mg# and clinopyroxene Mg# and jadeite % (Jd) calculated from cation abundances (see Table 2). "High-Ca", "high-Mg" and "low-Mg" garnet classification fields from Aulbach and Jacob (2016). The compositions of garnet and clinopyroxene from other southern Africa eclogite suites are shown for comparison (grey field; MacGregor and Manton, 1986; Greau et al., 2011; Pyle and Haggerty, 1998; Jacob et al., 2009; Aulbach and Viljoen, 2015; Aulbach et al., 2016, 2017b; Burness et al., 2020; Smart et al., 2021). The compositions of secondary clinopyroxene, found as rims on primary clinopyroxene (see **Fig. A.1**) in five Palmietfontein eclogites are indicated in **(b)**.

= Mg/[Mg + Fe]) of 0.40–0.72, and Ca-numbers (Ca# = Ca/[Mg + Fe + Ca + Mn]) of 0.10–0.27, (Fig. 4a). Using garnet geochemistry and the classification criteria of Aulbach and Jacob (2016), 11 Palmietfontein eclogites contain "high-Mg" garnet (Mg # > 0.6), 4 eclogites contain "high-Ca" garnet (Ca # > 0.2), and 2 eclogites contain "low-Mg" garnet (Mg # < 0.6). Garnet Fe^{3+} contents, expressed as $Fe^{3+}/\Sigma Fe$ (Table 2), range between 0.009 and 0.036 ± 0.01. Garnets from the Palmietfontein eclogites have Ni contents of 4–23 ppm, Y of 7–57 ppm and Pb contents of below detection to 0.1 ppm (Table 2). On chondrite-normalized REE

diagrams (Figure A2a), the Palmietfontein garnets display both positive and negative Eu anomalies ranging from 0.82 to 1.67 (Eu* = 2 × Eu/ [Sm + Gd]) and variably enriched and fractionated (Lu = 5.6–60; Lu/ Gd = 0.67–4.1) HREE contents. Garnet from Palm-23 is comparatively enriched in incompatible elements (Fig. A.2a) with marked enrichments in La (0.75 vs. <0.1 ppm) and Ce (0.91 vs. < 0.33 ppm). Garnet from 16 of the Palmietfontein eclogites have $\delta^{18}O$ values between 5.5 and 6.3 ± 0.1‰ (Table 4), falling slightly above the accepted mantle average of 5.5 ± 0.4‰ (Mattey et al., 1994).
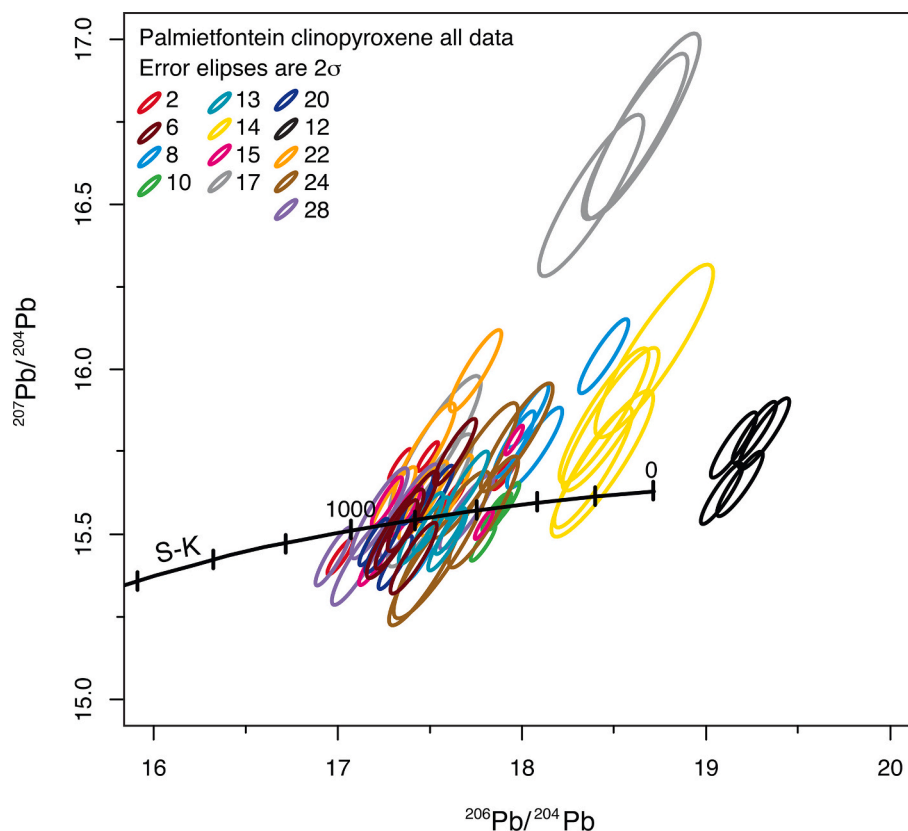

Fig. 5. Present-day Pb isotope compositions of clinopyroxene from the Palmietfontein eclogite xenoliths showing all measured $^{206}Pb/^{204}Pb$ and $^{207}Pb/^{204}Pb$ data. The two-stage model Pb curve "S-K" of Stacey and Kramers (1975) is shown with model ages in Ma.

Clinopyroxenes from the Palmietfontein eclogites are mostly "eclogitic", with molar Na/(Na + Ca) ratios >0.2 (excluding Palm-28 = 0.19), jadeite contents from 20 to 44 mol% (excluding Palm-28 = 0.17 and Palm-10 = 0.19) and Mg numbers from 0.77 to 0.91. Clinopyroxene has a MgO content of 8.4–14.6 wt%, CaO of 13.3–19.9 wt%, Na_2O of 2.62–6.52 wt%, and Al_2O_3 of 4.63–11.5 wt% (Table 2; Fig. 4b). Some clinopyroxenes are mantled with compositionally distinct secondary rims (see Section 2.1; Figure A1) that have lower jadeite (7–18 mol%) and generally higher MgO (14.5–15.3 wt%) and CaO (18.4–21.2 wt%) contents (Fig. 4b; Table A1). Trace element analyses were only possible for the "primary" clinopyroxene, which contains contain 80–424 ppm Ni, 72–509 ppm Sr, 0.3–3.3 ppm Pb, below detection to 0.14 ppm U and below detection to 0.81 ppm Th (Table 3). Palmietfontein clinopyroxenes have negatively-sloping REE patterns (FIgure A2b) with both variable LREE contents (La_N = 3.8–60) and patterns (La_N/Sm_N = 0.95–4.4). Clinopyroxene from Palm-7 displays a markedly depleted LREE pattern (La_N = 0.75, La_N/Sm_N = 0.4).

Amphibole found in eclogites Palm-10, −12 and − 18 is calcic to sodic-calcic with 8.7–10.7 wt% CaO and 3.8–4.6 wt% Na_2O, and classifies as pargasite and katophorite (Locock, 2014; Leake et al., 1997; Table A1). The amphibole has relatively constant MgO (17.4–17.9 wt%) and FeO (4.9–5.9 wt%), with low K_2O contents of 0.76–0.82 wt%. Amphibole in all three samples has low concentrations of trace elements, excluding elevated Ba (16–66 ppm) and Sr (23–26 ppm) contents (Figure A2c). Amphibole from Palm-10 displays distinctive negative troughs at Zr-Hf and positive spikes at Nb, in contrast to amphibole from Palm-12 and -18 that do not show Zr-Hf troughs, but instead display relative depletions in Nb-Ta. These different HFSE fractionations among amphiboles may be related to the presence of rutile in Palm-12 and -18, because rutile has significantly higher partition coefficients for Nb and Ta compared to Zr and Hf, and it largely controls the Nb-Ta budget of eclogites (Zack et al., 2002; Foley et al., 2000). Although zircon was not observed in the Palmietfontein eclogite xenoliths (only as megacrysts in the host kimberlite; Section 5.1), zircon has been reported from mantle eclogite xenoliths of the Slave craton in Canada (Schmidberger et al., 2005). The possible presence of zircon would control the Zr-Hf budget of our eclogite samples, and may explain the Zr-Hf depletions in 'coexisting' silicate phases (Zack et al., 2002), as observed for amphibole in sample Palm-10. Finally, any titanate mineral partitioning effect on coexisting amphibole HFSE budgets may be compounded by crystal

chemical effects of Ti and Nb-Ta in amphibole (Tiepolo et al., 2000; Foley et al., 2002). This could mean that the lower TiO_2 content of 0.53 wt% in Palm-10 amphibole (compared to ~1 wt% in Palm-12 and -18 amphibole) may cause increasing Nb and Ta partitioning into its crystal lattice.

5.3. Clinopyroxene Pb isotopic compositions

The $^{206}Pb/^{204}Pb$, $^{207}Pb/^{204}Pb$ and $^{208}Pb/^{204}Pb$ ratios were determined for clinopyroxene from 13 Palmietfontein eclogite xenoliths. The measured, present-day isotopic compositions are reported in Table 4 and represent an average of 5 clinopyroxene analyses per sample (the full dataset can be found in Table A3). The Palmietfontein clinopyroxene crystals have $^{206}Pb/^{204}Pb$ ratios of 17.28–19.20, $^{207}Pb/^{204}Pb$ of 15.51–16.27 and $^{208}Pb/^{204}Pb$ of 37.13–38.98. The $^{207}Pb/^{204}Pb$ ratios of >15.8 (e.g. Palm-8, −14, −17, −22) are associated with large uncertainties (2σ >0.1). Correction of the measured Pb isotope ratios for radiogenic in-growth since kimberlite magma eruption at ca. 75 Ma, using $^{238}U/^{204}Pb$ and $^{235}U/^{204}Pb$ calculated from measured clinopyroxene U and Pb contents (Table 3; Section 4.1), results in minute changes of ~0.02 to 0.06 for $^{206}Pb/^{204}Pb$ and 0.001 to 0.004 for $^{207}Pb/^{204}Pb$. These very small changes are generally encompassed within the symbol error bars in Fig. 5. In Fig. 5, the Palmietfontein clinopyroxene $^{206}Pb/^{204}Pb$ and $^{207}Pb/^{204}Pb$ compositions intercept the two-stage terrestrial Pb isotope evolution curve of Stacey and Kramers (1975) at model ages from 200 to 1000 Ma, and only clinopyroxene from the Palm-12 eclogite xenolith falls to the right of the Stacey-Kramers curve. Regression of the Pb isotope data using IsoplotR (Vermeesch, 2018) produces variable results based on the selected model parameters. The maximum likelihood regression (Model 1, incorporating 2-sigma uncertainties at a 90% confidence level) of all measured Pb isotope data gives an "isochron age" of 989 ± 243 Ma (Figure A3a; this "age" increases to 1145 ± 217 Ma if $^{207}Pb/^{204}Pb$ values of >15.8 are removed). Ordinary least-squares regression (Model 2, ignoring uncertainties) of all measured Pb isotope data yields an "isochron" age of 3280 ± 282 Ma (Figure A3b), but decreases to 2047 ± 401 Ma (Figure A3c) when $^{207}Pb/^{204}Pb$ values of >15.8 are excluded. The significance of these "ages" will be interpreted in Section 6.3 in light of prevalent Archean ages determined for Kaapvaal eclogite xenoliths, as well as the punctuated metasomatic history of the Kaapvaal lithospheric mantle.

5.4. P-T-fO₂ equilibration conditions for the Palmietfontein eclogite xenoliths

The pressure and temperature conditions of last equilibration for the Palmietfontein eclogites were calculated iteratively using the thermometer of Krogh-Ravna (2000), T_{KR00}, in combination with either the barometer of Beyer et al. (2015), P_{B15}, or the 40 mW/m² conductive geotherm from Hasterok and Chapman (2011), P_{HC40}. A 40 mW/m² paleogeotherm is considered representative for the southern African mantle lithosphere as sampled by ca. 90 Ma kimberlites in South Africa and Botswana (e.g., Kimberley, Koffiefontein, Orapa and Jagersfontein; Grütter, 2009; Stiefenhofer et al., 1997; Katayama et al., 2009), and these slightly warmer geothermal conditions appear to have prevailed in this cratonic region for the past billion years (Tappe et al., 2021). The $T_{KR00} − P_{B15}$ combination yields conditions of 628–944 °C and 0.5–2.7 GPa, whereas the $T_{KR00} − P_{HC40}$ combination yields higher temperatures and pressures of 740–1064 °C and 2.7–4.5 GPa (Table 5; Fig. 6a). Using the Krogh (1988) calibration of the Fe-Mg exchange thermometer results in a higher temperature range from 771 to 1096 °C, with insignificant pressure differences. The amphibole-bearing eclogites Palm-10, −12 and − 18 have equilibration pressures of 3.0 to 3.3 GPa, which is consistent with the stability limit of amphibole (Poli, 1993; Green et al., 2014). Application of the garnet – amphibole thermometer of Ravna (2000) to Palm-10, −12 and − 18 results in temperatures of 604, 696

Table 5
Calculated T-P-fO_2 for the Palmietfontein eclogite xenoliths.

	T_{KR00} - P_{B15}		T_{KR00} - P_{HC40}		log fO_2
	°C	kbar	°C	kbar	ΔFMQ
Palm-2	712	14	816	31	−3.2
Palm-6	778	18	911	36	−4.0
Palm-7	797	23	858	33	−1.6
Palm-8	764	18	886	35	−3.7
Palm-10	695	16	786	30	−3.5
Palm-12	750	20	842	33	
Palm-13	750	17	873	34	−4.1
Palm-14	944	27	1064	45	−3.4
Palm-15	766	20	852	33	−3.6
Palm-16	628	5	778	29	−2.8
Palm-17	668	14	749	27	−3.9
Palm-18	767	21	852	33	−4.5
Palm-20	766	20	862	34	−4.2
Palm-22	782	19	878	35	−1.6
Palm-23	781	20	873	34	−2.8
Palm-24	821	21	919	37	−2.9
Palm-28	684	18	740	27	−3.5

Temperatures and pressures calculated using combination of the Beyer et al. (2015) barometer (PB15), the Krogh-Ravna (2000) thermometer (TKR00), and the 40 mW/m2 conductive geotherm (PHC40) of Hasterok and Chapman (2011); see Section 5.4. Oxygen fugacities calculated after Stagno et al. (2015) using the TKR00 and PHC40 results and expressed relative to the fayalite-magnetite-quartz buffer.
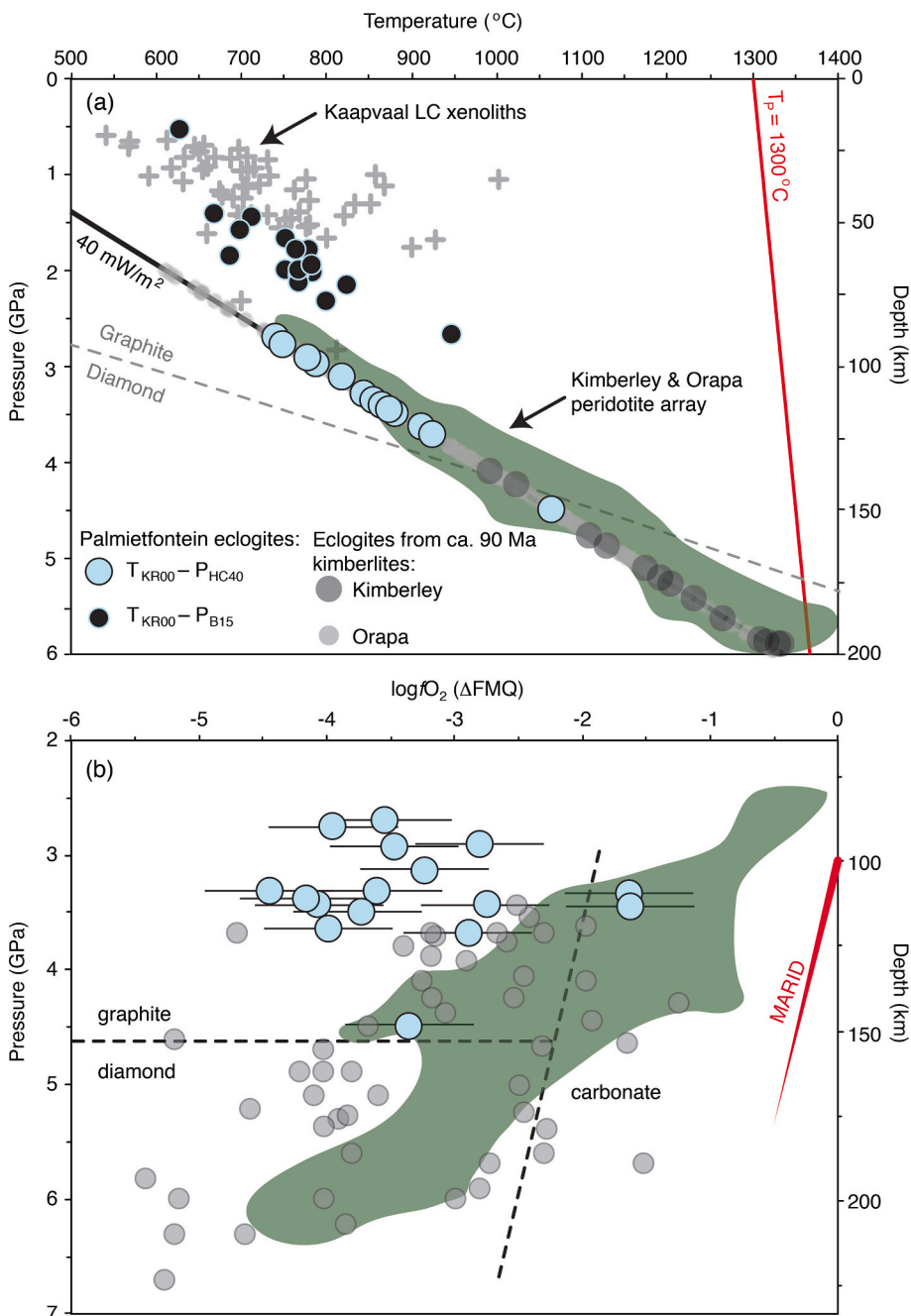
Fig. 6. Calculated pressure, temperature and oxygen fugacity conditions for the Palmietfontein eclogites. **(a)** Pressure - temperature conditions were calculated using the geothermometer of Krogh Ravna (2000; T_{KR00}) and either the 40 mW/m² conductive geotherm of Hasterok and Chapman (2011; P_{HC40}) or the barometer of Beyer et al. (2015; P_{B15}). The 40 mW/m² geotherm corresponds approximately to the peridotite xenolith-defined geotherm (green field) for other 90 Ma Group-1 kimberlites nearest to the Palmietfontein kimberlite, such as Orapa (Stiefenhofer et al., 1997); Goedgevonden (Kobussen et al., 2012) and the Kimberly cluster (Katayama et al., 2009). Shown for comparison are eclogite T_{KR00} – P_{HC40} values recalculated for eclogites from proximal 90 Ma southern Africa kimberlites (Orapa, Aulbach et al., 2017b; Kimberley, Jacob et al., 2009) and Kaapvaal lower crustal xenoliths (Huang et al., 1995; Van Calsteren et al., 1986; Pearson et al., 1995a, 1995b; Sommer et al., 2013; Pretorius and Barton Jr., 2003). Graphite-diamond transition from Day (2012). Mantle adiabat ($T_P = 1300$ °C) from Kimura and Kawabata (2014). **(b)** Pressure and oxygen fugacity conditions calculated using T_{KR00} and P_{HC40} with the oxybarometer of Stagno et al. (2015). Shown for comparison are P-fO_2 conditions for Kaapvaal eclogites where measured garnet Fe^{3+} exists: Lace (Aulbach et al., 2016); Roberts Victor and Jagersfontein (Burness et al., 2020). Kaapvaal peridotite P-fO_2 data from Woodland and Koch (2003), Creighton et al. (2009), Lazarov et al. (2009) and Hanger et al. (2015). Estimated MARID field from Creighton et al. (2009). Graphite-diamond-carbonate fields redrawn from Stagno et al. (2015). (For interpretation of the references to colour in this figure legend, the reader is referred to the web version of this article.)

and 336 °C, respectively, significantly lower than temperatures of 786, 842 and 852 °C calculated using T_{KR00}. These lower temperatures are most likely result from the generally lower Al and Ti but higher Na and Ca compositions of the Palmietfontein eclogite amphiboles compared to those used in the Ravna (2000) thermometer calibration. The Palmietfontein eclogite xenoliths pressures are relatively low compared to the range of 2–8 GPa calculated for diverse Kaapvaal cratonic mantle eclogite xenolith suites (e.g., Aulbach and Viljoen, 2015; Aulbach et al., 2017b; Schmickler et al., 2004). Several Palmietfontein eclogite samples have P_{B15} conditions that correspond to residence at crustal or shallow lithospheric mantle depths, where eclogite metamorphic assemblages are not stable (e.g., Palm-16). For example, calculated P_{B15} of 0.5 GPa for Palm-16 corresponds to eclogite residence within the cratonic crust at ~17 km depths, and both Palm-2 and Palm-17 have a calculated pressure of 1.4 GPa suggesting eclogite residence at ~46 km at the Kaapvaal Moho (34–47 km; James et al., 2003). Importantly, these three

eclogite nodules record significantly higher geotherm-derived pressures (P_{HC40}) between 2.8 and 3.1 GPa, which correspond to eclogite residence at lithospheric mantle depths of ~90 to 100 km. Uncertainty with the Beyer et al. (2015) barometer for cratonic eclogites is related largely to Ca-Tschermak and Si contents of clinopyroxene, and P_{B15} is not recommended for eclogites that contain clinopyroxene with >1.985 atoms Si per formula unit (Beyer et al., 2015). Clinopyroxene in our samples has molar Si <1.985 (except for Palm-20 with 1.986) and is characterized by cation totals of 4.01 ± 0.01 (1σ). Given that the Beyer et al. (2015) barometer is prescribed for minimum conditions of 2 GPa and 700 °C, the low apparent equilibration pressures obtained for the Palmietfontein eclogites appear to test the limits of the original experimental calibration and may call their validity into question. Therefore, only T_{KR00}-P_{HC40} equilibration conditions will be considered further.

The oxygen fugacity of 16 Palmietfontein eclogite xenoliths was calculated using measured garnet $Fe^{3+}/\Sigma Fe$ contents and the

Table 6
Calculated bulk Palmietfontein eclogite major and trace element compositions.

	Palm-2	Palm-6	Palm-7	Palm-8	Palm-10	Palm-12	Palm-13	Palm-14	Palm-15	Palm-16	Palm-17	Palm-18	Palm-20	Palm-22	Palm-23	Palm-24	Palm-28
Trace element class:	Gabbroic-Enriched	Gabbroic-Enriched	Basaltic	Basaltic-Enriched	Basaltic-Enriched	Basaltic-Enriched	Gabbroic-Enriched	Basaltic	Gabbroic-Enriched	Gabbroic-Enriched	Basaltic	Gabbroic-Enriched	Gabbroic-Enriched	Gabbroic-Enriched	Basaltic	Basaltic	Gabbroic-Enriched
SiO_2	47.4	47.2	46.2	47.7	47.6	48.0	47.0	46.7	47.0	46.7	47.1	47.9	47.3	46.8	46.7	46.5	47.3
TiO_2	0.1	0.1	0.1	0.1	0.2	0.2	0.1	0.2	0.1	0.2	0.1	0.2	0.1	0.2	0.1	0.2	0.1
Al_2O_3	16.3	16.1	16.9	16.2	14.0	14.5	15.5	17.6	15.4	16.0	16.9	14.6	15.6	16.5	15.7	16.2	14.8
Cr_2O_3	0.1	0.1	0.0	0.1	0.2	0.2	0.0	0.1	0.2	0.1	0.1	0.2	0.1	0.1	0.1	0.1	0.1
FeO	10.0	8.6	13.9	9.0	9.4	8.0	10.1	9.5	10.0	8.9	9.1	8.1	11.7	8.4	10.7	11.1	7.9
MnO	0.2	0.2	0.3	0.2	0.2	0.2	0.2	0.2	0.2	0.2	0.2	0.2	0.2	0.2	0.3	0.3	0.2
MgO	12.8	14.7	8.1	15.2	15.0	16.2	14.1	10.5	13.7	14.6	12.7	16.1	13.4	12.7	12.3	10.9	16.4
CaO	11.6	10.4	10.5	9.9	11.5	10.8	10.5	12.4	11.3	11.4	11.1	10.7	9.9	12.6	11.6	12.4	11.3
Na_2O	2.0	1.9	2.9	1.9	1.7	1.7	1.7	2.6	1.6	1.9	2.1	1.6	1.9	1.9	1.8	2.0	1.2
K_2O	–	–	–	–	0.12	0.04	–	–	–	–	–	0.04	–	–	–	–	–
Total	99.5	99.4	99.0	100.2	99.9	99.7	99.3	99.8	99.5	98.9	99.5	100.0	100.5	99.3	99.3	99.6	99.3
Mg#	0.7	0.8	0.6	0.8	0.6	0.8	0.7	0.7	0.7	0.8	0.7	0.8	0.7	0.8	0.7	0.7	0.8
V	219	211	262	223	218	222	245	354	444	216	181	222	284	193	508	556	187
Ni	122	124	81	153	123	75	91	46	134	129	204	150	137	130	40	38	180
Sc	50	37	36	33	38	36	37	47	40	48	33	36	51	41	64	53	32
Rb	0.05	0.03	0.10	0.03	0.05	0.05	0.04	0.01	0.05	0.15	0.03	0.02	0.03	0.01	0.27	0.06	0.02
Ba	0.04	0.02	0.05	0.04	2.50	3.47	0.04	0.05	0.20	0.11	0.07	3.08	0.03	0.06	0.39	0.09	0.15
Th	0.05	0.17	0.00	0.24	0.15	0.37	0.12	0.02	0.05	0.07	0.05	0.14	0.09	0.03	0.09	0.04	0.35
U	0.07	0.04	0.00	0.07	0.05	0.04	0.05	0.06	0.04	0.08	0.03	0.09	0.04	0.05	0.11	0.07	0.05
Nb	0.28	0.02	0.01	0.01	0.10	0.01	0.01	0.20	0.03	0.25	0.03	0.05	0.01	0.01	0.22	0.12	0.04
Ta	0.02	0.003	0.001	bd	0.004	0.007	0.001	0.006	0.002	0.011	0.002	0.002	0.010	0.001	0.011	0.003	0.002
La	1.5	2.5	0.0	3.8	3.1	7.7	3.6	0.4	2.2	1.5	0.7	3.3	3.8	1.4	2.3	1.4	6.4
Ce	4.7	8.8	0.0	9.2	6.7	16.7	9.1	1.5	6.1	4.0	1.6	8.4	10.1	3.9	8.8	5.3	15.7
Pr	0.7	1.4	0.0	1.0	0.8	1.9	1.2	0.3	0.7	0.6	0.2	0.9	1.3	0.5	1.6	1.0	1.8
Pb	0.6	0.7	0.1	1.0	1.4	0.8	0.9	0.4	0.9	0.8	0.3	0.9	0.9	0.6	0.9	0.5	0.6
Sr	112	185	33	229	172	222	183	131	158	102	56	199	182	126	153	136	214
Nd	3.0	6.1	0.6	3.3	3.5	7.7	5.1	2.1	2.5	2.2	0.9	3.4	5.3	2.3	8.2	5.5	6.5
Sm	0.7	1.2	1.5	0.7	0.8	2.0	1.0	0.9	0.5	0.5	0.5	0.8	1.1	0.5	2.2	1.9	1.2
Zr	3.1	6.4	7.7	11.9	2.8	38.3	6.2	8.1	9.0	2.6	6.9	5.5	6.5	4.0	14.6	8.8	17.4
Hf	0.1	0.2	0.8	0.4	0.1	1.1	0.2	0.3	0.3	0.1	0.2	0.1	0.2	0.1	0.4	0.2	0.5
Eu	0.3	0.5	0.8	0.3	0.3	0.6	0.3	0.4	0.2	0.2	0.2	0.3	0.4	0.3	0.8	0.7	0.5
Ti	962	920	708	963	495	911	868	1305	838	941	758	1105	959	1051	1016	1089	843
Gd	0.8	1.1	3.1	1.3	1.0	2.4	0.9	1.6	0.7	0.6	0.8	1.0	1.3	0.7	2.9	2.5	1.4
Tb	0.1	0.2	0.6	0.3	0.2	0.4	0.2	0.4	0.1	0.1	0.1	0.1	0.3	0.1	0.6	0.5	0.2
Dy	1.1	1.1	4.0	2.2	1.5	3.6	1.4	3.3	1.2	1.1	0.8	1.0	2.2	0.9	4.8	3.7	1.5
Y	7.2	6.3	21.1	12.9	8.5	21.1	9.1	22.5	8.5	6.7	4.1	5.5	15.1	5.1	32.3	23.6	7.7
Ho	0.3	0.2	0.8	0.5	0.3	0.8	0.3	0.8	0.3	0.2	0.2	0.2	0.6	0.2	1.2	0.9	0.3
Er	0.8	0.7	2.2	1.5	0.9	2.5	1.1	2.8	1.1	0.8	0.4	0.6	2.0	0.6	4.0	2.8	0.8
Tm	0.1	0.1	0.3	0.2	0.1	0.4	0.2	0.5	0.2	0.1	0.1	0.1	0.3	0.1	0.7	0.5	0.1
Yb	0.9	0.7	1.9	1.6	0.9	2.6	1.3	3.4	1.4	0.9	0.5	0.7	2.4	0.6	5.1	3.4	0.8
Lu	0.1	0.1	0.2	0.2	0.1	0.4	0.2	0.5	0.2	0.1	0.1	0.1	0.4	0.1	0.8	0.5	0.1
Eu*	1.18	1.42	1.11	1.00	1.05	0.92	1.08	0.99	1.29	1.37	1.09	1.11	1.19	1.64	0.98	1.01	1.32
Ce/Sm	1.62	1.53	0.00	4.27	2.64	2.84	2.73	0.35	3.52	2.27	1.01	3.03	2.55	2.11	0.77	0.54	3.85
Yb/Gd	1.55	0.89	0.83	1.60	1.22	1.45	2.00	2.97	2.72	2.00	0.83	0.88	2.58	1.19	2.45	1.85	0.78

Eu* as calculated in Table 2; Ce/Sm and Yb/Gd values are N-MORB normalized (values from Gale et al., 2013). Trace element classification discussed in Section 5.5 and Fig. 8.

Major elements contents in wt%; trace element contents in ppm.
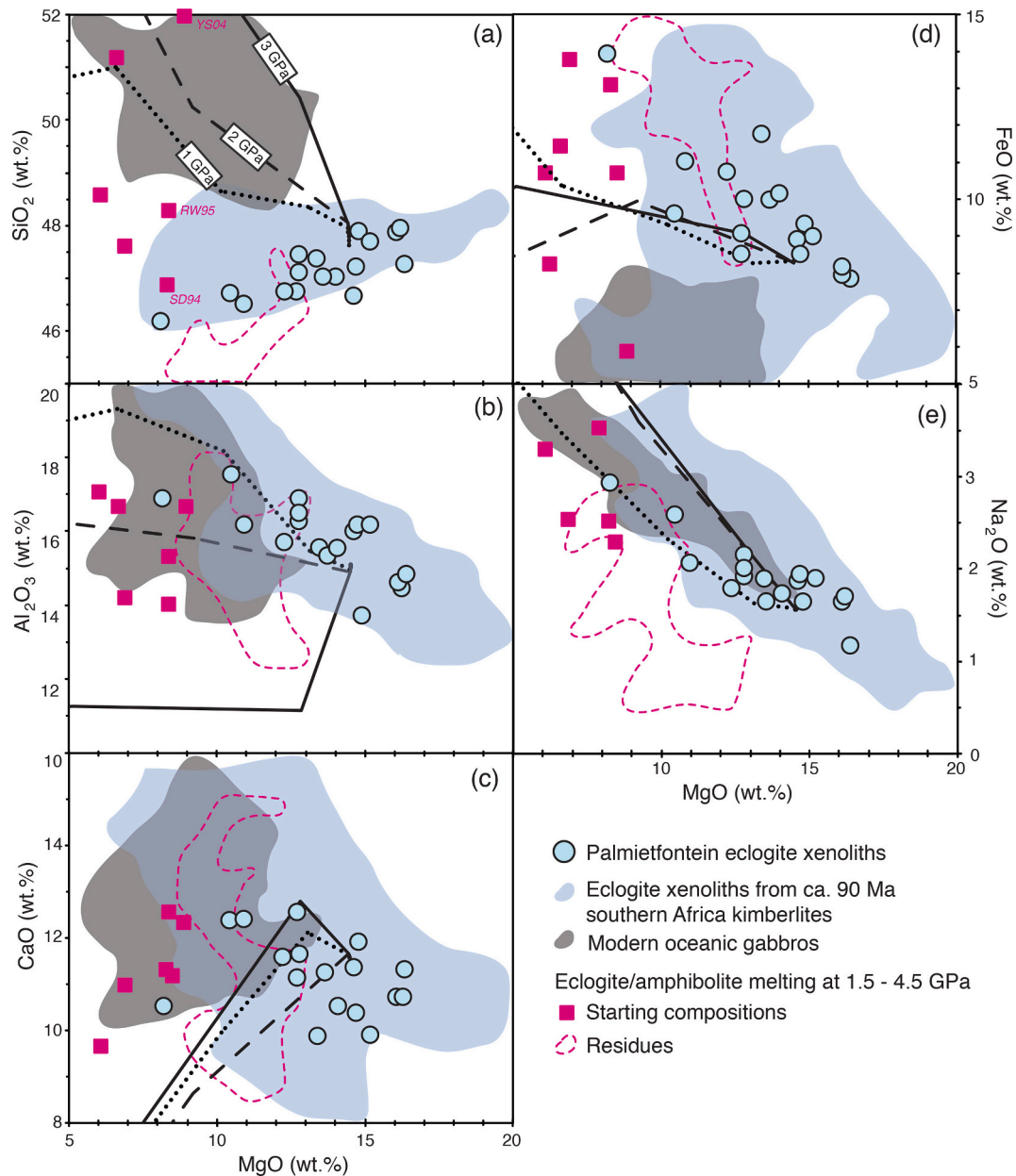
Fig. 7. Calculated bulk rock major element compositions of the Palmietfontein eclogite xenoliths (see Section 5.5). Lines indicate pMelts fractional crystallization trends for picrite (Falloon and Green, 1998) between 1 and 3 Gpa (Ghiroso et al., 2002). Square symbols and dashed fields indicate the effect of partial melting on amphibolite-to-eclogite-facies basalts (Sen and Dunn, 1994; Rapp and Watson, 1999) and gabbros (Yaxley and Sobolev, 2007). Shown for comparison are eclogite xenoliths from 90 Ma "Group-1" kimberlites of the Kaapvaal craton (Aulbach and Viljoen, 2015; Aulbach et al., 2016, 2017b; Gréau et al., 2011; Jacob et al., 2009; Pyle and Haggerty 1998; Smart et al., 2021; Burness et al., 2020) and the composition of modern oceanic gabbros (Bach et al., 2001). (For interpretation of the references to colour in this figure legend, the reader is referred to the web version of this article.)

oxybarometer of Stagno et al. (2015), which is calibrated for silica-saturated (i.e. quartz/coesite-bearing) eclogites. For the T_{KR00} and P_{HC40} conditions outlined above and garnet $Fe^{3+}/\Sigma Fe$ contents of 0.009–0.036, the Palmietfontein eclogites yield calculated $\Delta log fO_2$ values that range from FMQ-4.5 to FMQ-1.6 (FMQ = fayalite-magnetite-quartz reference buffer, Fig. 6b). The oxybarometer of Stagno et al. (2015) has an associated uncertainty of 0.5 log units, and absolute uncertainties of 0.01 for the measured $Fe^{3+}/\Sigma Fe$ contents translate into an additional uncertainty of 0.09 log units. Also, the Palmietfontein eclogites do not contain a 'free' silica phase and applying this oxybarometer to silica-undersaturated eclogites will introduce additional uncertainty for the calculated fO_2 values (e.g. Smart et al., 2021; Aulbach et al., 2017c). Since the Palmietfontein eclogites are biminerallic (±amphibole), silica activities cannot be readily calculated to determine

quantitative uncertainties for resulting fO_2. For a suite of variably corundum-bearing, silica-undersaturated eclogites from the western Kaapvaal craton, Smart et al. (2021) found that eclogite fO_2 values correlate with clinopyroxene Ca-Tschermak contents, and the corundum-bearing high-Al eclogites had both the highest Ca-Tschermak contents and highest (i.e., most oxidized) calculated fO_2 values with associated elevated uncertainties of 1.5 log units. Corundum is absent from the Palmietfontein eclogites, but the Ca-Tschermak's component (and total Al_2O_3 contents) also correlates weakly with calculated fO_2 values ($r^2 = 0.19$; Figure A4). The potentially more silica-undersaturated Palmietfontein eclogites (i.e., those with higher Ca-Tschermak's component) also have the most oxidized redox composition, suggesting that these "high" $\Delta log fO_2$ values may also have more significant uncertainties, which unfortunately remain unquantifiable. In
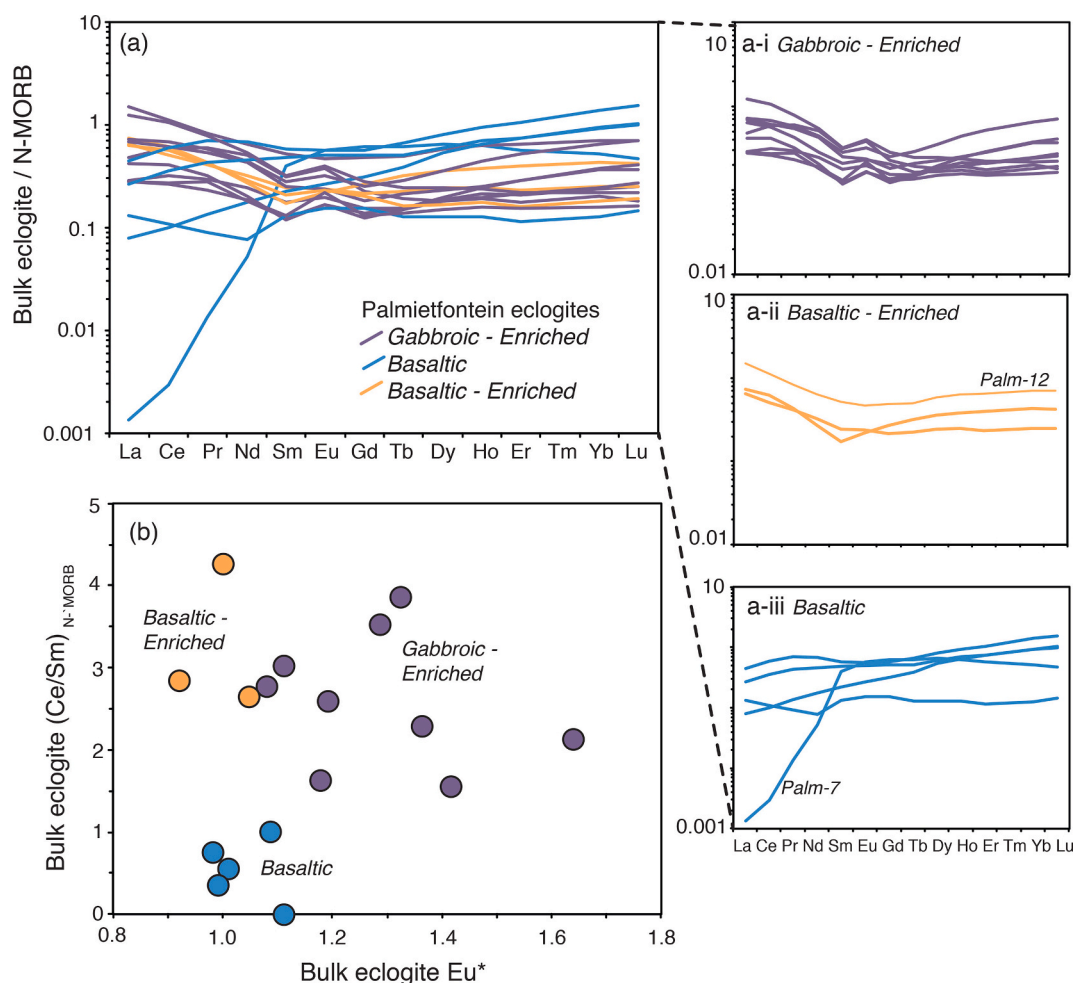
Fig. 8. (a) Calculated bulk REE compositions of the Palmietfontein eclogites, normalized to N-MORB. The eclogites have been divided into three groups (see **Section 5.5** and Table 6) based on the presence of a Eu anomaly (Eu*) and degree of LREE enrichment, as demonstrated in (**b**). *Gabbroic-enriched* (a-i) eclogites show positive Eu anomalies (Eu* = 1.1–1.6), and relative enriched LREE patterns (Ce/Sm = 1.8–3.5). Both *Basaltic-enriched* (a-ii) and *Basaltic* (a-iii) eclogites lack Eu anomalies (Eu* = 0.9–1.1), where the former has enriched LREE (Ce/Sm = 2.1–3.6) and the latter is variably depleted in the LREEs (Ce_N/Sm_N = 0.01–1.0). N-MORB normalization values from Gale et al. (2013).

summary, uncertainties of 0.6 log units are absolute minimum estimates for the calculated oxygen fugacities of the Palmietfontein eclogite xenoliths from the central Kaapvaal craton.

5.5. Calculated bulk eclogite compositions and classification

Measured whole-rock mantle xenolith compositions are typically compromised by infiltration with and metasomatism by the transporting kimberlite magma (Schmidberger and Francis, 2001; Barth et al., 2001), and thus bulk xenolith compositions are generally calculated from mineral compositions and modal mineral abundances (Tappe et al., 2011; Smart et al., 2009). Determinations of accurate modal mineral abundances for the Palmietfontein eclogite xenoliths are prevented because of small nodule sizes (maximum 2 cm in length) coupled with coarse crystal sizes (up to 5 mm). Therefore, modes of 55 wt% garnet and 45 wt% clinopyroxene were applied to all eclogite xenoliths studied (see Aulbach and Jacob, 2016). The whole-rock compositions of eclogite xenoliths Palm-10, −12 and − 18 were calculated incorporating amphibole modal abundances between 5 and 10 wt% (Table 2). Calculated bulk eclogite compositions are given in Table 6 and displayed in Figs. 7 and 8.

The Palmietfontein eclogites have calculated whole-rock MgO contents from 8.1 to 16.4 wt%, and the amphibole-bearing eclogites have some of the highest MgO contents (>15 wt%). Eclogite MgO contents

form a positive array with SiO$_2$ (46.2–48 wt%) and negative arrays with Al$_2$O$_3$ (14–17.6 wt%), FeO (7.9–13.9 wt%), and Na$_2$O (1.7–2.9 wt%; Fig. 7). The Palmietfontein eclogites are grouped based on N-MORB normalized REE patterns and the presence of positive Eu anomalies (Eu* = [2*Eu]/[Sm + Gd] using N-MORB-normalized values), which are generally thought to indicate oceanic crustal gabbroic precursors (e.g. Aulbach and Jacob, 2016; Smart et al., 2017; Fig. 8). Twelve out of 17 Palmietfontein eclogite samples show incompatible trace element enrichments with negatively sloped LREE patterns (Ce/Sm = 1.5–4.3); nine of these enriched eclogites are identified as "*gabbroic-enriched*" due to the presence of positive Eu anomalies from 1.1–1.6 (Fig. 8a-i), whereas the remaining three eclogite samples lack Eu anomalies (Eu* ~ 1; Fig. 8a-ii) and are identified as "*basaltic-enriched*". Five out of 17 Palmietfontein eclogite xenoliths have flat to depleted LREE patterns (Ce/Sm = 0.003–1.0) without Eu anomalies (Eu* = 0.99–1.1), and are identified as "*basaltic*" eclogites (Fig. 8a-iii). The *enriched* gabbroic and basaltic eclogites have higher contents of Th (0.03–0.37 ppm), Sr (102–229 ppm) and Pb (0.59–1.38 ppm) compared to the more depleted or less enriched basaltic eclogites (Th ≤ 0.09 ppm, Sr ≤ 153 ppm and Pb ≤ 0.92 ppm), but all eclogite xenoliths have overlapping Ti-Zr-Hf concentrations. Notably, the "*basaltic*" eclogites that lack trace element enrichment have the lowest MgO (8.1–12.3 wt%) and among the highest Na$_2$O (1.8–2.9 wt%) and Al$_2$O$_3$ (15.7–17.6 wt%) contents. In contrast, *enriched* eclogites with the highest bulk MgO (>16 wt%) also have the
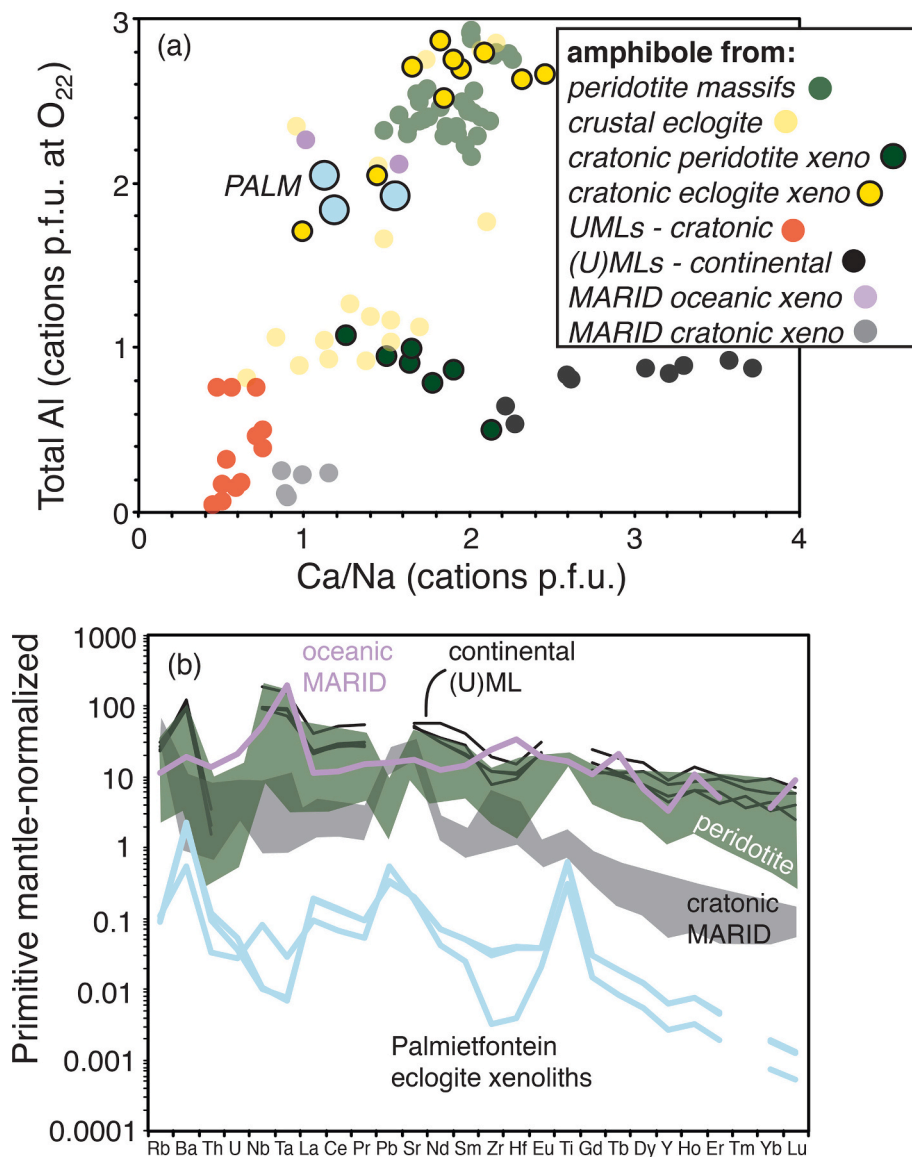
Fig. 9. (a) Al vs. Ca/Na contents of amphiboles from the Palmietfontein eclogites Palm-10, −12 and − 18. The Palmietfontein amphiboles are compositionally distinct from most secondary metasomatic amphibole derived from cratonic mantle eclogite xenoliths (Hills and Haggerty, 1989), veins in peridotite massifs (e.g. Lherz, Beni Bousera; Fabriès et al., 2001; El Atrassi et al., 2014; Zanetti et al., 1996), as well as UHP crustal eclogites (Massone, 2012; Okay, 1995; Zack et al., 1997; Spandler et al., 2003; Enami et al., 1995). Additionally, amphibole found in metasomatized peridotite xenoliths (Ionov and Hoffman, 1995), ultramafic lamprophyres in continental (Orejana et al., 2008) and cratonic settings (Tappe et al., 2004), as well as volatile-rich metasomatic "MARID-type" xenoliths in cratonic (Grégoire et al., 2002) and oceanic settings (Smart et al., 2019) have distinctly lower-Al compositions. (b) Primitive-mantle normalized multi-element trace element patterns of the Palmietfontein amphibole. The Palmietfontein amphiboles are comparatively trace element-depleted compared to amphibole from metasomatic MARID-type xenoliths, ultramafic lamprophyres, and amphibole derived from metasomatic peridotite xenoliths and massif veins (references as in (a)). Primitive mantle values from Palme and O'Neill (2003).

highest incompatible trace element contents (e.g. La > 3 ppm and Sr > 200 ppm). The Palmietfontein eclogite xenoliths display variably fractionated HREE patterns (Yb/Gd = 0.8–3).

6. Discussion

Mantle eclogite xenoliths are widely interpreted as fragments of oceanic lithosphere recycled into the cratonic mantle since the Archean. The key pieces of geochemical evidence for this hypothesis include bulk eclogite major element compositions consistent with low-pressure igneous differentiation at ~1 GPa, possibly impacted by the effects of partial melt extraction (shown in Fig. 7), and bulk eclogite REE patterns boasting positive Eu anomalies indicative of plagioclase-bearing gabbroic protoliths (Fig. 8 Aulbach and Jacob, 2016). This geochemical evidence is often supported by mineral $\delta^{18}O$ values that are both higher and lower than the mantle average, which resulted from fractionation induced by near-surface seawater interaction (Table 4; Gregory and Taylor Jr, 1981). Eclogite xenolith suites from the Kaapvaal craton, including the Palmietfontein samples, bear most of these petrogenetic fingerprints and thus likely have igneous protoliths from within former oceanic crust. However, unlike other xenolith suites of Kaapvaal mantle eclogites that have Archean formation ages linked to

ca. 2.9 Ga subduction and craton suturing events (Shirey et al., 2001; Schmitz et al., 2004), age information is not available for the Palmietfontein eclogites. The Palmietfontein eclogites bear several distinctive features that set them apart from other Kaapvaal eclogite suites: residence at relatively shallow mantle depths of ~100 km; the occurrence of euhedral, coarse "primary" amphibole; omnipresent incompatible trace element enrichment, and Pb isotopic compositions that overlap with those of Group-2 kimberlites. Altogether, these features speak to a unique eclogite petrogenesis and will be examined below considering the >3 billion year evolution of the Kaapvaal craton.

6.1. The role of metasomatism in the formation of amphibole-bearing eclogites

The study of mantle eclogite xenoliths is fundamental for understanding deep geochemical cycles through time, because the igneous protoliths of many eclogite suites are basalts and gabbros that formed within Archean and Paleoproterozoic oceanic lithospheres (Aulbach and Viljoen, 2015; Jacob et al., 1994; Tappe et al., 2011; Smart et al., 2014, 2017; Schmidberger et al., 2007; Shu et al., 2016). For the Kaapvaal craton specifically, mantle eclogite xenoliths have maximum ages of ca. 3–3.2 Ga (e.g. Shirey et al., 2001; Shu et al., 2016), which, when
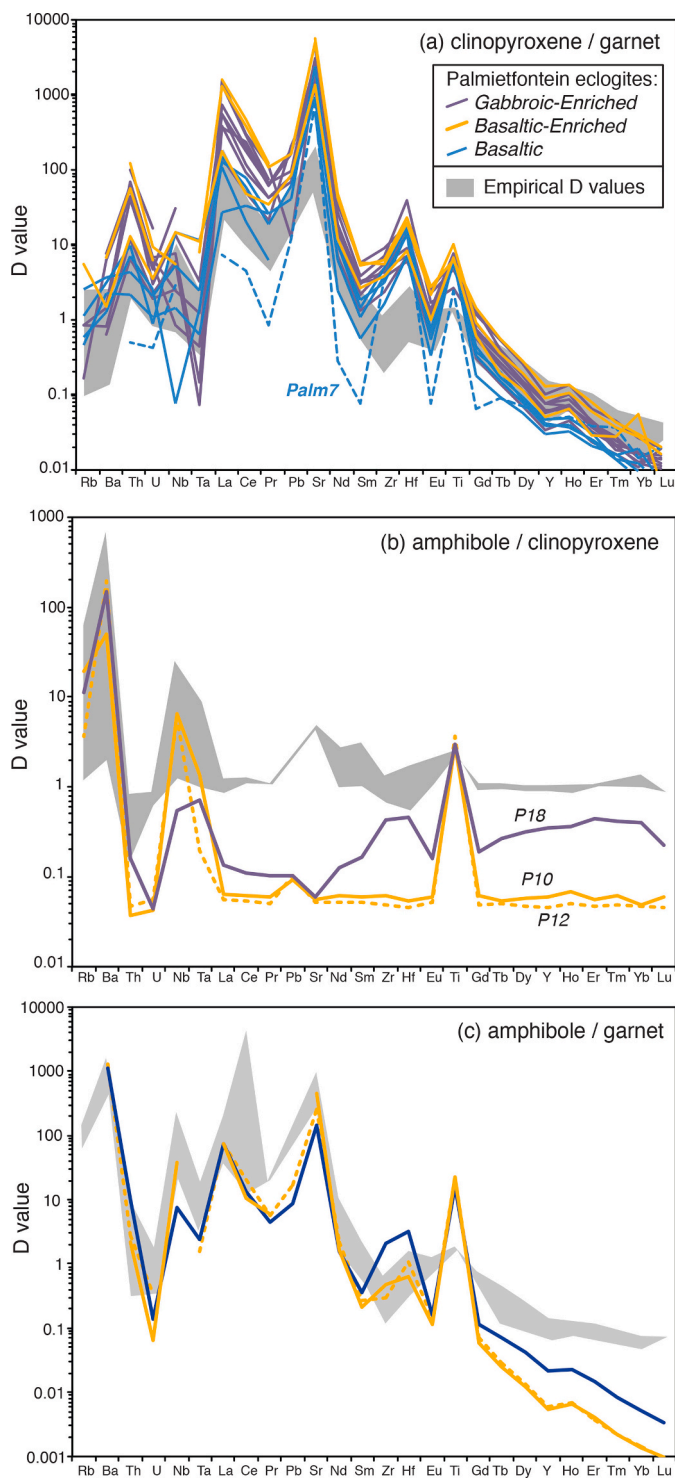
Fig. 10. Calculated partition coefficients of trace elements between **(a)** clinopyroxene and garnet, **(b)** clinopyroxene and amphibole, and **(c)** garnet and amphibole for the Palmietfontein eclogites. Grey fields represent partition coefficients determined from both experimental studies (Green et al., 2000; Adam and Green, 2006; Xiong, 2006) and natural eclogite samples (Zack et al., 1997). Trace element classes as described in **Section 5.5** and **Fig. 8**. (For interpretation of the references to colour in this figure legend, the reader is referred to the web version of this article.)

combined with the generally much younger timing of host kimberlite magma eruptions between 50 and 250 Ma (Tappe et al., 2018a), results in a prolonged mantle residence that renders the eclogites susceptible to metasomatic overprinting, masking the geochemical and isotopic characteristics of the protoliths. Metasomatism may occur during subduction by circulating slab-derived melts and fluids ("autometasomatism"; e.g. Halama et al., 2011; John et al., 2012; Aulbach et al., 2016), but is also commonly envisaged to occur within the mantle lithosphere by percolating volatile-bearing silica-undersaturated media such as alkali basaltic, carbonatitic, or kimberlitic, as well as high-density fluids (collectively termed "mantle metasomatism"; Huang et al., 2012; Aulbach et al., 2020; Smart et al., 2009; Jacob et al., 2009; Mikhail et al., 2019). Because mantle eclogites are generally though to have oceanic crustal protoliths (Aulbach and Jacob, 2016), eclogitization of former oceanic basalts and gabbros at pressures above 2 GPa during subduction (±fluid/melt removal; Schmidt and Poli, 2014) should result in volatile-free biminerallic garnet-clinopyroxene rocks that may contain minor to trace amounts of rutile, kyanite and coesite (Yaxley and Sobolev, 2007). It follows that mantle eclogites should have trace element characteristics that largely resemble the precursor, subduction-modified oceanic basalts and gabbros (Barth et al., 2001), including MORB-like flat or slightly depleted (due to mineral accumulation or partial melting; Smart et al., 2017) REE patterns that may contain Eu anomalies due to plagioclase accumulation in the protolith (Aulbach and Jacob, 2016). Therefore, mantle eclogite xenoliths that contain volatile-bearing phases (e.g. amphibole, phlogopite, diamond), or bear LILE and LREE enrichments, or even have anomalously high Mg and Ca contents, have probably interacted with volatile-bearing melts and/or fluids causing metasomatism (Smart et al., 2009; Tappe et al., 2011; Aulbach et al., 2020; Jacob et al., 2009; Barth et al., 2001; Mikhail et al., 2019).

The presence of amphibole in three Palmietfontein eclogite xenoliths, plus the pervasive LREE-enrichment observed in the suite, cursorily suggest that these rocks interacted with an enriched, hydrous metasomatic agent. Metasomatic secondary amphiboles in mantle eclogite xenoliths are known to occur as minor (<1 vol%) and fine-grained (<1 mm) subhedral crystals along cracks and grain boundaries (Hills and Haggerty, 1989). However, in the Palmietfontein eclogite xenoliths, amphibole occurs as coarse-grained, euhedral crystals that form an interlocking equilibrium texture with garnet and clinopyroxene (Fig. 2b; Figure A1b). The amphiboles are calcic to sodic-calcic in composition (i.e., pargasite and katophorite) with elevated Al_2O_3 contents of up to 12 wt% but low K_2O contents <1 wt%. These compositions are distinctly different from richteritic amphiboles as found in heavily K-metasomatized mantle xenoliths such as members of the MARID suite (Grégoire, 2002; Fitzpayne et al., 2018), and potassic mafic-ultramafic magmas that carry diamonds (Tappe et al., 2004; Howarth et al., 2011; Ngwenya and Tappe, 2020) (Fig. 9a). Furthermore, amphibole hosted in metasomatic mantle xenoliths is enriched in incompatible trace elements (Grégoire et al., 2002; Grégoire et al., 2005; Smart et al., 2019), which stands in sharp contrast to the comparatively depleted amphiboles in the Palmietfontein eclogite xenoliths (Fig. 9b). Texturally and geochemically the Palmietfontein amphiboles do not appear to have a metasomatic origin, although growth during hydrous basaltic metasomatism cannot be fully excluded (e.g. Grégoire et al., 2005). It is most plausible that these amphiboles present part of the metamorphic phase assemblage that formed during prograde mineral reactions within a mafic igneous protolith towards eclogite-facies conditions, and the presence of minor "primary" amphibole is in agreement with the relatively shallow equilibration depths of the Palmietfontein eclogite xenoliths (Fig. 6a).

During prograde metamorphism of oceanic basalts in relatively cool subduction zones, characteristic sodic amphibole such as glaucophane forms as the mafic lithologies enter into blueschist facies PT conditions. Glaucophane will persist in cold subduction zones well into the eclogite facies (Bang et al., 2021; Spandler et al., 2003). The presence of calcic and calcic-sodic amphiboles, instead of glaucophane, in our samples
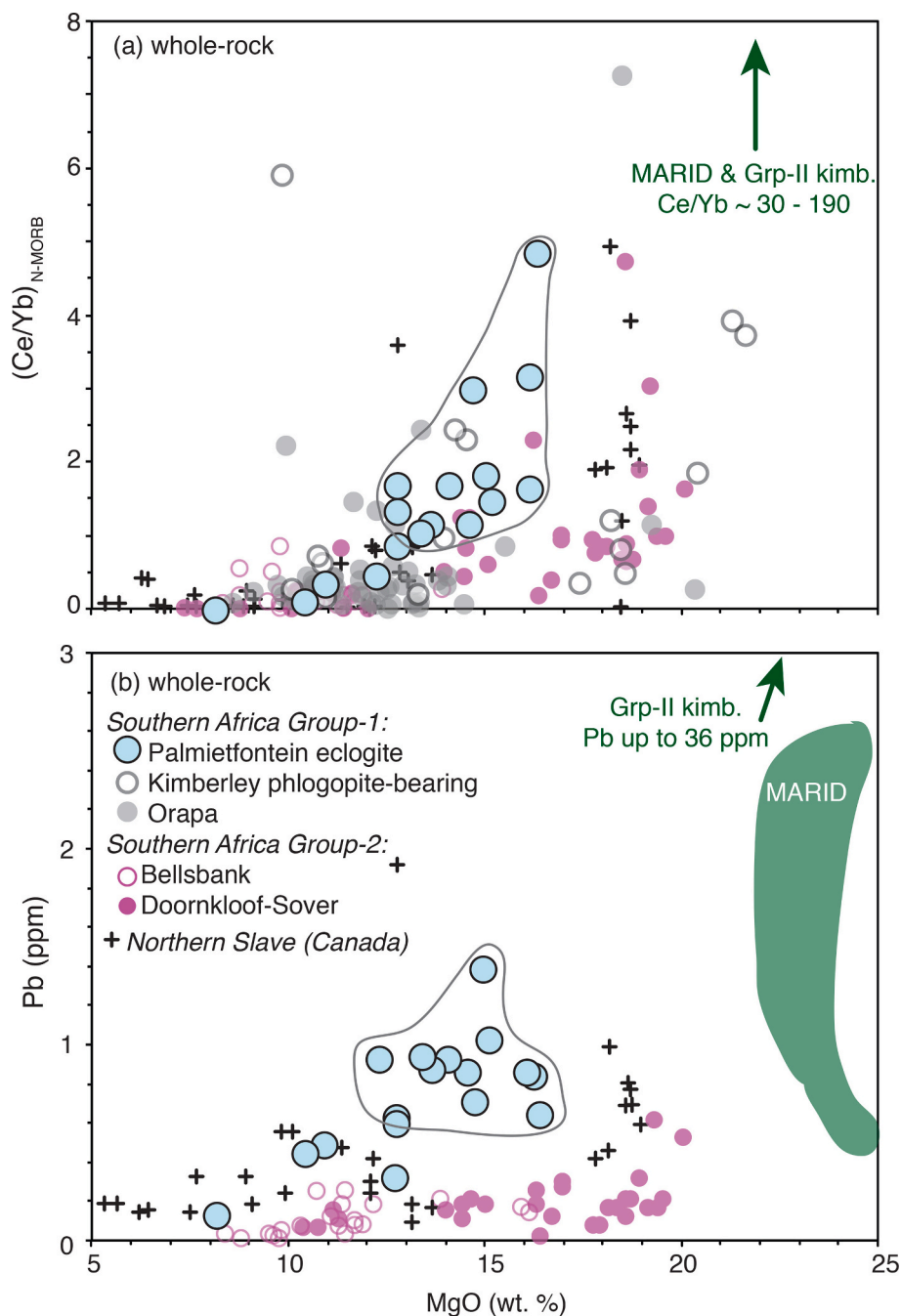
Fig. 11. Enrichment in bulk eclogite MgO contents and **(a)** (Ce/Yb)$_{NMORB}$ and **(b)** Pb contents suggests the activity of a ultramafic, incompatible element enriched metasomatic agent beneath the northern Kaapvaal craton. Palmietfontein eclogites with "enriched" trace element signatures are encircled. Eclogite xenoliths from other Kaapvaal Group-1 (Kimberley, Orapa; Jacob et al., 2009; Aulbach et al., 2017b) and Group-2 kimberlites (Bellsbank, Doornkloof-Solver; Smart et al., 2021; Aulbach et al., 2020b) shown for comparison. Metasomatized eclogites from the Northern Slave craton from Smart et al. (2009, 2014) also shown for comparison. Fields for MARID metasomatic xenoliths from Grégoire et al., 2002 and Group-2 kimberlite from Becker and le Roex (2006).

may be attributed to Mesoarchean to Paleoproterozoic eclogite 'formation events' that led to the assembly and modification of the Kaapvaal craton lithosphere (e.g. Shirey et al., 2001; Timmerman et al., 2017). On the Early Earth, warmer subduction zone geotherms (Korenaga, 2008; Hawkesworth et al., 2017) largely impeded high-pressure / low-temperature metamorphic conditions that are required for blueschist formation (e.g. Stern, 2005). Furthermore, Archean to Paleoproterozoic oceanic crust was probably more Mg-rich compared to modern oceanic basalts (Herzberg et al., 2010). Under these PTX conditions, glaucophane formation is strongly limited and only occurs in a narrow pressure-temperature interval displaced from the warmer subduction zone geotherms on the Early Earth (Palin and White, 2016). In other words, subduction of high-MgO basalts (~14–16 wt% MgO), similar in composition to the bulk Palmietfontein eclogite xenoliths with up to 16.4 wt% MgO (Table 6), would promote calcic amphibole formation as

part of the eclogite facies metamorphic mineral assemblage (Palin and White, 2016), which explains the presence of pargasitic amphibole and the absence of glaucophane in the eclogites studied.

The origin of the Palmietfontein eclogite LREE-enrichment, as well as the "primary" origin of the amphibole can be interrogated considering the trace element distribution between the apparent equilibrium mineral phases. Chemical elements partition between coexisting minerals as a function of pressure, temperature and compositional variations, and, importantly, for bimineralic eclogite assemblages trace elements are increasingly incorporated into garnet with increasing bulk eclogite Ca content (Harte and Kirkley, 1997). Thus, garnet with low Ca content coexists with clinopyroxene that is increasingly enriched in, for example, the LREE to MREE, Sr, and Y (Harte and Kirkley, 1997; Aulbach et al., 2016). In agreement with previous studies, Palmietfontein eclogitic garnet Ca contents (expressed as Ca#; see Table 2 and Section
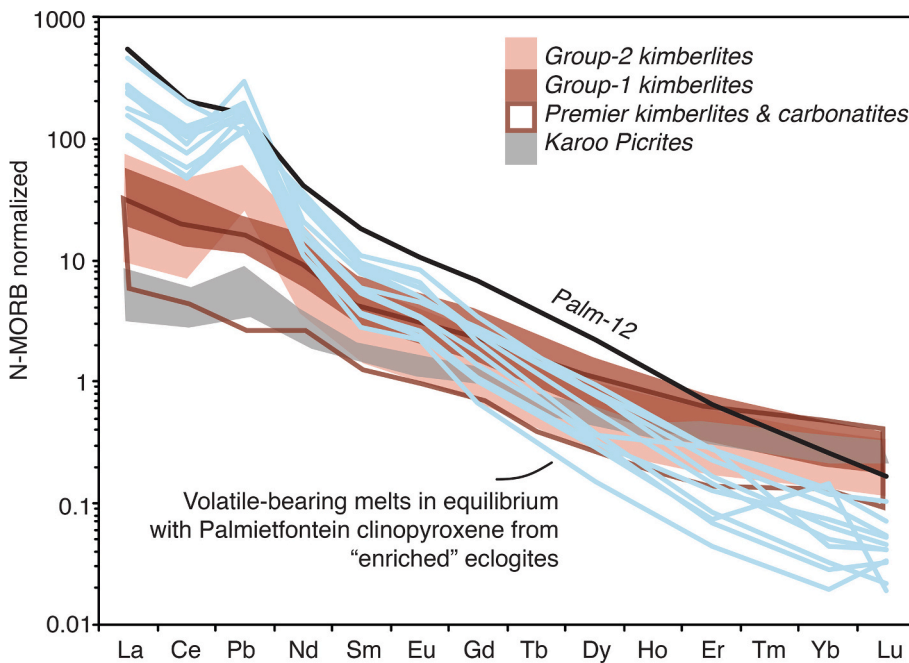
Fig. 12. Calculated volatile-bearing liquids in equilibrium with clinopyroxene from the "enriched" group of Palmietfontein eclogites exhibit broad similarities to ca. 120 Ma Group-2 Kaapvaal kimberlites. Clinopyroxene-melt partition coefficients for CO_2-bearing incipient melts from Dasgupta et al. (2009). Trace element compositions of Group-1 and Group-2 kimberlites are from Becker and le Roex (2006), the nearby 1135 Ma Premier Group-1 kimberlite from Tappe et al. (2020) and the ca. 180 Ma Karoo picrites from Jourdan et al. (2007) are shown for comparison. Normalization values from Gale et al. (2013).

4.1) correlate inversely with $D^{cpx/grt}$ values for Sr, Th, U, Zr, Hf, Y, and La through Er. However, garnet Ca contents do not show any relationships with Ti, Pb or Nb (Figure A5). Clinopyroxene/garnet and clinopyroxene/amphibole partition coefficients for the incompatible elements Th, Sr, Pb, Zr, Hf and the LREE in the "*enriched*" eclogites are consistently higher than those determined from high-pressure (>2 GPa) experiments in mafic-ultramafic systems (Green et al., 2000; Xiong, 2006; Adam and Green, 2006; Fig. 10a,b), suggesting that clinopyroxene is not in trace element equilibrium with garnet and amphibole. Some of the observed incompatible trace element enrichment in clinopyroxene may be related to the crystal chemical controls described above, because the "*enriched*" gabbroic and basaltic eclogites have much lower garnet Ca# of 0.1–0.23 compared to higher values of 0.18–0.27 for the more depleted "*basaltic*" eclogites. Applying a correction for eclogite Ca contents using eq. (1) in Harte and Kirkley (1997) variably reduces the Palmietfontein $D^{cpx/grt}$ values; for example, maximum $D^{cpx/grt}$ values change for La from 1605 to 64 (*versus* a maximum experimental value of 51; Green et al., 2000), for Ce from 477 to 26 (vs. 19), for Sr from 8170 to 930 (vs. 140) and for Zr from 9.1 to 2.9 (vs. 0.44). Some of the corrected $D^{cpx/grt}$ values show apparent garnet – clinopyroxene equilibrium, but overall the Palmietfontein eclogitic clinopyroxene shows clear enrichments in some LREE and HFSE. In contrast, the three amphibole-bearing eclogites have $D^{amph/grt}$ values that reconcile well with experimentally determined partitioning values, excluding some mismatches observed for Zr, Hf, Ti and the HREE (Fig. 10c). This finding suggests that clinopyroxene - not amphibole - is in trace element disequilibrium within the "*enriched*" class of Palmietfontein eclogite xenoliths and thus may have a secondary, metasomatic origin.

6.2. Nature and timing of enrichment of the central Kaapvaal cratonic mantle

The Palmietfontein "*enriched*" eclogite groups have comparatively higher bulk contents of incompatible elements such as Th, Sr, Pb, the LREE-MREE, as well as higher bulk MgO, CaO and SiO_2 contents (and lower Al_2O_3), compared to the more depleted "*basaltic*" eclogites (Fig. 11a,b). These "*enriched*" eclogites contain clinopyroxene that has elevated incompatible trace element contents (Fig. 10a) and could possibly be related to the presence of ubiquitous secondary diopside-rich rims (with up to 21 wt% CaO; Figure A1b, Fig. 4b) observed on primary

omphacitic clinopyroxene. The linked incompatible trace element and Mg-Ca enrichment trends shown by the Palmietfontein eclogites are very similar to the "carbonated ultramafic" metasomatism described by Aulbach et al. (2020), where similar geochemical effects (increases in bulk MgO, SiO_2, LREE, Sr, Pb, Th, U, Zr, Nb and decreases in Al_2O_3) were observed in up to 40% of eclogite xenoliths studied from kimberlite localities worldwide. Aulbach et al. (2020) suggested that this carbonated ultramafic metasomatism caused formation of high-temperature jadeite-poor pyroxene, similar to the diopside-rich rims observed on the Palmietfontein eclogitic clinopyroxene. The carbonated ultramafic metasomatic agent is envisioned to be similar to incipient volatile-bearing "proto-kimberlitic" melts that may form a ubiquitous network near the lithosphere – asthenosphere interface, and is responsible for secular metasomatism of the cratonic mantle (Tappe et al., 2017, 2018). Metasomatism of the Kaapvaal cratonic mantle by such melts has long been recognized, from both the formation of discrete "metasomatic" MARID and PIC lithologies (Dawson and Smith, 1977; Grégoire et al., 2002; Fitzpayne et al., 2018), and the enriched geochemical and isotopic compositions of peridotitic and eclogitic xenoliths (Grégoire et al., 2003; Simon et al., 2007; Rehfeldt et al., 2008; Huang et al., 2012; Tappe et al., 2021). Using partition coefficients between CO_2-bearing near-solidus melts and clinopyroxene from Dasgupta et al. (2009), calculated melts in equilibrium with the Palmietfontein "*enriched*" clinopyroxene are incompatible trace element enriched (NMORB-normalized La contents from ~30–500), with steeply-sloping REE patterns and positive spikes for Pb (Fig. 12), reminiscent of both Group-1 and Group-2 kimberlites as well as associated carbonatites on the Kaapvaal craton (Becker and le Roex, 2006; Tappe et al., 2020).

Metasomatism of the central Kaapvaal lithospheric mantle by proto-kimberlitic melts can be further explored considering the Pb isotopic compositions of clinopyroxene from the Palmietfontein eclogite xenoliths. The $^{206}Pb/^{204}Pb$ – $^{207}Pb/^{204}Pb$ isotope systematics of the Palmietfontein eclogites do not form a linear array with age significance (see Section 5.3), which is in contrast to ca. 1.8 Ga Pb-Pb secondary isochrons defined by clinopyroxene from eclogites of the Northern Slave craton (Schmidberger et al., 2007; Smart et al., 2014, 2017). Instead of providing clear age information, the Palmietfontein Pb isotope data form a diffuse cluster between $^{206}Pb/^{204}Pb$ = 17 to 18, which overlaps with the Pb isotopic compositions of Kaapvaal Group-2 kimberlites (Fraser et al., 1985) and the petrogenetically related MARID suite of

metasomatic xenoliths (e.g. Grégoire et al., 2002; Fitzpayne et al., 2019) (Fig. 13a). Combined with the inverse melt modelling discussed above, it is reasonable to argue that the Palmietfontein eclogites were overprinted by "MARID-type" metasomatism that was probably associated with regional Group-2 kimberlite magmatism during the Mesozoic. Kobussen et al. (2012), from a study of >6700 Group-1 kimberlite-derived garnet megacrysts, also found extensive evidence for Group-2

kimberlite-related metasomatic overprinting of the Kaapvaal cratonic mantle exemplified by strong Ti-Zr enrichments in garnet, and this geochemical overprint is generally referred to as "phlogopite" or "MARID"-style metasomatism (Grégoire et al., 2003). For the central Kaapvaal craton additional Fe enrichment suggests a basalt-driven metasomatic event, possibly related to the proximal Paleoproterozoic Bushveld intrusion, and the younger Ti-Zr enrichment may be
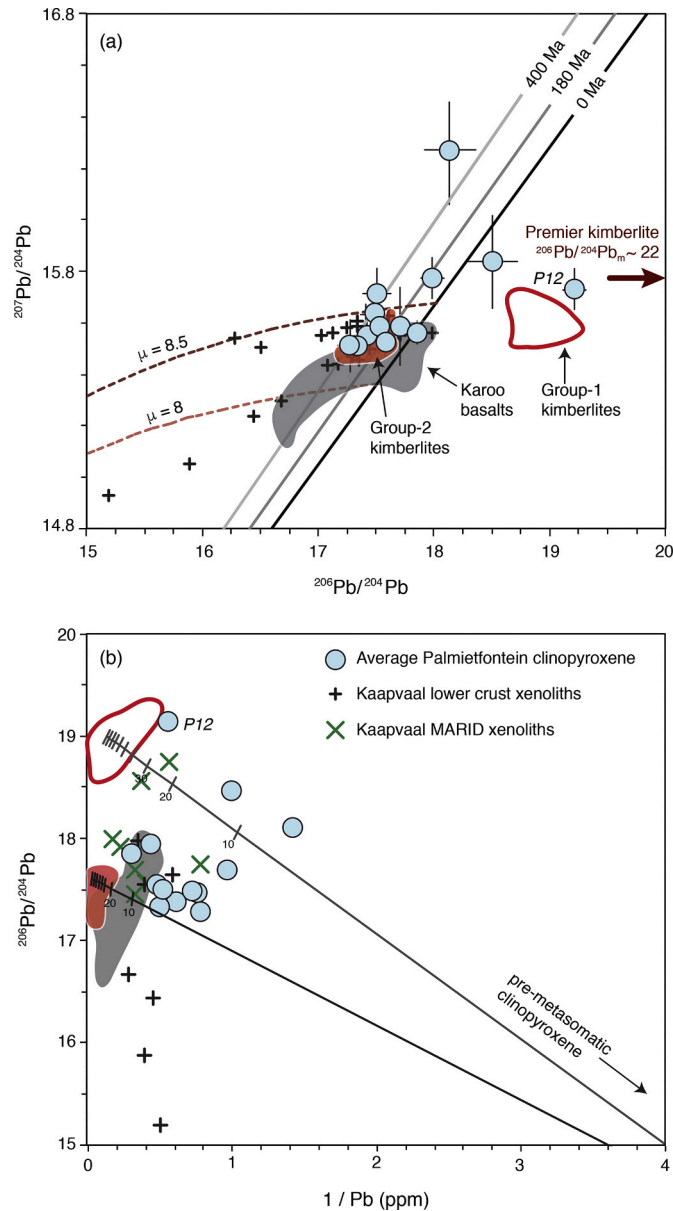

Fig. 13. **(a)** Average present-day $^{206}Pb/^{204}Pb$ – $^{207}Pb/^{204}Pb$ isotope compositions for clinopyroxene from the Palmietfontein eclogite xenoliths ($n = 5$ clinopyroxene per xenolith; error bars are 2σ). The clinopyroxene have low measured U/Pb and μ values, and thus calculated initial Pb isotope ratios at the time of kimberlite eruption at 75 Ma are within the 2σ uncertainty of the displayed present-day Pb values. Shown for comparison are the ~180 Ma Karoo basalts and picrites (Jourdan et al., 2007), ca. 2.5–2.9 Ga Kaapvaal lower crustal xenoliths (Huang et al., 1995), ~ 90 Ma Group-1 and ~ 120 Ma Group-2 kimberlites (Smith, 1983). Also displayed are the positions of the Geochron at 0, 180 and 400 Ma, as well as single-stage Pb evolution curves with μ values of 8 and 8.5, using initial values of Canyon Diablo Troilite. **(b)** The Pb isotope systematics of the Palmietfontein eclogites may be explained as mixing products of Archean oceanic crustal eclogite protoliths and Phanerozoic metasomatic agents. The "pre-metasomatic" eclogite precursors are assumed to be Archean oceanic crust, as is proposed for many suites of Kaapvaal eclogites (e.g. Aulbach and Jacob, 2016), with Pb concentrations of 0.2 ppm approximated from average subducted oceanic crust (Gale et al., 2013; Bach et al., 2001) that has undergone dehydration and/or melt loss during subduction processing (Pb partition coefficient for bulk eclogite = 0.156; Klemme et al., 2002). This estimated pre-metasomatic eclogite Pb content is also similar to median clinopyroxene Pb concentrations (0.08–0.3 ppm) from several Kaapvaal eclogite suites (Aulbach and Viljoen, 2015; Aulbach et al., 2019) that have between Mesoarchean to Paleoproterozoic model and secondary isochron ages. The pre-metasomatic eclogite is assumed to have $^{206}Pb/^{204}Pb = 14$, similar to the least-radiogenic isotope composition (13.6) of the ca. 2.9 Ga Lace eclogite suite mentioned previously, and is also similar to the $^{206}Pb/^{204}Pb$ isotope composition at ~2.5 Ga on the Stacey-Kramers two-stage terrestrial Pb evolution curve. The Pb isotope compositions and contents of potential Phanerozoic metasomatic agents are taken from Kaapvaal Group-1 and -2 kimberlites of Smith (1983).

superimposed onto this ancient metasomatic event. However, recent work on peridotite xenoliths from the Premier kimberlite pipe some 150 km southeast of Palmietfontein (Fig. 1) showed that metasomatic imprints from a hypothetical Bushveld mantle plume are unlikely to be preserved, and most if not all of the identified geochemical enrichment can be readily generated by kimberlitic and carbonatitic liquids shortly prior to the magmatic event that led to entrainment of the mantle xenoliths (Tappe et al., 2021).

Lead isotopic and elemental mixing arrays between a hypothetical eclogite protolith (e.g. Precambrian seawater-altered oceanic crust) and

Kaapvaal kimberlites are shown in Fig. 13b. Most of the analysed Palmietfontein clinopyroxene crystals have Pb isotope and elemental characteristics that fall along a mixing array with Group-2 kimberlites and MARID xenoliths, excluding four samples that have $^{206}Pb/^{204}Pb$ ratios of >18; these samples instead fall along a mixing array with ca. 90 Ma Group-1 kimberlites. In summary, the Palmietfontein eclogites preserve a metasomatic record of the older ca. 120 Ma Group-2 kimberlite / MARID magmatic event, and several eclogite xenoliths have experienced an additional overprint by the younger ca. 90–75 Ma Group-1 kimberlite magmatic event.
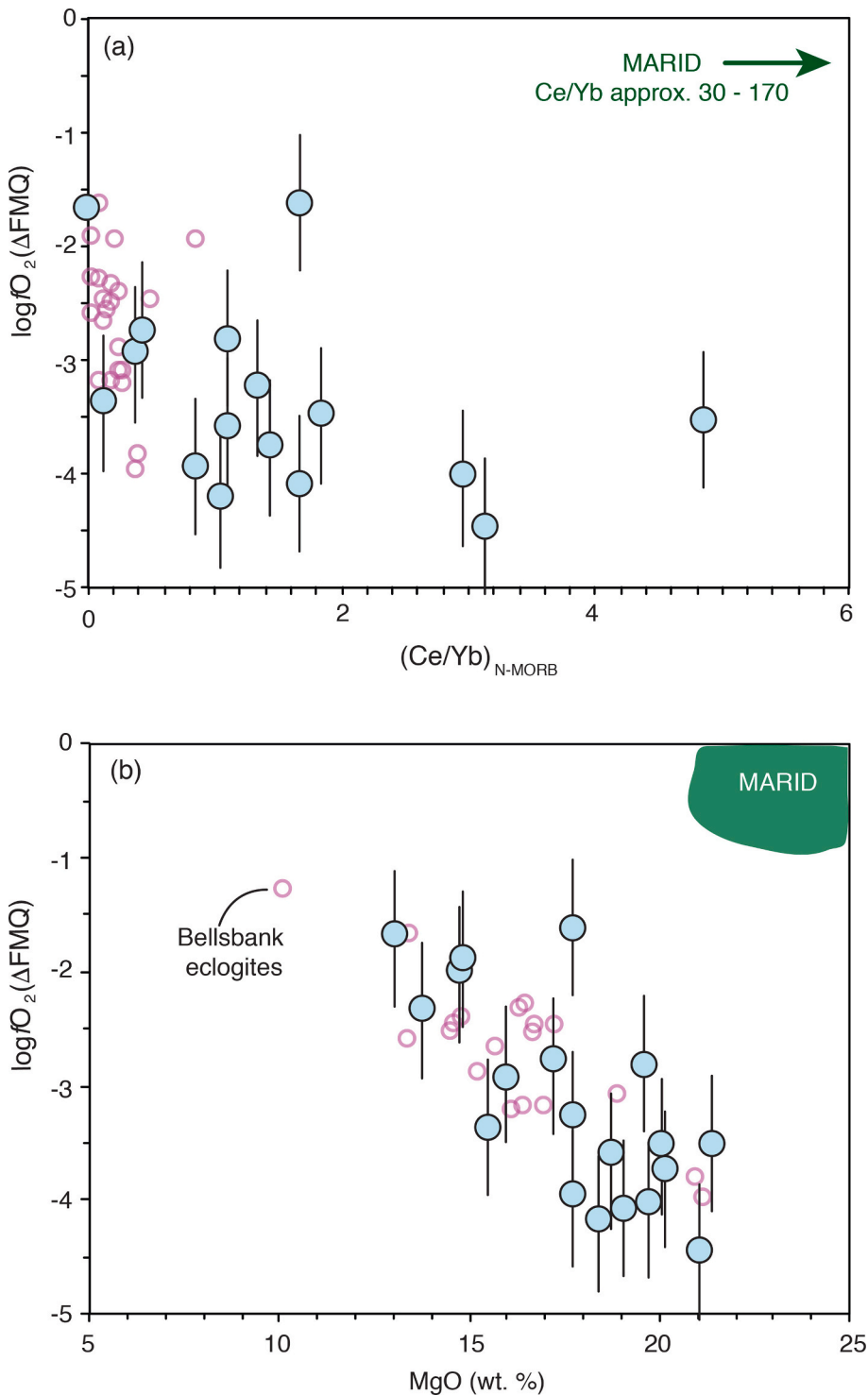
Fig. 14. Palmietfontein eclogite oxygen fugacity, displayed as log$f$O$_2$ relative to the FMQ buffer (see Table 5) compared to **(a)** bulk eclogite N-MORB normalized Ce/Yb and **(b)** MgO contents. No correlation is observed between eclogite oxygen fugacity and geochemical indices of metasomatism, shown here as (Ce/Yb)$_{NMORB}$. A weak correlation exists between eclogite fO$_2$ values and bulk MgO contents, and likely represents a relict of igneous fractionation processes. MARID fields from Grégoire et al., 2002 and Creighton et al. (2009).

Previous investigations of Kaapvaal peridotite xenoliths have shown that metasomatism is often accompanied by net-oxidation (Woodland and Koch, 2003; Lazarov et al., 2009; Hanger et al., 2015), where metasomatized peridotites have P-T-fO$_2$ systematics that fall away from the expected trend of lower oxygen fugacity with increasing pressure/depth (Wood et al., 1990; Frost and McCammon, 2008). Creighton et al. (2009) calculated the oxidation states of MARID xenoliths for between 80 and 180 km depths, i.e. from mid-lithospheric depths down to the Kaapvaal craton base. They found that MARID materials have fO$_2$ values 1 to 3 log units higher than the coexisting "unmetasomatized" peridotitic mantle (Lazarov et al., 2009; Woodland and Koch, 2003). At ~110 km depth, equivalent to the average residence depth for the Palmietfontein eclogites, MARID materials have oxidized compositions with log$f$O$_2$ values around FMQ (Fig. 6b). Thus, as observed in Kaapvaal peridotite xenoliths, it could be predicted that "MARID-style" metasomatism of the Palmietfontein eclogites would also result in an overall oxidation; however, such "oxidative metasomatism" is not observed in the eclogite xenoliths studied. In Fig. 14, Palmietfontein eclogite fO$_2$ values do not correlate with other geochemical indicators of metasomatism, such as bulk eclogite N-MORB-normalized (Ce/Yb) (Fig. 14a), or Pb and Th contents (r^2 = 0.16, 0.18 and 0.19, respectively). Instead, the fO$_2$ values present weak negative correlations with bulk eclogite MgO (Fig. 14b) and Sr contents (not shown; r^2 = 0.35), which may be related to crystal fractionation processes during formation of the gabbroic and basaltic protoliths (Smart et al., 2017, 2021). Alternatively, given that the eclogite xenoliths with the strongest indication of melt metasomatism (e.g. high incompatible trace element contents) show the lowest fO$_2$ values, it can be inferred that the metasomatic event that affected the Palmietfontein eclogites was relatively reduced in nature (see Burness et al., 2020). However, this is not expected given the relatively oxidized nature of metasomatic agents of carbonatitic (Braunger et al., 2020), kimberlitic (Yaxley et al., 2017) and lamproitic (Creighton et al., 2009; Ngwenya and Tappe, 2020) compositions, unless the fO$_2$ of metasomatic agent was modified by previous interaction with the mantle lithosphere.

6.3. Central Kaapvaal eclogites and link to a mid-lithospheric discontinuity

As established in Section 6, the Palmietfontein eclogites reveal the hallmark features of oceanic mafic protoliths, including positive Eu anomalies and δ^{18}O values from 5.5–6.9‰. These δ^{18}O values are generally higher than those of garnets derived from peridotite xenoliths and peridotitic-type diamonds, which have average values of approximately 5.3 ± 0.2‰ (Lowry et al., 1999; Schulze et al., 2003). However, the petrogenesis of the Palmietfontein eclogite xenoliths is complicated by metasomatic enrichment linked to ca. 120 Ma Group-2 kimberlite magmatism and the consanguineous MARID-style overprinting of the Kaapvaal craton mantle lithosphere. We suggest that the relatively shallow mean equilibration pressures of ~3.3 GPa (~110 km depth) for the Palmietfontein eclogites and their pervasively overprinted geochemical compositions are not coincidental. The Palmietfontein eclogites reside between 90 and 150 km depths, a horizon that coincides with a seismically detected mid-lithospheric discontinuity in the Kaapvaal cratonic lithosphere (Sodoudi et al., 2013; Wittlinger and Farra, 2007). Mid-lithospheric discontinuities have been argued to represent metasomatic fronts; that is, depth horizons within the conductive mantle lithosphere marked by focussed crystallization of 'low-velocity' hydrous minerals, such as amphibole and phlogopite, from volatile-rich low-volume melts (Aulbach et al., 2017a). The Palmietfontein eclogites not only match the depth of origin of the Kaapvaal craton mid-lithospheric discontinuity but also carry the geochemical imprint of such intensive metasomatism caused by volatile-rich melts. The Pb isotope compositions of the Palmietfontein eclogites do not provide compelling evidence for igneous protolith formation because the model ages of ca. 3.3, 2 and 1 Ga (Fig. A3) may variably correspond to oceanic lithosphere formation

during the Archean (Shirey et al., 2001; Shu et al., 2016), picritic magma underplating related to the Paleoproterozoic Bushveld large igneous event (Richardson and Shirey, 2008), or volatile-rich alkaline to carbonatitic-kimberlitic magmatic activity on the central Kaapvaal craton during the Mesoproterozoic (e.g. Pilanesberg alkaline complex; Spitskopf carbonatite complex, Premier kimberlite cluster) (Harmer, 1999; Tappe et al., 2018b; Elburg and Cawthorn, 2017). The most straightforward interpretation of the Pb isotope mixing relationships shown in Fig. 13a is, however, strong compositional overprinting during Mesozoic events such as the Group-2 kimberlite magma eruptions across the Kaapvaal craton.

The mid-lithospheric mantle focal point of Group-2 kimberlite and MARID-style metasomatism has also been observed in other xenolith suites from across the Kaapvaal craton. In a study of kimberlite-borne eclogite xenoliths from Jagersfontein, Roberts Victor and Kimberley on the southwestern Kaapvaal craton, Burness et al. (2020) found that strongly LREE-enriched eclogites were derived from ~140 km depth, whereas much more depleted eclogites occur towards the base of the cratonic lithosphere down to 220 km depth. Similarly, eclogites from the Orapa kimberlite also show enrichment at mid-lithospheric levels (Aulbach et al., 2020), and thus it is feasible that this relatively shallow-level enrichment is a widespread feature of the Kaapvaal lithospheric mantle. We also note that lower crustal xenoliths from the Kaapvaal craton, which generally reside at <50 km depth (Schmitz and Bowring, 2003; Pearson et al., 1995), show REE patterns that are very similar to those of the reconstructed Palmitefontein eclogite xenoliths, with strong LREE-enrichments (N-MORB-normalized La/Sm of up to 6) and positive Eu anomalies (Fig. 8a-i). The Kaapvaal lower crustal xenoliths have ^{206}Pb/^{204}Pb ratios between 15.9 and 17.6 overlapping those of the Palmietfontein eclogites as determined in this study for fresh clinopyroxene crystals (Fig. 13). Akin to Kaapvaal eclogite suites with Archean formation ages, mafic lower crustal xenoliths from the region also reveal ages between ca. 3.1–2.6 Ga based on on their whole-rock Pb-Pb and zircon U-Pb systematics (Huang et al., 1995; Schmitz and Bowring, 2000). This may indicate mafic protolith formation in the Archean either related to ca. 2.7 Ga basaltic magmatism of the Ventersdorp Supergroup with significant 'underplating' (Schmitz and Bowring, 2000), or, similar to the Kaapvaal eclogites linked to subduction of oceanic crust during ca. 2.9 Ga continent amalgamation (Schmitz et al., 2004; Shirey and Harris, 2004). The U-Pb isotope systematics of Kaapvaal lower crustal xenoliths also record post-Archean resetting and thermal overprinting, related to Proterozoic orogenesis and Mesozoic continental rifting during Gondwana breakup (Schmitz and Bowring, 2000, 2003). Therefore, it is reasonable to assume that the Palmietfongein eclogite xenoliths have a similar origin to other Kaapvaal craton eclogites and the mafic lower crust, with protolith formation during subduction of Archean oceanic crust during continent amalgamation (ShirShirey and Harris, 2004). Most importantly, however, we recognize a craton-scale pattern in which eclogite components residing at mid-lithospheric depths tend to be more strongly chemically overprinted than deeper-seated eclogites, which supports the idea that seismic discontinuities within the cratonic mantle lithosphere reflect depth-controlled metasomatism caused by the ponding of volatile-rich low-volume melts and subsequent melt-rock interactions. Such localized metasomatic activity at mid-lithospheric depth, possibly related to amphibole stability or the position of the prominent ledge on the CO_2-bearing peridotite solidus, may be further elucidated from other suites of eclogite xenoliths worldwide (e.g. Aulbach et al., 2020), or by rapidly improving geophysical detection methods (e.g. Garber, 2018). Future work needs to assess how significant the metasomatic mid-lithosphere is in terms of volatile budgets and cycling, as well as its impact on craton stability and the formation of superlative metal deposits commonly associated with the ancient continental cores.

7. Conclusions

- Seventeen eclogite xenoliths were studied from the Group-1 75 Ma Palmietfontein kimberlite, located in the central area of the Kaapvaal craton, at the western margin of the Paleoproterozoic Bushveld large igneous province, where few previous studies of the lithospheric mantle exist. A mantle zircon recovered from the kimberlite heavy mineral concentrate provided U-Pb age dates of ca. 75 Ma, which can be taken as the timing of Palmietfontein Group-1 kimberlite magmatism.

- The Palmietfontein eclogites have features typical of eclogite xenoliths with oceanic crustal protoliths, including bulk REE patterns with positive Eu anomalies and flat HREEs, with garnet $\delta^{18}O$ values from 5.5–6.9‰

- The Palmietfontein eclogites contain equilibrium amphibole and have unusually low equilibration pressures between 2.7 and 4.5 GPa (mean 3.3 GPa), translating to shallow lithospheric mantle residence depths between 90 and 150 km. This depth range coincides with a mid-lithospheric discontinuity detected seismically within the Kaapvaal lithospheric mantle.

- The eclogites record relatively low $\Delta logfO_2$ values from FMQ-4.5 to FMQ-1.6 that do not correlate with incompatible element contents, ruling out oxidative metasomatism. Instead, eclogite fO_2 correlates with bulk MgO and Sr contents and records igneous protolith differentiation.

- In addition to the shallow mantle residence, the Palmietfontein eclogites bear ubiquitous diopside-rich clinopyroxene overgrowths, strong incompatible element enrichments and Pb isotope compositions that overlap directly with ~120 Ma Group-2 kimberlites and the metasomatic MARID xenoliths. Therefore, the residence of the Palmietfontein eclogites within the Kaapvaal mid-lithospheric discontinuity rendered them susceptible to intensive metasomatic overprinting associated with Cretaceous LIP kimberlite (Group-2 orangeite) magmatic events that impacted the Kaapvaal craton

Declaration of Competing Interest

The authors declare that they have no known competing financial interests or personal relationships that could have appeared to influence the work reported in this paper.

Acknowledgements

Appendix A

Table A1
Amphibole and secondary clinopyroxene mineral chemistry from the Palmietfontein eclogite xenoliths.

	Palm-10	Palm-12	Palm-18	Palm-6	Palm-8	Palm-10	Palm-13	Palm-14
	amph	*amph*	*amph*	*2nd cpx*	*2nd cpx*	*2nd cpx*	*2nd cpx*	*2nd cpx*
SiO_2	48.1	49.0	46.4	53.6	52.6	53.4	51.3	52.5
TiO_2	x	1.05	1	0.28	0.33	0.15	0.36	0.51
Al_2O_3	11.7	11.2	12.2	5.4	5.9	3.5	9.7	4.6
Cr_2O_3	0.18	0.16	0.24	0.13	0.14	0.32	0.10	0.09
FeO	5.91	4.94	5.59	3.9	3.5	4.7	5.0	4.3
MnO	0	0	0.02	0.04	0.02	0.12	0.06	0.06
MgO	17.4	17.9	17.8	14.7	14.5	15.1	11.9	15.3
CaO	10.7	9.8	8.7	19.4	20.0	21.2	18.4	20.8
Na_2O	3.8	4.6	4.3	2.2	2.1	1.2	2.9	1.3
K_2O	0.82	0.77	0.76	–		–	–	–
Total	99.1	98.4	97.0	99.7	99.1	99.7	99.6	99.5
Mg#	0.85	0.88	0.88	0.87	0.88	0.85	0.81	0.86
Jd	–	–	–	0.14	0.13	0.07	0.18	0.06
V	17.8	16.0	15.8					
Ni	40.6	23.3	23.8					
Sc	0.83	0.70	0.70					
Rb	0.32	0.27	0.26					
Ba	15.8	65.8	57.6					
Th	0.01	0.04	0.05					
U	0.003	0.004	0.01					
Nb	0.43	0.05	0.05					
Ta	0.01	0.003	0.002					
La	0.48	1.0	1.0					
Ce	1.0	2.0	2.0					
Pr	0.12	0.21	0.21					
Pb	0.31	0.19	0.19					
Sr	23.1	25.8	26.2					
Nd	0.51	0.86	0.87					
Sm	0.09	0.19	0.19					
Zr	0.4	3.5	4.1					

Table A1 (*continued*)

	Palm-10	Palm-12	Palm-18	Palm-6	Palm-8	Palm-10	Palm-13	Palm-14
Hf	0.01	0.11	0.11					
Eu	0.03	0.05	0.05					
Ti	3177	6295	5995					
Gd	0.07	0.15	0.15					
Tb	0.01	0.02	0.02					
Dy	0.03	0.08	0.08					
Y	0.10	0.23	0.23					
Ho	0.004	0.01	0.01					
Er	0.007	0.017	0.018					
Tm	0.001	0.002	0.002					
Yb	0.003	0.007	0.007					
Lu	0.0003	0.001	0.001					

Table A2

One-sigma standard deviations for mineral trace element compositions reported in Table 2 and Standards results.

	Palm-2	Palm-6	Palm-7	Palm-8	Palm-10	Palm-12	Palm-13	Palm-14	Palm-15	Palm-16	Palm-17	Palm-18	Palm-20	Palm-22	Palm-23	Palm-24	Palm-28		BCR Average	2	NIST 612 average	2
	Grt	Grt	Grt	Grt	Grt	Grt	Grt	Grt	Grt	Grt	Grt	Grt	Grt	Grt	Grt	Grt	Grt					
V	4.8	4.6	13.4	1.7	2.4	4.5	3.6	9.0	7.2	5.2	4.3	5.5	4.2	5.4	5.2	14.0	5.3	V	424	13	39.2	1.0
Ni	2.3	3.0	1.2	2.3	1.9	1.7	1.2	1.7	2.5	2.9	5.3	2.8	2.4	3.6	0.8	1.1	3.7	Ni	12.3	1.5	38.5	2.6
Sc	6.3	5.1	4.3	1.7	2.3	4.1	2.8	8.6	4.6	7.2	5.4	4.9	5.5	7.1	3.4	7.2	4.0	Sc	33.7	1.1	41.1	1.3
Rb	0.04	0.04	0.04	0.02	0.02	0.04	0.02	0.03	0.03	0.04	0.04	0.03	0.03	0.03	0.08	0.09	0.03	Rb	47	1.4	31.6	0.9
Ba	0.05	0.05	bd	0.01	0.02	0.05	0.04	0.04	0.05	0.21	0.07	0.04	0.04	0.07	0.34	0.10	0.18	Ba	633	20	37.8	1.1
Th	0.004	0.01	0.004	0.002	0.002	0.01	0.002	0.004	0.004	0.01	0.01	0.01	0.01	0.01	0.01	0.01	0.01	Th	5.6	0.2	37.2	0.5
U	0.01	0.01	0.003	0.004	0.01	0.01	0.004	0.02	0.01	0.01	0.01	0.01	0.01	0.01	0.05	0.02	0.01	U	1.6	0.10	37.2	0.6
Nb	0.02	0.02	0.01	0.003	0.01	0.01	0.01	0.02	0.02	0.02	0.02	0.01	0.30	0.01	0.02	0.02	0.01	Nb	11	0.40	38.1	0.8
Ta	0.003	0.004	0.002	0.001	0.001	0.003	0.002	0.003	0.002	0.003	0.003	0.002	0.01	0.002	0.003	0.003	0.003	Ta	0.7	0.10	39.8	0.6
La	0.01	0.01	0.005	0.003	0.004	0.01	0.003	0.01	0.01	0.01	0.01	0.01	0.01	0.01	0.01	0.01	0.01	La	24	0.5	35.8	0.7
Ce	0.03	0.03	0.01	0.01	0.01	0.03	0.01	0.04	0.02	0.04	0.02	0.03	0.03	0.04	0.06	0.04	0.03	Ce	51	1.1	38.3	0.6
Pr	0.01	0.02	0.01	0.005	0.01	0.01	0.01	0.02	0.01	0.01	0.01	0.02	0.02	0.02	0.01	0.03	0.01	Pr	6.3	0.2	37.2	0.4
Pb	0.01	0.01	0.02	0.01	0.01	0.01	0.01	0.02	0.01	0.44	0.01	0.01	0.02	0.01	0.66	0.02	0.03	Pb	11	0.4	39.0	0.9
Sr	0.06	0.06	0.05	0.02	0.02	0.05	0.03	0.12	0.06	0.06	0.04	0.07	0.05	0.08	0.06	0.09	0.13	Sr	322	10	76.1	1.5
Nd	0.12	0.16	0.19	0.03	0.05	0.11	0.05	0.25	0.09	0.11	0.08	0.14	0.11	0.16	0.12	0.29	0.11	Nd	27	1.1	35.3	1.1
Sm	0.12	0.16	0.37	0.04	0.06	0.17	0.06	0.23	0.09	0.10	0.14	0.15	0.13	0.14	0.31	0.12	Sm		6.2	0.50	36.7	1.0
Zr	0.19	0.38	0.44	0.21	0.08	1.06	0.13	0.81	0.43	0.21	0.37	0.28	0.25	0.39	0.34	0.49	0.62	Zr	164	5	36.0	0.9
Hf	0.02	0.03	0.04	0.01	0.01	0.04	0.01	0.03	0.02	0.02	0.02	0.02	0.01	0.02	0.01	0.02	0.03	Hf	4.4	0.30	34.8	0.6
Eu	0.05	0.07	0.15	0.02	0.02	0.06	0.02	0.09	0.05	0.05	0.05	0.06	0.06	0.07	0.05	0.12	0.06	Eu	1.8	0.10	34.4	0.7
Ti	47.5	43.3	73.1	35.7	32.9	42.5	33.3	91.8	35.5	53.9	54.6	59.4	81.4	71.1	60.8	68.2	56.3	Ti	15,395	971	48.2	3.4
Gd	0.18	0.21	0.56	0.12	0.10	0.29	0.10	0.35	0.17	0.16	0.20	0.22	0.21	0.19	0.24	0.43	0.22	Gd	6.3	0.4	36.9	0.6
Tb	0.03	0.04	0.09	0.02	0.02	0.06	0.02	0.07	0.03	0.03	0.03	0.04	0.04	0.03	0.04	0.08	0.04	Tb	0.9	0.1	35.9	0.3
Dy	0.22	0.23	0.61	0.18	0.15	0.51	0.15	0.60	0.24	0.24	0.19	0.22	0.34	0.23	0.39	0.6	0.26	Dy	6.1	0.4	36.0	0.6
Y	1.1	0.98	3.0	0.81	0.67	2.9	0.79	4.1	1.2	1.1	0.74	0.88	2.0	0.95	2.1	3.6	1.1	Y	32	0.8	38.2	0.9
Ho	0.06	0.05	0.13	0.04	0.03	0.13	0.04	0.14	0.06	0.05	0.04	0.05	0.09	0.05	0.09	0.14	0.06	Ho	1.2	0.1	37.9	0.6
Er	0.16	0.15	0.35	0.14	0.11	0.40	0.12	0.49	0.21	0.18	0.12	0.15	0.31	0.15	0.34	0.45	0.17	Er	3.4	0.1	37.4	0.6
Tm	0.03	0.03	0.06	0.03	0.02	0.07	0.02	0.09	0.04	0.04	0.02	0.03	0.06	0.03	0.06	0.09	0.03	Tm	0.50	0.05	37.6	0.6
Yb	0.21	0.19	0.36	0.15	0.12	0.48	0.17	0.65	0.28	0.22	0.15	0.19	0.41	0.18	0.39	0.6	0.2	Yb	3.3	0.30	40.0	0.8
Lu	0.04	0.03	0.05	0.02	0.02	0.07	0.03	0.09	0.05	0.04	0.03	0.03	0.07	0.03	0.07	0.09	0.03	Lu	0.5	0.05	37.7	0.3

	Cpx	Cpx	Cpx	Cpx	Cpx	Cpx	Cpx	Cpx	Cpx	Cpx	Cpx	Cpx	Cpx	Cpx	Cpx	Cpx	Cpx
V	34.5	36.8	33.0	17.1	18.7	33.6	48.6	77.5	69.5	40.2	35.1	33.8	44.5	19.9	40.2	97.8	29.9
Ni	40.5	47.1	28.9	47.2	42.4	22.0	43.1	23.9	41.3	54.7	90.5	47.5	41.6	32.0	14.3	15.5	64.9
Sc	2.4	2.1	2.5	0.84	1.3	2.5	2.8	2.9	2.2	2.7	1.9	1.9	3.0	1.3	1.8	3.4	2.2
Rb	0.03	0.02	0.04	0.01	0.01	0.03	0.02	0.02	0.02	0.11	0.02	0.02	0.03	0.01	0.05	0.04	0.03
Ba	0.04	0.14	0.07	0.03	0.05	0.22	0.06	0.06	0.10	0.70	0.07	0.10	0.04	0.02	0.24	0.10	0.17
Th	0.02	0.04	0.002	0.03	0.02	0.07	0.04	0.01	0.02	0.02	0.02	0.04	0.03	0.01	0.01	0.02	0.07
U	0.02	0.01	0.00	0.01	0.01	0.02	0.02	0.01	0.01	0.02	0.01	0.02	0.01	0.01	0.01	0.02	0.02
Nb	0.09	0.02	0.01	0.01	0.01	0.01	0.02	0.08	0.01	0.09	0.01	0.03	0.02	0.01	0.03	0.05	0.02
Ta	0.01	0.002	0.001	0.001	0.002	0.004	0.002	0.01	0.002	0.01	0.003	0.003	0.001	0.002	0.01	0.004	0.001
La	0.28	0.46	0.01	0.31	0.27	1.24	0.73	0.11	0.38	0.30	0.16	0.56	0.62	0.16	0.19	0.28	1.1
Ce	0.75	1.44	0.02	0.75	0.61	2.50	1.62	0.29	0.96	0.70	0.30	1.3	1.5	0.36	0.73	0.89	2.5
Pr	0.12	0.22	0.01	0.09	0.09	0.28	0.20	0.06	0.12	0.11	0.05	0.15	0.21	0.05	0.15	0.16	0.28
Pb	0.14	0.17	0.05	0.11	0.17	0.21	0.23	0.14	0.19	0.31	0.10	0.18	0.20	0.09	0.33	0.13	0.14
Sr	18.5	32.5	5.6	17.4	14.6	34.9	36.2	27.6	25.4	19.0	10.9	32.1	28.9	12.8	12.2	24.5	36.7
Nd	0.64	1.3	0.08	0.32	0.37	1.5	1.4	0.47	0.53	0.56	0.28	0.70	1.0	0.30	0.72	1.1	1.4
Sm	0.18	0.28	0.07	0.09	0.11	0.40	0.28	0.14	0.14	0.15	0.14	0.19	0.25	0.07	0.17	0.29	0.30
Zr	0.57	1.0	1.2	0.82	0.26	5.6	1.3	1.2	1.3	0.53	1.3	0.86	1.0	0.36	0.91	1.4	2.8
Hf	0.04	0.06	0.16	0.05	0.02	0.21	0.07	0.09	0.09	0.05	0.08	0.05	0.07	0.03	0.05	0.07	0.12
Eu	0.05	0.08	0.03	0.03	0.03	0.10	0.07	0.04	0.04	0.04	0.04	0.05	0.07	0.02	0.04	0.07	0.09
Ti	290	329	178	362	208	252	371	619	241	368	307	319	218	238	405	392	265
Gd	0.12	0.15	0.09	0.09	0.09	0.31	0.17	0.11	0.10	0.10	0.10	0.14	0.17	0.04	0.12	0.19	0.20
Tb	0.01	0.02	0.02	0.01	0.01	0.04	0.02	0.01	0.01	0.01	0.01	0.01	0.02	0.00	0.01	0.02	0.02

Table A2 (*continued*)

	Cpx	Cpx	Cpx	Cpx	Cpx	Cpx	Cpx	Cpx	Cpx	Cpx	Cpx	Cpx	Cpx	Cpx	Cpx	Cpx	Cpx
Dy	0.06	0.06	0.09	0.05	0.04	0.17	0.08	0.07	0.06	0.05	0.04	0.06	0.09	0.02	0.06	0.09	0.09
Y	0.11	0.12	0.20	0.10	0.08	0.43	0.16	0.17	0.12	0.10	0.07	0.10	0.21	0.03	0.12	0.19	0.16
Ho	0.01	0.01	0.02	0.01	0.01	0.03	0.01	0.01	0.01	0.01	0.01	0.01	0.02	0.004	0.01	0.01	0.01
Er	0.02	0.02	0.04	0.02	0.02	0.06	0.03	0.03	0.03	0.02	0.01	0.02	0.04	0.01	0.02	0.03	0.03
Tm	0.003	0.004	0.01	0.003	0.003	0.01	0.005	0.01	0.004	0.004	0.002	0.003	0.01	0.001	0.003	0.01	0.01
Yb	0.02	0.02	0.03	0.02	0.01	0.04	0.02	0.03	0.02	0.03	0.01	0.01	0.03	0.01	0.02	0.03	0.02
Lu	0.003	0.002	0.01	0.002	0.001	0.01	0.003	0.01	0.004	0.002	0.002	0.003	0.005	0.001	0.002	0.005	0.003

Table A3

Pb isotope compositions of Palmietfontein eclogite clinopyroxene and NIST-614 standard results.

	$^{206}Pb/$ ^{204}Pb	2σ (mean)	$^{207}Pb/$ ^{204}Pb	2σ (mean)	$^{208}Pb/$ ^{204}Pb	2σ (mean)	$^{207}Pb/$ ^{206}Pb	2σ (mean)	$^{208}Pb/$ ^{206}Pb	2σ (mean)	Total 208v	$^{206}Pb/$ ^{207}Pb	2σ (mean)
P15-1	17.793	0.041	15.530	0.036	38.216	0.091	0.873	0.001	2.103	0.002	0.008	1.1456	0.0008
P15-2	17.957	0.040	15.786	0.036	38.312	0.087	0.879	0.001	2.140	0.001	0.008	1.1372	0.0007
P15-3	17.266	0.068	15.599	0.061	37.743	0.171	0.905	0.001	2.214	0.004	0.008	1.1055	0.0009
P15-4	17.369	0.070	15.573	0.063	37.629	0.173	0.898	0.001	2.208	0.003	0.008	1.1138	0.0012
P15-5	17.197	0.067	15.416	0.057	37.395	0.168	0.896	0.001	2.196	0.003	0.007	1.1155	0.0011
average	*17.517*	*0.057*	*15.581*	*0.051*	*37.859*	*0.138*	*0.890*	*0.001*	*2.172*	*0.002*	*0.008*	*1.124*	*0.001*
P8-1	17.434	0.062	15.418	0.051	38.636	0.147	0.884	0.001	2.159	0.003	0.008	1.1307	0.0010
P8-2	18.443	0.110	16.040	0.092	39.401	0.263	0.874	0.001	2.146	0.007	0.007	1.1439	0.0015
P8-3	17.958	0.091	15.773	0.082	39.041	0.221	0.879	0.001	2.172	0.003	0.007	1.1373	0.0012
P8-4	18.068	0.123	15.762	0.100	38.828	0.260	0.874	0.001	2.149	0.003	0.007	1.1446	0.0016
P8-5	18.035	0.089	15.859	0.078	38.968	0.204	0.879	0.001	2.160	0.003	0.007	1.1372	0.0011
average	*17.988*	*0.095*	*15.771*	*0.080*	*38.975*	*0.219*	*0.878*	*0.001*	*2.157*	*0.004*	*0.007*	*1.139*	*0.001*
P10-1	17.917	0.056	15.598	0.048	39.074	0.130	0.870	0.001	2.181	0.002	0.011	1.1495	0.0009
P10-2	17.861	0.052	15.565	0.044	38.833	0.143	0.872	0.001	2.175	0.004	0.012	1.1471	0.0008
P10-3	17.851	0.055	15.565	0.046	38.932	0.138	0.871	0.001	2.182	0.002	0.012	1.1477	0.0007
P10-4	17.789	0.055	15.475	0.045	38.604	0.153	0.870	0.001	2.174	0.003	0.012	1.1498	0.0009
P10-5	17.880	0.051	15.570	0.045	38.933	0.125	0.871	0.001	2.178	0.002	0.012	1.1481	0.0009
average	*17.860*	*0.054*	*15.555*	*0.045*	*38.875*	*0.138*	*0.871*	*0.001*	*2.178*	*0.002*	*0.012*	*1.148*	*0.001*
P22-1	17.747	0.115	15.996	0.101	38.394	0.257	0.901	0.001	2.164	0.003	0.004	1.1097	0.0013
P22-2	17.469	0.137	15.746	0.124	37.437	0.304	0.902	0.001	2.148	0.003	0.004	1.1082	0.0014
P22-3	17.463	0.108	15.603	0.097	37.214	0.247	0.894	0.001	2.135	0.003	0.004	1.1188	0.0014
P22-4	17.294	0.106	15.587	0.096	37.224	0.243	0.901	0.001	2.152	0.003	0.004	1.1103	0.0012
P22-5	17.592	0.113	15.618	0.100	37.493	0.251	0.888	0.001	2.134	0.003	0.004	1.1263	0.0014
average	*17.513*	*0.116*	*15.710*	*0.104*	*37.552*	*0.261*	*0.897*	*0.001*	*2.147*	*0.003*	*0.004*	*1.115*	*0.001*
P12-1	19.314	0.112	15.805	0.088	38.879	0.233	0.817	0.001	2.013	0.002	0.005	1.2241	0.0012
P12-2	19.084	0.093	15.623	0.075	38.130	0.201	0.819	0.001	2.002	0.003	0.006	1.2215	0.0012
P12-3	19.183	0.102	15.653	0.080	38.426	0.213	0.816	0.001	2.005	0.003	0.006	1.2257	0.0011
P12-4	19.261	0.097	15.809	0.076	39.033	0.214	0.821	0.001	2.028	0.003	0.006	1.2179	0.0013
P12-5	19.149	0.102	15.771	0.081	38.796	0.223	0.823	0.001	2.027	0.003	0.005	1.2144	0.0014
average	*19.198*	*0.101*	*15.732*	*0.080*	*38.653*	*0.217*	*0.819*	*0.001*	*2.015*	*0.003*	*0.006*	*1.221*	*0.001*
P20-1	17.534	0.076	15.624	0.069	37.934	0.180	0.891	0.001	2.164	0.003	0.006	1.1224	0.0011
P20-2	17.243	0.077	15.465	0.066	37.589	0.165	0.897	0.001	2.180	0.002	0.007	1.1145	0.0011
P20-3	17.433	0.070	15.607	0.062	38.020	0.156	0.896	0.001	2.182	0.002	0.007	1.1165	0.0012
P20-4	17.312	0.075	15.415	0.066	37.551	0.168	0.890	0.001	2.169	0.003	0.006	1.1238	0.0011
P20-5	17.195	0.064	15.477	0.058	37.363	0.155	0.899	0.001	2.175	0.003	0.007	1.1120	0.0010
average	*17.343*	*0.072*	*15.518*	*0.064*	*37.692*	*0.165*	*0.895*	*0.001*	*2.174*	*0.003*	*0.007*	*1.118*	*0.001*
P13-1	17.702	0.095	15.650	0.083	38.076	0.211	0.884	0.001	2.153	0.003	0.005	1.1308	0.0012
P13-2	17.451	0.099	15.518	0.088	37.922	0.209	0.889	0.001	2.170	0.003	0.006	1.1253	0.0014
P13-3	17.594	0.085	15.481	0.074	37.991	0.185	0.880	0.001	2.161	0.002	0.007	1.1361	0.0011
P13-4	17.505	0.079	15.531	0.067	37.995	0.177	0.888	0.001	2.174	0.003	0.007	1.1265	0.0012
P13-5	17.611	0.067	15.510	0.057	38.041	0.145	0.880	0.001	2.161	0.002	0.007	1.1366	0.0011
average	*17.573*	*0.085*	*15.538*	*0.074*	*38.005*	*0.185*	*0.884*	*0.001*	*2.164*	*0.003*	*0.006*	*1.131*	*0.001*
P2-1	17.904	0.052	15.684	0.039	37.692	0.085	0.879	0.001	2.115	0.002	0.003	1.1382	0.0008
P2-2	17.337	0.049	15.710	0.040	37.488	0.085	0.906	0.001	2.157	0.001	0.003	1.1040	0.0006
P2-3	17.489	0.046	15.736	0.036	37.714	0.078	0.900	0.000	2.157	0.001	0.004	1.1115	0.0006
P2-4	17.630	0.051	15.616	0.039	37.537	0.087	0.885	0.001	2.128	0.001	0.003	1.1296	0.0007
P2-5	17.013	0.057	15.432	0.044	36.713	0.095	0.908	0.001	2.156	0.001	0.003	1.1013	0.0008
average	*17.474*	*0.051*	*15.636*	*0.040*	*37.429*	*0.086*	*0.895*	*0.001*	*2.143*	*0.001*	*0.003*	*1.117*	*0.001*
P6-1	17.637	0.094	15.750	0.082	38.053	0.202	0.892	0.001	2.159	0.002	0.004	1.1207	0.0012
P6-2	17.407	0.112	15.570	0.099	37.641	0.237	0.894	0.001	2.164	0.002	0.004	1.1182	0.0013
P6-3	17.318	0.094	15.500	0.085	37.429	0.210	0.895	0.001	2.160	0.002	0.004	1.1175	0.0012
P6-4	17.412	0.103	15.428	0.088	37.316	0.222	0.887	0.001	2.148	0.003	0.004	1.1274	0.0013
P6-5	17.312	0.127	15.502	0.110	37.517	0.274	0.896	0.001	2.168	0.002	0.004	1.1161	0.0015
average	*17.417*	*0.106*	*15.550*	*0.093*	*37.591*	*0.229*	*0.893*	*0.001*	*2.160*	*0.002*	*0.004*	*1.120*	*0.001*
P24-1	17.971	0.160	15.794	0.134	37.664	0.325	0.880	0.001	2.104	0.004	0.003	1.1362	0.0019
P24-2	17.744	0.191	15.694	0.167	37.352	0.403	0.883	0.001	2.112	0.003	0.002	1.1326	0.0018
P24-3	17.791	0.154	15.568	0.138	36.989	0.329	0.875	0.001	2.086	0.004	0.002	1.1429	0.0016
P24-4	17.475	0.161	15.393	0.138	36.620	0.326	0.882	0.001	2.101	0.003	0.003	1.1342	0.0017
P24-5	17.564	0.214	15.468	0.182	37.001	0.434	0.883	0.002	2.112	0.005	0.002	1.1319	0.0031

Table A3 (*continued*)

	206Pb/204Pb	2σ (mean)	207Pb/204Pb	2σ (mean)	208Pb/204Pb	2σ (mean)	207Pb/206Pb	2σ (mean)	208Pb/206Pb	2σ (mean)	Total 208v	206Pb/207Pb	2σ (mean)
average	17.709	0.176	15.584	0.152	37.125	0.364	0.881	0.002	2.103	0.004	0.002	1.136	0.002
P28-1	17.227	0.126	15.564	0.112	37.044	0.273	0.905	0.002	2.156	0.004	0.003	1.105	0.002
P28-2	17.386	0.130	15.573	0.114	37.416	0.276	0.896	0.001	2.153	0.003	0.003	1.116	0.002
P28-3	17.699	0.120	15.569	0.093	37.774	0.251	0.879	0.002	2.133	0.005	0.004	1.138	0.002
P28-4	16.977	0.080	15.433	0.072	36.976	0.185	0.910	0.001	2.179	0.003	0.005	1.099	0.001
P28-5	17.111	0.117	15.411	0.102	36.891	0.251	0.900	0.002	2.152	0.003	0.003	1.111	0.002
average	17.280	0.115	15.510	0.099	37.220	0.247	0.898	0.001	2.155	0.004	0.004	1.114	0.002
P14-1	18.718	0.262	16.056	0.214	39.600	0.530	0.857	0.002	2.112	0.004	0.002	1.1673	0.0024
P14-2	18.436	0.226	15.714	0.181	38.581	0.456	0.856	0.002	2.101	0.004	0.002	1.1688	0.0023
P14-3	18.481	0.214	15.849	0.177	38.799	0.466	0.859	0.002	2.100	0.004	0.002	1.1641	0.0021
P14-4	18.445	0.198	15.860	0.167	38.725	0.433	0.860	0.001	2.099	0.004	0.002	1.1629	0.0018
P14-5	18.386	0.173	15.703	0.149	38.597	0.370	0.856	0.001	2.101	0.003	0.003	1.1685	0.0018
average	18.493	0.215	15.836	0.178	38.860	0.451	0.857	0.002	2.103	0.004	0.002	1.166	0.002
P17-1	18.614	0.233	16.706	0.205	39.542	0.501	0.899	0.001	2.132	0.003	0.002	1.1124	0.0018
P17-2	18.376	0.232	16.527	0.200	38.842	0.488	0.902	0.002	2.116	0.004	0.002	1.1085	0.0021
P17-3	18.656	0.253	16.738	0.229	39.299	0.537	0.897	0.002	2.108	0.003	0.002	1.1154	0.0020
P17-4	17.528	0.203	15.765	0.176	37.022	0.420	0.900	0.002	2.117	0.004	0.002	1.1115	0.0019
P17-5	17.501	0.189	15.603	0.164	36.799	0.397	0.893	0.001	2.104	0.004	0.002	1.1202	0.0019
average	18.135	0.222	16.268	0.195	38.301	0.469	0.898	0.002	2.115	0.003	0.002	1.114	0.002

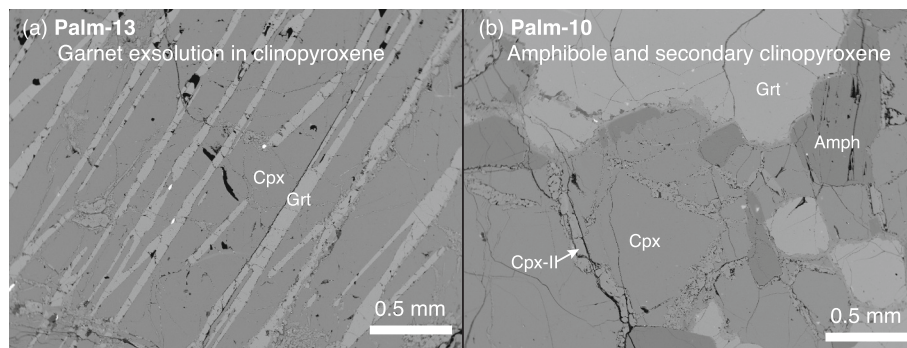| NIST-614 SRM	206Pb/204Pb	2σ(mean)	207Pb/204Pb	2σ(mean)	208Pb/204Pb	2σ(mean)	207Pb/206Pb	2σ(mean)	208Pb/206Pb	2σ(mean)
614–1	17.793	0.041	15.530	0.036	37.393	0.091	0.873	0.001	2.103	0.002
614–2	17.821	0.047	15.431	0.040	37.109	0.100	0.866	0.001	2.081	0.002
614–3	17.810	0.044	15.441	0.040	37.095	0.101	0.867	0.001	2.085	0.002
614–4	17.776	0.046	15.528	0.041	37.421	0.113	0.874	0.001	2.106	0.002
614–5	17.884	0.046	15.582	0.039	37.699	0.107	0.871	0.001	2.109	0.002
614–6	17.883	0.043	15.571	0.037	37.558	0.096	0.870	0.001	2.099	0.001
614–7	17.839	0.049	15.508	0.044	37.393	0.106	0.870	0.001	2.095	0.002
614–8	17.901	0.053	15.585	0.046	37.683	0.110	0.870	0.001	2.104	0.001
614–9	17.888	0.052	15.578	0.044	37.627	0.107	0.871	0.001	2.104	0.001
614–10	17.817	0.045	15.526	0.039	37.414	0.097	0.871	0.001	2.100	0.001
614–11	17.776	0.043	15.499	0.037	37.347	0.097	0.873	0.001	2.101	0.001
614–12	17.874	0.045	15.572	0.039	37.657	0.098	0.871	0.001	2.107	0.001
614–13	17.833	0.043	15.545	0.037	37.590	0.097	0.872	0.001	2.108	0.001
614–14	17.840	0.053	15.523	0.044	37.411	0.109	0.871	0.001	2.097	0.001
614–15	17.835	0.049	15.549	0.042	37.413	0.102	0.871	0.001	2.098	0.001
614–16	17.862	0.053	15.530	0.044	37.523	0.109	0.870	0.001	2.100	0.001
614–17	17.858	0.049	15.556	0.042	37.525	0.103	0.871	0.001	2.101	0.001
614–18	17.826	0.048	15.558	0.041	37.519	0.106	0.872	0.001	2.104	0.002
614–19	17.836	0.045	15.545	0.041	37.505	0.102	0.872	0.001	2.105	0.002
614–20	17.881	0.048	15.594	0.041	37.683	0.107	0.872	0.001	2.107	0.002
614–21	17.891	0.045	15.581	0.041	37.669	0.102	0.872	0.001	2.108	0.002
614–22	17.789	0.051	15.485	0.044	37.360	0.108	0.870	0.001	2.099	0.001
614–23	17.822	0.050	15.528	0.042	37.361	0.105	0.871	0.001	2.096	0.002
614–24	17.819	0.051	15.519	0.044	37.541	0.109	0.870	0.001	2.106	0.001
614–25	17.852	0.050	15.562	0.043	37.542	0.105	0.872	0.001	2.103	0.002
614–26	17.832	0.047	15.538	0.041	37.472	0.100	0.871	0.001	2.101	0.001
614–27	17.880	0.050	15.570	0.044	37.520	0.106	0.871	0.001	2.100	0.001
614–28	17.892	0.056	15.601	0.051	37.732	0.119	0.871	0.001	2.109	0.001
614–29	17.788	0.064	15.538	0.055	37.272	0.134	0.873	0.001	2.095	0.002
614–30	17.743	0.067	15.477	0.057	37.180	0.138	0.872	0.001	2.094	0.002
614–31	17.905	0.042	15.606	0.037	37.580	0.091	0.871	0.001	2.099	0.001
614–32	17.879	0.046	15.604	0.039	37.597	0.101	0.873	0.001	2.103	0.001
614–33	17.856	0.048	15.524	0.042	37.625	0.104	0.870	0.001	2.107	0.001
614–34	17.742	0.053	15.454	0.045	37.271	0.113	0.871	0.001	2.100	0.001
614–35	17.892	0.048	15.587	0.042	37.648	0.104	0.871	0.001	2.103	0.001
614–36	17.777	0.053	15.517	0.045	37.295	0.113	0.872	0.001	2.097	0.001
614–37	17.890	0.039	15.529	0.033	37.643	0.083	0.869	0.001	2.106	0.001
614–38	17.823	0.056	15.556	0.051	37.487	0.118	0.872	0.001	2.103	0.001
614–39	17.857	0.049	15.580	0.041	37.587	0.106	0.873	0.001	2.106	0.001
614–40	17.835	0.058	15.514	0.047	37.450	0.120	0.870	0.001	2.099	0.002
614–41	17.894	0.047	15.603	0.042	37.615	0.111	0.872	0.001	2.104	0.002
614–42	17.895	0.052	15.603	0.046	37.663	0.120	0.872	0.001	2.105	0.002
614–43	17.781	0.059	15.476	0.050	37.280	0.126	0.871	0.001	2.095	0.002
614–44	17.815	0.052	15.508	0.045	37.521	0.113	0.870	0.001	2.105	0.002
average	17.841		15.541		37.488		0.871		2.101	
2 sigma	0.088		0.089		0.319		0.003		0.011	
2 sigma RSD	0.495		0.572		0.851		0.343		0.542	

Fig. A1. Backscattered electron images for **(a) Palm-13** showing garnet (Grt) exsolution from clinopyroxene (Cpx), and **(b) Palm-10** showing the occurrence of secondary clinopyroxene ("Cpx-II") and amphibole (Amph).
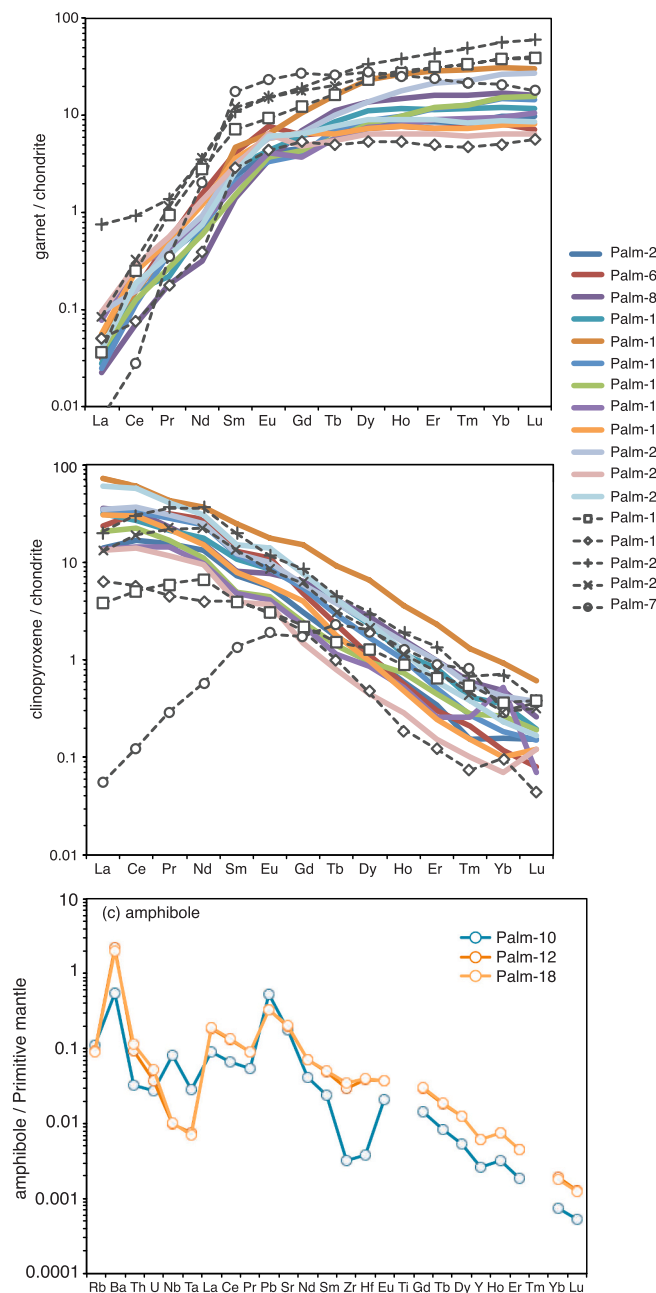

Fig. A2. Chondrite-normalized REE plots for **(a) garnet** and **(b) clinopyroxene.** Primitive-mantle normalized multi-element plot for **(c) amphibole** from the Palmietfontein eclogites. Grey dashed lines in (a) and (b) indicate eclogites that belong to the "basaltic" eclogites that predominantly have "high-Ca" garnet compositions. Coloured lines indicate eclogites belonging to the "enriched" eclogites that have predominantly "high-Mg" garnets. Normalization values from Palme & O'Neill (2014).
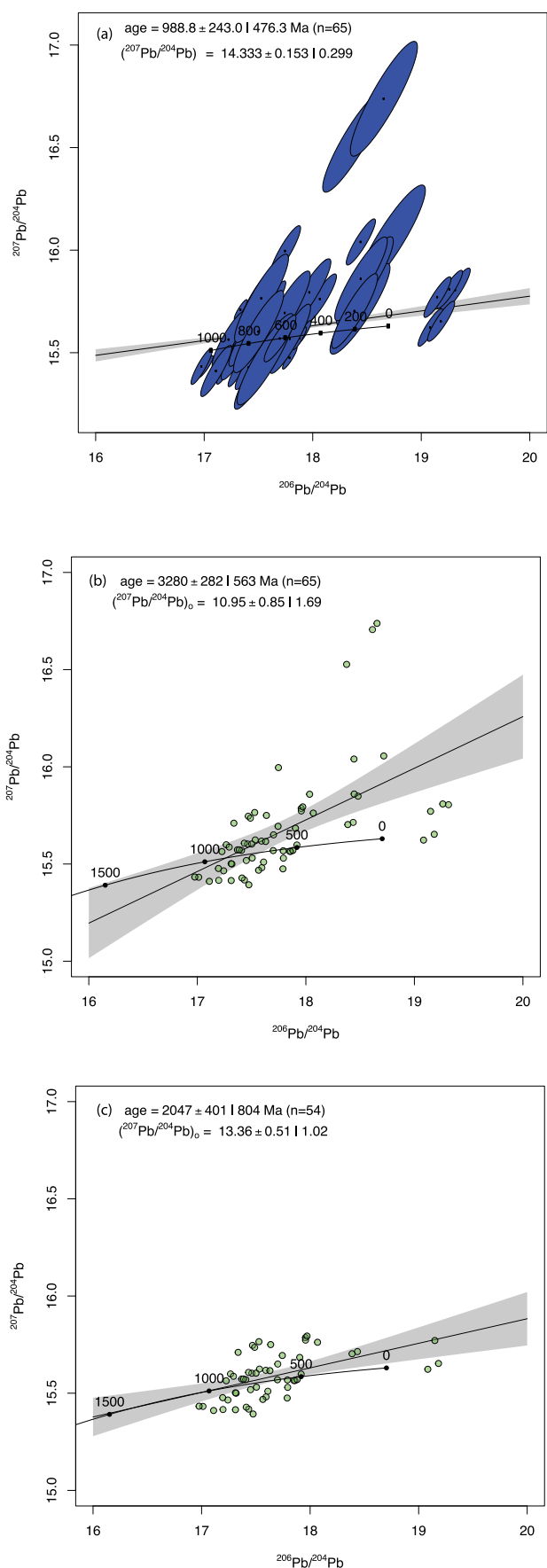
Fig. A3. Regression of Palmietfontein clinopyroxene Pb isotope data. **(a)** Model-1 regression of all clinopyroxene Pb isotope data using 2⌠uncertainties (90% confidence level) produces an isochron with an associated age of 989 ± 243 Ma. **(b)** Ordinary least-squares regression (Model-2) of all Pb isotope data yields an isochron with an associated age of 3280 ± 282 Ma that in **(c)** reduces to 2047 ± 401 Ma when 207Pb/204Pb ratios >15.8 are excluded. Regressions were performed using Isoplot R of Vermeesch (2018) with the Pb evolution line from Stacey and Kramers (1975) shown for comparison.
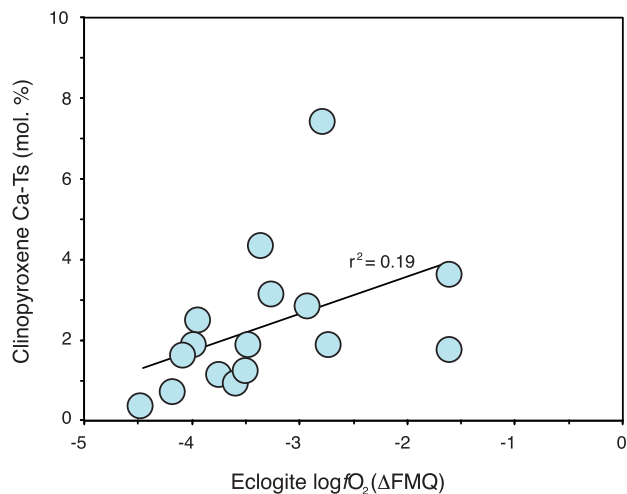
Fig. A4. Clinopyroxene Ca-Tschermak's component (Ca-Ts) and calculated eclogite oxygen fugacity relative to FMQ. Oxygen fugacity calculated using Stagno et al. (2015); see Table 5 and Fig. 6.

(caption on next column)
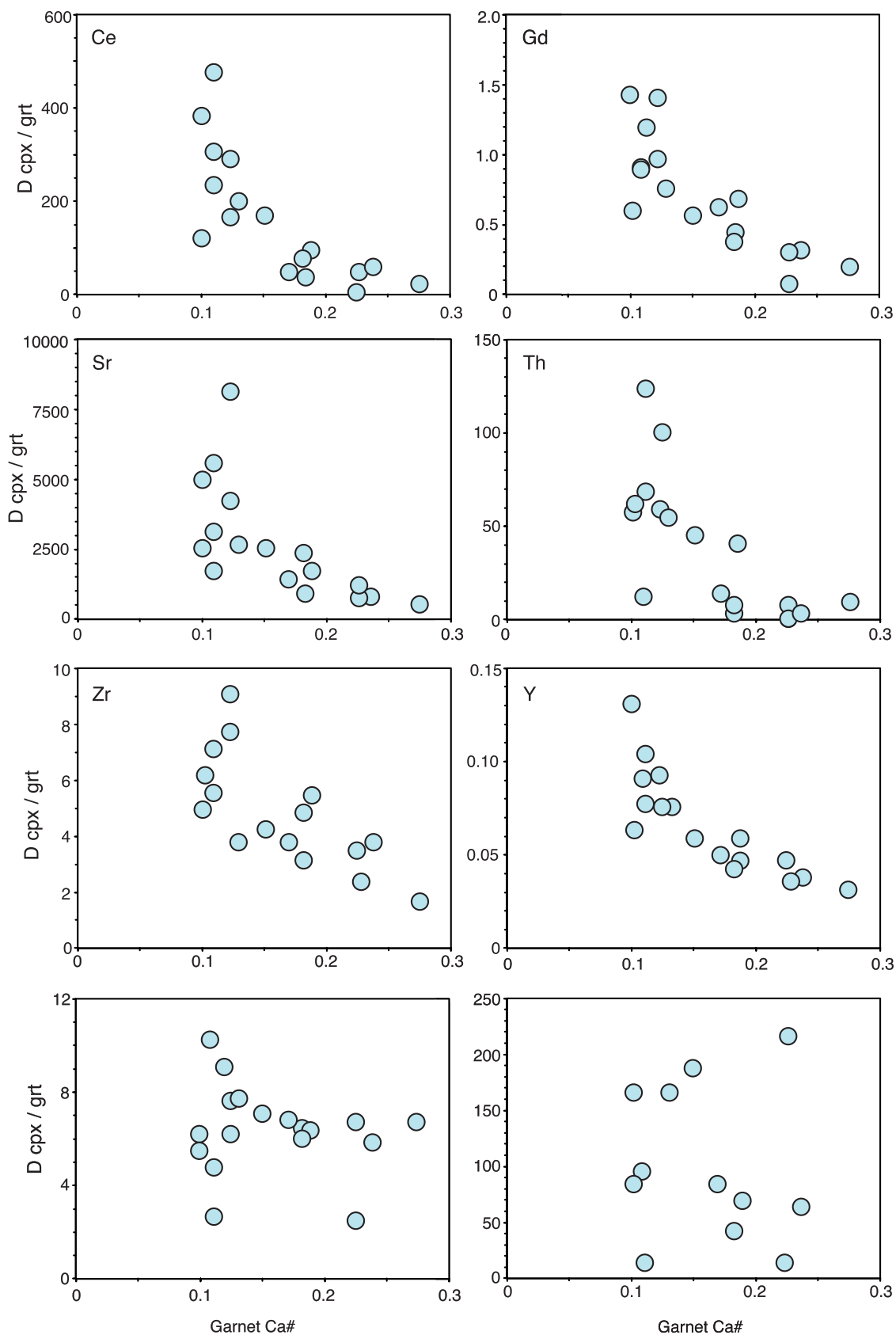
Fig. A5. Relationship between garnet Ca# (Table 2) and various trace elements. Exponential relationships can be observed between garnet Ca contents and Sr, the LREE-MREE (e.g. Ce, Gd), and some HFSE (Th, Zr and Y), but no relationships exist for elements such as Nb, Pb, Ti, and the HREE (not shown).

References

Adam, J., Green, T., 2006. Trace element partitioning between mica- and amphibole-bearing garnet lherzolite and hydrous basanitic melts. 1. Experimental results and the investigation of controls on partitioning behaviour. Contrib. Mineral. Petrol. 152, 1–17.

Aulbach, S., Jacob, D.E., 2016. Major- and trace-elements in cratonic mantle eclogites and pyroxenites reveal heterogeneous sources and metamorphic processing of low-pressure protoliths. Lithos 262, 586–605.

Aulbach, S., Viljoen, K.S., 2015. Eclogite xenoliths from the Lace kimberlite, Kaapvaal craton: From convecting mantle source to palaeo-ocean floor and back. Earth Planet. Sci. Lett. 431, 274–286.

Aulbach, S., Gerdes, A., Viljoen, K.S., 2016. Formation of diamondiferous kyanite–eclogite in a subduction mélange. Geochim. Cosmochim. Acta 179, 156–176.

Aulbach, S., Massuyeau, M., Gaillard, F., 2017a. Origins of cratonic mantle discontinuities: A view from petrology, geochemistry and thermodynamic models. Lithos 268-271, 364–382.

Aulbach, S., Jacob, D.E., Cartigny, P., Stern, R.A., Simonetti, S.S., Wörner, G., Viljoen, K. S., 2017b. Eclogite xenoliths from Orapa: Ocean crust recycling, mantle metasomatism and carbon cycling at the western Zimbabwe craton margin. Geochim. Cosmochim. Acta 213, 574–592.

Aulbach, S., Woodland, A.B., Vasilyev, P., Galvez, M.E., Viljoen, K.S., 2017c. Effects of low-pressure igneous processes and subduction on $Fe^{3+}/\Sigma Fe$ and redox state of mantle eclogites from Lace (Kaapvaal craton). Earth Planet. Sci. Lett. 474, 283–295.

Aulbach, S., Heaman, L.M., Jacob, D.E., Viljoen, K.S., 2019. Ages and sources of mantle eclogites: ID-TIMS and in situ MC-ICPMS Pb-Sr isotope systematics of clinopyroxene. Chem. Geol. 503, 15–28.

Aulbach, S., Massuyeau, M., Garber, J.M., Gerdes, A., Heaman, L.M., Viljoen, K.S., 2020. Ultramafic carbonated melt- and auto-metasomatism in mantle eclogites: compositional effects and geophysical consequences. Geochem. Geophys. Geosystems 5 e2019GC008774.

Aulbach, S., Viljoen, K.S., Gerdes, A., 2020b. Diamondiferous and barren eclogites and pyroxenites from the western Kaapvaal craton record subduction and mantle metasomatism, respectively. Lithos 368-369, 105588.

Bach, W., Alt, J.C., Niu, Y., Humphris, S.E., Erzinger, J., Dick, H., 2001. The geochemical consequences of late-stage low-grade alteration of lower ocean crust at the SW Indian Ridge: Results from ODP Hole 735B (Leg 176). Geochim. Cosmochim. Acta 65, 3267–3287.

Baker, J., Peate, D., Waight, T., Meyzen, C., 2004. Pb isotopic analysis of standards and samples using a Pb-Pb double spike and thallium to correct for mass bias with a double-focusing MC-ICP-MS. Chem. Geol. 211, 275–303.

Bang, Y., Hwang, H., Kim, T., Cynn, H., Park, Y., Jung, H., Park, C., Popov, D., Prakapenka, V.B., Wang, L., Liermann, H.-P., Irifune, T., Mao, H.-K., Lee, Y., 2021. The stability of subducted glaucophane with the Earth's secular cooling. Nat. Comms. 12, 1496.

Barth, M.G., Rudnick, R.L., Horn, I., McDonough, W.F., Spicuzza, M.J., Valley, J.W., Haggerty, S.E., 2001. Geochemistry of xenolithic eclogites from West Africa, Part I: a link between low MgO eclogites and Archean crust formation. Geochim. Cosmochim. Acta 65, 1499–1527.

Becker, M., le Roex, A.P., 2006. Geochemistry of South African On- and Off-craton, Group I and Group II Kimberlites: Petrogenesis and Source Region Evolution. J. Petrol. 47, 673–703.

Belousova, E.A., Griffin, W.L., Pearson, N.J., 1998. Trace element composition and cathodoluminescence properties of southern African kimberlitic zircons. Mineral. Mag. 62, 355–366.

Beyer, C., Frost, D.J., Miyajima, N., 2015. Experimental calibration of a garnet–clinopyroxene geobarometer for mantle eclogites. Contrib. Mineral. Petrol. 169, 18.

Black, L.P., Kamo, S.L., Allen, C.M., Davis, D.W., Aleinikoff, J.N., Valley, J.W., Mundil, R., Campbell, I.H., Korsch, R.J., Williams, I.S., Foudoulis, C., 2004. Improved (206)Pb/(238)U microprobe geochronology by the monitoring of a trace-element-related matrix effect: SHRIMP, ID-TIMS, ELA-ICP-MS and oxygen isotope documentation for a series of zircon standards. Chem. Geol. 205, 115–140.

Braunger, S., Marks, M.A.W., Wenzel, T., Chymz, L., Azzone, R.G., Markl, G., 2020. Do carbonatites and alkaline rocks reflect variable redox conditions in their upper mantle source? Earth Planet. Sci. Lett. 533, 116041.

Burness, S., Smart, K.A., Tappe, S., Stevens, G., Woodland, A.B., Cano, E., 2020. Sulphur-rich mantle metasomatism of Kaapvaal craton eclogites and its role in redox-controlled platinum group element mobility. Chem. Geol. 542, 119476.

Chen, W., Simonetti, A., 2015. Isotopic (Pb, Sr, Nd, C, O) evidence for plume-related sampling of an ancient, depleted mantle reservoir. Lithos 216-217, 81–92.

Creighton, S., Stachel, T., Matveev, S., Höfer, H., McCammon, C., Luth, R.W., 2009. Oxidation of the Kaapvaal lithospheric mantle driven by metasomatism. Contrib. Mineral. Petrol. 157, 491–504.

da Costa, A.J.M., 1989. Palmietfontein kimberlite pipe, South Africa–A case history. Geophysics 54, 689–700.

Dasgupta, R., Hirschmann, M.M., McDonough, W.F., Spiegelman, M., Withers, A.C., 2009. Trace element partitioning between garnet lherzolite and carbonatite at 6.6 and 8.6 GPa with applications to the geochemistry of the mantle and of mantle-derived melts. Chem. Geol. 262, 57–77.

Dawson, J.B., Smith, J.V., 1977. The MARID (mica-amphibole-rutile-ilmenite-diopside) suite of xenoliths in kimberlite. Geochim. Cosmochim. Acta 41, 309–323.

Day, H.W., 2012. A revised diamond-graphite transition curve. Am. Mineral. 97, 52–62.

El Atrassi, F., Chazot, G., Brunet, F., Chopin, C., Bouybaouene, M., 2014. Amphibole genesis in pyroxenites from the Beni Bousera peridotite massif (Rif, Morocco): Evidence for two different metasomatic episodes. Lithos 208-209, 67–80.

Elburg, M.A., Cawthorn, R.A., 2017. Source and evolution of the alkaline Pilanesberg Complex, South Africa. Chem. Geol. 455, 148–165.

Enami, M., Zang, Q., Yin, Y., 1995. High-pressure eclogites in northern Jiangsu – southern Shandong province, eastern China. J. Metamorphic Geol. 11, 589–603.

Fabriès, J., Lorand, J.-P., Guiraud, M., 2001. Petrogenesis of the amphibole-rich veins from the Lherz orogenic lherzoite massif (Eastern Pyrenees, France): a case study for the origin of orthopyroxene-bearing amphibole pyroxenites in the lithospheric mantle. Contrib. Mineral. Petrol. 140, 383–403.

Falloon, T.J., Green, D.H., 1998. Anhydrous partial melting of peridotite from 8 to 35 kb and the petrogenesis of MORB. J. Petrol. 379-414.

Fisher, K.A., Ford, H.A., Abt, D.L., Rychert, C.A., 2010. The Lithosphere-Asthenosphere Boundary. Annu. Rev. Earth Planet. Sci. 38, 551–575.

Fitzpayne, A., Giuliani, A., Phillips, D., Hergt, J., Woodhead, J.D., Farquhar, J., Fiorentini, M.L., Drysdale, R.N., Wu, N., 2018. Kimberlite-related metasomatism recorded in MARID and PIC mantle xenoliths. Mineral. Petrol. 112, 71–84.

Fitzpayne, A., Giuliani, A., Maas, R., Hergt, J., Janney, P., Phillips, D., 2019. Progressive metasomatism of the mantle by kimberlite melts: Sr–Nd–Hf–Pb isotope compositions of MARID and PIC minerals. Earth Planet. Sci. Lett. 509, 15–26.

Foley, S.F., Barth, M.G., Jenner, G.A., 2000. Rutile/melt partition coefficients for trace elements and an assessment of the influence of rutile on the trace element characteristics of subduction zone magmas. Geochem. Cosmochim. Acta 64, 933–938.

Foley, S., Tiepolo, M., Vannucci, R., 2002. Growth of early continental crust controlled by melting of amphibolite in subduction zones. Nature 417, 837–840.

Fraser, K.J., Hawkesworth, C.J., Erlank, A.J., Mitchell, R.H., Scott Smith, B.H., 1985. Sr, Nd and Pb isotope and minor element geochemistry of lamproites and kimberlites. Earth Planet. Sci. Lett. 76, 57–70.

Frost, D.J., McCammon, C.A., 2008. The redox state of Earth's mantle. Annu. Rev. Earth Planet. Sci. 36, 389–420.

Gale, A., Dalton, C.A., Langmuir, C.H., Su, Y.J., Schilling, J.G., 2013. The mean composition of ocean ridge basalts. Geochem. Geophys. Geosys. 14, 489–518.

Garber, J., Maurya, S., Hernandex, J.-A., Duncan, M.S., Zeng, L., Zhang, H.L., Faul, U., Mcammon, C., Montagner, J.-P., Moresi, L., Romanowicz, B.A., Rudnick, R.L., Stixrude, L., 2018. Multidisciplinary constraints on the abundance of diamond and eclogite in the cratonic lithosphere. Geochem. Geophys. Geosyst. 19 https://doi.org/10.1029/208GC007534.

Ghiroso, M.S., Hirschmann, M.M., Reiners, P.W., Kress III, V.C., 2002. The pMELTS: A revision of MELTS for improved calculation of phase relations and major element partitioning related to partial melting of the mantle to 3 GPa. Geochem. Geophys. Geosyst. 3, 1–36.

Giuliani, A., Phillips, D., Woodhead, J.D., Kamenetsky, V.S., Fiorentini, M.L., Maas, R., Soltys, A., Armstrong, R.A., 2015. Did diamond-bearing orangeites originate from MARID-veined peridotites in the lithospheric mantle? Nat. Commun. 6, 6837.

Gréau, Y., Huang, J.-X., Griffin, W.L., Renac, C., Alard, O., O'Reilly, S.Y., 2011. Type I eclogites from Roberts Victor kimberlites: products of extensive mantle metasomatism. Geochim. Cosmochim. Acta 75, 6927–6954.

Green, T.H., Blundy, J.D., Adam, J., Yaxley, G.M., 2000. SIMS determination of trace element partition coefficients between garnet, clinopyroxene and hydrous basaltic liquids at 2–7.5 GPa and 1080–1200°C. Lithos 53, 165–187.

Green, D.H., Hibberson, W.O., Rosenthal, A., Kovacs, I., Yaxley, G.M., Falloon, T.J., Brink, F., 2014. Experimental study of the influence of water on melting and phase assemblages in the upper mantle. J. Petrol. 55, 2067–2096.

Grégoire, M., Bell, D.R, Le Roex, A.P., 2002. Trace element geochemistry of phlogopite-rich mafic mantle xenoliths: their classification and their relationship to phlogopite-bearing peridotites and kimberlites revisited. Contrib. Mineral. Petrol. 142, 603–625.

Grégoire, M., Bell, D.R., Le Roex, A.P., 2003. Garnet lherzolites from the Kaapvaal Craton (South Africa): Trace element evidence for a metasomatic history. J. Petrol. 44, 629–657.

Grégoire, M., Tinguely, C., Bell, D.R., le Roex, A.P., 2005. Spinel lherzolite xenoliths from the Premier kimberlite (Kaapvaal craton, South Africa): Nature and evolution of the shallow upper mantle beneath the Bushveld complex. Lithos 84, 185–205.

Gregory, R.T., Taylor Jr., H.P., 1981. An oxygen isotope profile in a section of Cretaceous oceanic crust, Samail Ophiolite, Oman: Evidence for $\delta^{18}O$ buffering of the oceans by deep (>5 km) seawater-hydrothermal circulation at mid-ocean ridges. J. Geophys. Res. 86 (B4), 2737–2755.

Griffin, W.L., O'Reilly, S.Y., Natapov, L.M., Ryan, C.G., 2003. The evolution of lithospheric mantle beneath the Kalahari Craton and its margins. Lithos 71 (2–4), 215–241.

Griffin, W.L., Batumike, J.M., Greau, Y., Pearson, N.J., Shee, S.R., O'Reilly, S.Y., 2014. Emplacement ages and sources of kimberlites and related rocks in southern Africa: U-Pb ages and Sr-Nd isotopes of groundmass perovskite. Contrib. Mineral. Petrol. 168, 1–13.

Grütter, H.S., 2009. Pyroxene xenocryst geotherms: Techniques and application. Lithos 112, 1167–1178.

Halama, R., John, T., Herms, P., Hauff, F., Schenk, Y., 2011. A stable (Li, O) and radiogenic (Sr, Nd) isotope perspective on metasomatic processes in a subducting slab. Chem. Geol. 281, 151–166.

Hanger, B.J., Yaxley, G.M., Berry, A.J., Kamenetsky, V.S., 2015. Relationships between oxygen fugacity and metasomatism in the Kaapvaal subcratonic mantle, represented by garnet peridotite xenoliths in the Wesselton kimberlite, South Africa. Lithos 212, 443–452.

Harmer, R.E., 1999. The petrogenetic association of carbonatite and alkaline magmatism: constraints from the Spitskop complex, South Africa. J. Petrol. 40, 525–548.

Harris, C., Vogeli, J., 2010. Oxygen isotope composition of garnet in the Peninsula Granite, Cape Granite Suite, South Africa: Constraints on melting and emplacement mechanisms. South African J. Geol. 113, 401–412.

Harte, B., Kirkley, M.B., 1997. Partitioning of trace elements between clinopyroxene and garnet: data from mantle eclogites. Chem. Geol. 136, 1–24.

Hasterok, D., Chapman, D.S., 2011. Heat production and geotherms for the continental lithosphere. Earth Planet. Sci. Lett. 307, 59–70.

Hawkesworth, C.J., Cawood, P.A., Dhuime, B., Kemp, T.I.S., 2017. Earth's Continental Lithosphere Through Time. Annu. Rev. Earth Planet. Sci. 45, 169–198.

Herzberg, C., Condie, K., Korenaga, J., 2010. Thermal history of the Earth and its petrological expression. Earth Planet. Sci. Lett. 292, 79–88.

Hills, D.V., Haggerty, S.E., 1989. Petrochemistry of eclogites from the Koidu Kimberlite Complex, Sierra Leone. Contrib. Mineral. Petrol. 103, 397–422.

Howarth, G.H., Skinner, E.M.W., Prevec, S.A., 2011. Petrology of the hypabyssal kimberlite of the Kroonstad Group II kimberlite (orangeite) cluster, South Africa: Evolution of the magma within the cluster. Lithos 125, 795–808.

Huang, Y.-M., Van Calsteren, P., Hawkesworth, C.J., 1995. The evolution of the lithosphere in southern Africa: A perspective on the basic granulite xenoliths from kimberlites in South Africa. Geochim. Cosmochim. Acta 59, 4905–4920.

Huang, J.-X., Greau, Y., Griffin, W.L., O'Reilly, S.Y., Pearson, N.J., 2012. Multi-stage origin of Roberts Victor eclogites: Progressive metasomatism and its isotopic effects. Lithos 142-143, 161–181.

Ionov, D.A., Hoffman, A.W., 1995. Nb-Ta-rich mantle amphiboles and micas: Implications for subduction-related metasomatic trace element fractionations. Earth Planet. Sci. Lett. 131, 341–356.

Jackson, S.E., Pearson, N.J., Griffin, W.L., Belousova, E.A., 2004. The application of laser ablation-inductively coupled plasma-mass spectrometry to in situ U-Pb zircon geochronology. Chem. Geol. 211, 47–69.

Jacob, D., Jagoutz, E., Lowry, D., Mattey, D., Kudrjavtseva, G., 1994. Diamondiferous eclogites from Siberia: remnants of Archean oceanic crust. Geochimi. Cosmochim. Acta 58, 5191–5207.

Jacob, D.E., Viljoen, K.S., Grassineau, N.V., 2009. Eclogite xenoliths from Kimberley, South Africa—a case study of mantle metasomatism in eclogites. Lithos 112, 1002–1013.

James, D.E., Niu, F., Rokosky, J., 2003. Crustal structure of the Kaapvaal craton and its significance for early crustal evolution. Lithos 71, 413–429.

Jelsma, H.A., De Wit, M.J., Thiart, C., Dirks, P.H.G.M., Viola, G., Basson, I.J., Anckar, E., 2004. Preferential distribution along transcontinental corridors of kimberlites and related rocks of Southern Africa. South African J. Geol. 107, 301–324.

Jelsma, H., Barnett, W., Richards, S., Lister, G., 2009. Tectonic setting of kimberlites. Lithos 112, 155–165.

Jochum, K.P., Weis, U., Stoll, B., Kuzmin, D., Yang, Q., Raczek, I., Jacob, D.E., Stracke, A., Birbaum, K., Frick, D.A., Günther, D., Enzweiler, J., 2011. Determination of reference values for NIST SRM 610–617 glasses following ISO guidelines. Geostand. Geoanal. Res. 35, 397–429.

John, T., Gussone, N., Podladchikov, Y.Y., Bebout, G.E., Dohmen, R., Halama, R., Klemd, R., Magna, T., Seitz, H.M., 2012. Volcanic arcs fed by rapid pulsed fluid flow through subducting slabs. Nat. Geosci. 5 (7), 489–492.

Jourdan, F., Bertrand, H., Schärer, U., Blichert-Toft, J., Féraud, G., Kampunzu, A.B., 2007. Major and trace element and Sr, Nd, Hf, and Pb isotope compositions of the Karoo large igneous province, Botswana–Zimbabwe: Lithosphere vs. mantle plume contribution. J. Petrol. 48, 1043–1077.

Karato, S.-I., Park, J., 2018. On the origin of the upper mantle seismic discontinuities. In: Yuan, H., Romanowicz, B. (Eds.), Lithospheric Discontinuities. https://doi.org/10.1002/9781119249740.ch1.

Katayama, I., Suyama, Y., Ando, J., Komiya, T., 2009. Mineral chemistry and P–T condition of granular and sheared peridotite xenoliths from Kimberley, South Africa: Origin of the textural variation in the cratonic mantle. Lithos 109, 333–340.

Kimura, J.-I., Kawabata, H., 2014. Trace element mass balance in hydrous adiabatic mantle melting: The hydrous adiabatic mantle simulator version 1 (HAMMS1). Geochem. Geophys. Geosyst. 15, 2467–2493.

Klemme, S., Blundy, J.D., Wood, B.J., 2002. Experimental constraints on major and trace element partitioning during partial melting of eclogite. Geochim. Cosmochim. Acta 66, 3109–3123.

Kobussen, A.F., Griffin, W.L., O'Reilly, S.Y., 2012. Cretaceous thermo-chemical modification of the Kaapvaal cratonic lithosphere, South Africa. Lithos 112S, 886–895.

Konzett, J., Armstrong, R.A., Sweeney, R.J., Compston, W., 1998. The timing of MARID metasomatism in the Kaapvaal mantle: An ion probe study of zircons from MARID xenoliths. Earth Planet. Sci. Lett. 160, 133–145.

Korenaga, J., 2008. Urey ratio and the structure and evolution of Earth's mantle. Reviews of Geophysics 46, 2007RG000241.

Kramers, J.D., Roddick, J., Dawson, J.B., 1983. Trace element and isotope studies on veined, metasomatic and "MARID" xenoliths from Bultfontein. South Africa. Earth Planet. Sci. Lett. 65, 90–106.

Krogh, E.J., 1988. The garnet–clinopyroxene Fe–Mg geothermometer–a reinterpretation of existing experimental data. Contrib. Mineral. Petrol. 99, 44–48.

Krogh Ravna, E.J., 2000. The garnet-clinopyroxene Fe^{2+}-Mg geothermometer: an updated calibration. J. Metamorph. Geol. 18, 211–219.

Lazarov, M., Woodland, A.B., Brey, G.P., 2009. Thermal state and redox conditions of the Kaapvaal mantle: A study of xenoliths from the Finsch mine, South Africa. Lithos 112S, 913–925.

Lazarov, M., Brey, G.P., Weyer, S., 2012. Evolution of the South African mantle–a case study of garnet peridotites from the Finsch diamond mine (Kaapvaal craotn); Part 2: Multiple depletion and re-enrichment processes. Lithos 154, 210–223.

Leake, B.E., Woolley, A., Arps, C.E.S., Birch, W., Gilbert, C.M., Grice, J.D., Hawthorne, F.C., Kato, A., Kisch, H.J., Krivovichev, V.G., Linthout, K., Laird, J., Mandarino, J.A., Maresch, W.V., Nickel, E.H., Rock, N.M.S., Schumacher, J.C., Smith, D.C., Stephenson, N.C.N., Ungaretti, L., Whittaker, E.J.W., Youzhi, G., 1997. Nomenclature of amphiboles; Report of the Subcommittee on Amphiboles of the International Mineralogical Association, Commission on New Minerals and Mineral Names. Am. Mineral. 82, 1019–1037.

Locock, A.J., 2014. An Excel spreadsheet to classify chemical analyses of amphiboles following the IMA 2012 recommendations. Comput. Geosci. 62, 1–11.

Lowry, D., Mattey, D.P., Harris, J.W., 1999. Oxygen isotope composition of syngenetic inclusions in diamond from the Finsch Mine. RSA. Geochim. Cosmochim. Acta 63, 1825–1836.

Ludwig, K.R., 2000. Isoplot/Ex version 2.2. – a geochronological toolkit for Microsoft Excel. In: Berkeley Geochronology Center Special Publication No. 1a Berkeley, California.

MacGregor, I.D., Manton, W.I., 1986. Roberts Victor eclogites: ancient oceanic crust. J. Geophys. Res. Solid Earth 91, 14063–14079.

Massone, H.-J., 2012. Formation of amphibole and clinozoisite-epidote in eclogite owing to fluid infiltration during exhumation in a subduction channel. J. Petrol. 53, 1969–1998.

Mattey, D., Lowry, D., Macpherson, C., 1994. Oxygen isotope composition of mantle peridotite. Earth Planet. Sci. Lett. 128, 231–241.

Mikhail, S., McCubbin, F.M., Jenner, F.E., Shirey, S.B., Rumble, D., Bowden, R., 2019. Diamondites: evidence for a distinct tectono-thermal diamond-forming event beneath the Kaapvaal craton. Contrib. Mineral. Petrol. 174, 1–15.

Ngwenya, N.S., Tappe, S., 2020. Diamondiferous lamproites of the Luangwa Rift in Central Africa and links to remobilized cratonic lithosphere. Chem. Geol. 120019.

Niida, K., Green, D.H., 1999. Stability and chemical composition of pargasitic amphibole in MORB pyrolite under upper mantle conditions. Contrib. Mineral. Petrol. 135, 18–40.

Okay, A.I., 1995. Paragonite eclogites from Dabie Shan, China: re-equilibration during exhumation. J. Metamorphic Geol. 13, 449–460.

Orejana, D., Villaseca, C., Billström, K., Paterson, B.A., 2008. Petrogenesis of Permian alkaline lamprophyres and diabases from the Spanish Central System and their geodynamic context within western Europe. Contrib. Mineral. Petrol. 156, 477–500.

Palin, R.M., White, R.W., 2016. Emergence of blueschists on Earth linked to secular changes in oceanic crust composition. Nat. Geosci. 9, 60–64.

Palme, H., O'Neill, H.S.C., 2003. Cosmochemical estimates of mantle composition. In: Carlson, R.W. (Ed.), Treatise on Geochemistry. Elsevier, Amsterdam, pp. 1–38.

Pearson, D.G., Carlson, R.W., Shirey, S.B., Boyd, F.R., Nixon, P.H., 1995a. Stabilisation of Archaean lithospheric mantle: A Re–Os isotope study of peridotite xenoliths from the Kaapvaal craton. Earth Planet. Sci. Lett. 134, 341–357.

Pearson, N.J., O'Reilly, S.Y., Griffin, W.L., 1995b. The crust-mantle boundary beneath cratons and craton margins: A transect across the south-west margin of the Kaapvaal craton. Lithos 36, 257–287.

Poli, S., 1993. The amphibolite-eclogite transformation: an experimental study on basalt. Am. J. Sci. 2983, 1061–1107.

Pretorius, W., Barton Jr., J.M., 2003. Petrology and geochemisty of crustal and upper mantle xenoliths from the Venetia Diamond Mine – evidence for Archean crustal growth and subduction. South African J. Geol. 106, 213–230.

Pyle, J.M., Haggerty, S.E., 1998. Eclogites and the metasomatism of eclogites from the Jagersfontein kimberlite: punctuated transport and implications for alkali magmatism. Geochim. Cosmochim. Acta 62, 1207–1231.

Rader, E., Emry, E., Schmerr, N., Frost, D., Cheng, C., Menard, J., Yu, C.-Q., Geist, D., 2015. Characterization and Petrological Constraints of the Midlithospheric Discontinuity. Geochem. Geophys. Geosyst. 16, 3484–3504.

Rapp, R.P., Watson, E.B., 1999. Dehydration melting of metabasalt at 8-32 kbar: Implications for continental growth and crust-mantle recycling. J. Petrol. 36, 891–931.

Ravna, E.K., 2000. Distribution of Fe^{2+} and Mg between coexisting garnet and hornblende in synthetic and natural systems: an empiracle calibration of the garnet–hornblende Fe–Mg geothermometer. Lithos 53, 265–277.

Rehfeldt, T., Foley, S.F., Jacob, D.E., Carlson, R.W., Lowry, D., 2008. Contrasting types of metasomatism in dunite, wehrlite and websterite xenoliths from Kimberley, South Africa. Geochim. Cosmochim. Acta 72, 5722–5756.

Richardson, S.H., Shirey, S.B., 2008. Continental mantle signature of Bushveld magmas and coeval diamonds. Nature 453 (7197), 910–913.

Rychert, C.A., Shearer, P.M., 2009. A Global View of the Lithosphere-Asthenosphere Boundary. Science 324, 495–498.

Savage, B., Silver, P.G., 2008. Evidence for a compositional boundary within the lithospheric mantle beneath the Kalahari craton from S receiver functions. Earth Planet. Sci. Lett. 272, 600–609.

Schmickler, B., Jacob, D.E., Foley, S.F., 2004. Eclogite xenoliths from the Kuruman kimberlites, South Africa: geochemical fingerprinting of deep subduction and cumulate processes. Lithos 75, 173–207.

Schmidberger, S.S., Francis, D., 2001. Constraints on the trace element composition of the Archean mantle root beneath Somerset Island, Arctic Canada. J. Petrol. 42, 1095–1117.

Schmidberger, S.S., Heaman, L.M., Simonetti, A., Creaser, R.A., Cookenboo, H.O., 2005. Formation of Paleoproterozoic eclogitic mantle, Slave Province (Canada): Insights from in-situ Hf and U-Pb isotopic analyses of mantle zircons. Earth Planet. Sci. Lett. 240, 621–633.

Schmidberger, S.S., Simonetti, A., Heaman, L.M., Creaser, R.A., Whiteford, S., 2007. Lu–Hf, in-situ Sr and Pb isotope and trace element systematics for mantle eclogites from the Diavik diamond mine: Evidence for Paleoproterozoic subduction beneath the Slave craton. Canada. Earth Planet. Sci. Lett. 254, 55–68.

Schmidt, M.W., Poli, S., 2014. Devolatilization during subduction. In: Rudnick, R.L. (Ed.), The crust, 2nd edn, Treatise on geochemistry. Elsevier, Amsterdam, pp. 669–701.

Schmitz, M.D., Bowring, S.A., 2000. The significance of U-Pb zircon dates in lower crustal xenoliths from the southwestern margin of the Kaapvaal craton, southern Africa. Chem. Geol. 172, 59–76.

Schmitz, M.D., Bowring, S.A., 2003. Constraints on the thermal evolution of continental lithosphere from U-Pb accessory mineral thermochronology of lower crustal xenoliths, southern Africa. Contrib. Mineral. Petrol. 144, 592–618.

Schmitz, M.D., Bowring, S.A., de Wit, M.J., Gartz, V., 2004. Subduction and terrane collision stabilize the western Kaapvaal craton tectosphere 2.9 billion years ago. Earth Planet. Sci. Lett. 222, 363–376.

Schulze, D.J., Valley, J.W., Spicuzza, M.J., DeR Channer, D.R., 2003. Oxygen isotope composition of eclogitic and peridotitic garnet xenocrysts from the La Ceniza kimberlite, Guaniamo, Venezuela. Int. Geol. Rev. 45, 968–975.

Selway, K., Ford, H., Kelemen, P., 2015. The seismic mid-lithosphere discontinuity. Earth Planet. Sci. Lett. 414, 45–57.

Sen, C., Dunn, T., 1994. Dehydration melting of a basaltic composition amphibolite at 1.5 and 2.0 GPa: implications for the origin of adakits. Contrib. Mineral. Petrol. 117, 394–409.

Shaikh, A.M., Tappe, S., Bussweiler, Y., Patel, S.C., Ravi, S., Bolhar, R., Viljoen, F., 2020. Clinopyroxene and garnet mantle cargo in kimberlites as probes of Dharwar Craton architecture and geotherms, with implications for post-1.1 Ga lithosphere thinning events beneath southern India. J. Petrol 61 egaa087.

Shirey, S.B., Richardson, S.B., Harris, J.W., 2004. Integrated models of diamond formation and craton evolution. Lithos 77, 923–944.

Shirey, S.B., Carlson, R.W., Richardson, S.H., Menzies, A., Gurney, J.J., Pearson, D.G., Harris, J.W., Wiechert, U., 2001. Archean emplacement of eclogitic components into the lithospheric mantle during formation of the Kaapvaal Craton. Geophys. Res. Lett. 28, 2509–2512.

Shu, Q., Brey, G.P., 2015. Ancient mantle metasomatism recorded in subcalcic garnet xenocrysts: Temporal links between mantle metasomatism, diamond growth and crustal tectonomagmatism. Earth Planet. Sci. Lett. 418, 27–39.

Shu, Q., Brey, G.P., Gerdes, A., Höfer, H.E., 2013. Geochronological and geochemical constraints on the formation and evolution of the mantle underneath the Kaapvaal craton: Lu-Hf and Sm-Nd systematics of subcalcic garnets from highly depleted peridotites. Geochim. Cosmochim. Acta 113, 1–20.

Shu, Q., Brey, G.P., Hoefer, H.E., Zhao, Z., Pearson, D.G., 2016. Kyanite/corundum eclogites from the Kaapvaal Craton: subducted troctolites and layered gabbros from the Mid- to Early Archean. Contrib. Mineral. Petrol. 171, 11.

Simon, N.S.C., Carlson, R.W., Pearson, D.G., Davies, G.R., 2007. The origin and evolution of the Kaapvaal cratonic lithospheric mantle. J. Petrol. 48, 589–625.

Simonetti, A., Heaman, L.M., Chacko, T., Banerjee, N.R., 2006. In situ petrographic thin section U-Pb dating of zircon, monazite, and titanite using laser ablation-MC-ICP-MS. Int. J. Mass Spectrom. 253, 87–97.

Skinner, E.M.W., 1989. Contrasting group I and group II kimberlite petrology: towards a genetic model for kimberlites. In: Ross, J. (Ed.), Kimberlites and related rocks. Geological Society of Australia, Sydney, N.S.W., Australia, pp. 528–544.

Slama, J., Kosler, J., Condon, D.J., Crowley, J.L., Gerdes, A., Hanchar, J.M., Horstwood, M.S.A., Morris, G.A., Nasdala, L., Norberg, N., Schaltegger, U., Schoene, B., Tubrett, M.N., Whitehouse, M.J., 2008. Plesovice zircon - A new natural reference material for U-Pb and Hf isotopic microanalysis. Chem. Geol. 249, 1–35.

Smart, K.A., Heaman, L.M., Chacko, T., Simonetti, A., Kopylova, M., Mah, D., Daniels, D., 2009. The origin of high-MgO diamond eclogites from the Jericho Kimberlite, Canada. Earth Planet. Sci. Lett. 284, 527–537.

Smart, K.A., Chacko, T., Simonetti, A., Sharp, Z.D., Heaman, L.M., 2014. A Record of Paleoproterozoic Subduction Preserved in the Northern Slave Cratonic Mantle: Sr-Pb-O Isotope and Trace-element Investigations of Eclogite Xenoliths from the Jericho and Muskox Kimberlites. J. Petrol. 55, 549–583.

Smart, K.A., Tappe, S., Simonetti, A., Simonetti, S.S., Woodland, A.B., Harris, C., 2017. Tectonic significance and redox state of Paleoproterozoic eclogite and pyroxenite components in the Slave cratonic mantle lithosphere, Voyageur kimberlite, Arctic Canada. Chem. Geol. 455, 98–119.

Smart, K.A., Tappe, S., Ishikawa, A., Pfänder, J.A., Stracke, A., 2019. K-rich hydrous mantle lithosphere beneath the Ontong Java Plateau: significance for the genesis of oceanic basalts and Archean continents. Geochim. Cosmochim. Acta 248, 311–342.

Smart, K.A., Tappe, S., Woodland, A.B., Greyling, D.R., Harris, C., Gussone, N., 2021. Constraints on Archean crust recycling and the origin of mantle redox variability from the $\delta^{44/40}$Ca - δ^{18}O – fO_2 signatures of cratonic eclogites. Earth Planet. Sci. Lett. 556, 116720.

Smith, C.B., 1983. Pb, Sr and Nd isotopic evidence for sources of southern African Cretaceous kimberlites. Nature 304, 51–54.

Smith, C.B., Allsop, H.L., Kramers, J.D., Hutchinson, G., Roddick, J.C., 1985. Emplacement ages of Jurassic-Cretaceous South African kimberlites by the Rb-Sr method on phlogopite and whole-rock samples. Transactions of the Geological Society of South Africa 88 (2), 249–266.

Sodoudi, F., Yuan, X., Kind, R., Lebedev, S., Adam, J.M.-C., Kästle, E., Tilmann, F., 2013. Seismic evidence for stratification in composition and anisotropic fabric within the thick lithosphere of the Kalahari Craton. Geochem. Geophys. Geosyst. 14, 5393–5412.

Sommer, H., Wan, Y., Kröner, A., 2013. Shrimp zircon ages and petrology of lower crustal granulite xenoliths from the Letseng-La Terae kimberlite, Lesotho: further evidence for a Namaqua-Natal connection. South African J. Geol. 116, 183–198.

Spandler, C., Hermann, J., Arculus, R., Mavrogenes, J., 2003. Redistribution of trace elements during prograde metamorphism from lawsonite blueschist to eclogite facies; implications for deep subduction-zone processes. Contrib. Mineral. Petrol. 146, 205–222.

Stacey, J.S., Kramers, J.D., 1975. Approximation of terrestrial lead isotope evolution by a two-stage model. Earth Planet. Sci. Lett. 26, 207–221.

Stagno, V., Frost, D.J., McCammon, C.A., Mohseni, H., Fei, Y., 2015. The oxygen fugacity at which graphite or diamond forms from carbonate-bearing melts in eclogitic rocks. Contrib. Mineral. Petrol. 169, 16.

Steiger, R.H., Jäger, E., 1977. Subcommission on geochronology: Convention on the use of decay constants in geo- and cosmochronology. Earth Planet. Sci. Lett. 36, 359–362.

Stern, R.J., 2005. Evidence from ophiolites, blueschists, and ultrahigh-pressure metamorphic terranes that the modern episode of subduction tectonics began in Neoproterozoic time. Geology 33, 557–560.

Stiefenhofer, J., Viljoen, K.S., Marsh, J.S., 1997. Petrology and geochemistry of peridotite xenoliths from the Letlhakane kimberlites. Botswana. Contrib. Mineral. Petrol. 127, 147–158.

Storey, C.D., Jeffries, T.E., Smith, M., 2006. Common lead-corrected laser ablation ICP-MS U-Pb systematics and geochronology of titanite. Chem. Geol. 227, 37–52.

Sun, J., Tappe, S., Kostrovitsky, S.I., Liu, C.-Z., Skuzovatov, S.Y., Wu, F.-Y., 2018. Mantle sources of kimberlites through time: A U-Pb and Lu-Hf isotope study of zircon megacrysts from the Siberian diamond fields. Chem. Geol. 479, 228–240.

Tappe, S., Simonetti, A., 2012. Combined U-Pb geochronology and Sr-Nd isotope analysis of the Ice River perovskite standard, with implications for kimberlite and alkaline rock petrogenesis. Chem. Geol. 304-305, 10–17.

Tappe, S., Jenner, G.A., Foley, S.F., Heaman, L., Besserer, D., Kjarsgaard, B.A., Ryan, B., 2004. Torngat ultramafic lamprophyres and their relation to the North Atlantic Alkaline Province. Lithos 76, 491–518.

Tappe, S., Smart, K.A., Pearson, D.G., Steenfelt, A., Simonetti, A., 2011. Craton formation in Late Archean subduction zones revealed by first Greenland eclogites. Geology 39, 1103–1106.

Tappe, S., Romer, R.L., Stracke, A., Steenfelt, A., Smart, K.A., Muehlenbachs, K., Torsvik, T., 2017. Sources and mobility of carbonate melts beneath cratons, with implications for deep carbon cycling, metasomatism and rift initiation. Earth Planet. Sci. Lett. 466, 152–167.

Tappe, S., Smart, K.A., Torsvik, T.H., Massuyeau, M., de Wit, M.C.J., 2018a. Geodynamics of kimberlites on a cooling Earth: Clues to plate tectonic evolution and deep volatile cycles. Earth Planet. Sci. Lett. 484, 1–14.

Tappe, S., Dongre, A., Liu, C.-Z., Wu, F.-Y., 2018b. 'Premier' evidence for prolonged kimberlite pipe formation and its influence on diamond transport from deep Earth. Geology 46, 843–846.

Tappe, S., Stracke, A., van Acken, D., Strauss, H., Luguet, A., 2020. Origins of kimberlites and carbonatites during continental collision – Insights beyond decoupled Nd-Hf isotopes. Earth Sci. Rev. 208, 103287.

Tappe, S., Massuyeau, M., Smart, K.A., Woodland, A.B., Gussone, N., Milne, S., Stracke, A., 2021. Sheared peridotite and megacryst formation beneath the central Kaapvaal craton: Snapshots of tectonomagmatic processes across the lithosphere–asthenosphere transition. J. Petrol. accepted manuscript.

Tharimena, S., Rychert, C.A., Harmon, N., 2016. Seismic imaging of a mid-lithospheric discontinuity beneath Ontong Java Plateau. Earth Planet. Sci. Lett. 450, 62–70.

Thybo, H., 2006. The heterogeneous upper mantle low velocity zone. Tectonophys. 416, 53–79.

Tiepolo, M., Vannucci, R., Oberti, R., Foley, S., Bottazzi, P., Zanetti, A., 2000. Nb and Ta incorporation and fractionation in titanian pargasite and kaersutite: crystal–chemical constraints and implications for natural systems. Earth Planet. Sci. Lett. 175, 185–201.

Timmerman, S., Koornneef, J.M., Chinn, I.L., Davis, G.R., 2017. Dated eclogitic diamond growth zones reveal variable recycling of crustal carbon through time. Earth Planet. Sci. Lett. 463, 178–188.

van Achterbergh, E., Ryan, C., Jackson, S., Griffin, W.L., 2001. Laser-Ablation-ICPMS in the Earth Sciences - Appendix 3 data reduction software for LA-ICP-MS. In: Sylvester, P. (Ed.), Mineralogical Association of Canada Short Course, 29, pp. 239–243.

Van Calsteren, P.W.C., Harris, N.B.W., Hawkesworth, C.J., Menzies, M.A., Rogers, N.W., 1986. Xenoliths from southern Africa: a perspective on the lower crust. In: Dawson, J.B., et al. (Eds.), The Nature of the Lower Continental Crust, Spec. Publ. Geol. Soc. Lond, 24, pp. 351–362.

Vermeesch, P., 2018. IsoplotR: a free and open toolbox for geochronology. Geosci. Front. 9, 1479–1493.

Walker, R.J., Carlson, R.W., Shirey, S.B., Boyd, F.R., 1989. Os, Sr, Nd, and Pb isotope systematics of southern African peridotite xenoliths: Implications for the chemical evolution of subcontinental mantle. Geochim. Cosmochim. Acta 53, 1583–1595.

Wittlinger, G., Farra, V., 2007. Converted waves reveal a thick and layered tectosphere beneath the Kalahari super-craton. Earth Planet. Sci. Lett. 254, 404–415.

Wölbern, I., Rümpker, G., Link, K., Sodoudi, F., 2012. Melt infiltration of the lower lithosphere beneath the Tanzania craton and the Albertine rift inferred from S receiver functions. Geochem. Geophys. Geosyst. 13, 1–20.

Wood, B.J., Bryndzia, T., Johnson, K.E., 1990. Mantle oxidation state and its relationship to tectonic environment and fluid speciation. Science 248, 337–345.

Woodhead, J., Hergt, J., Giuliani, A., Phillips, D., Maas, R., 2017. Tracking continental-scale modification of the Earth's mantle using zircon megacrysts. Geochemical Perspectives Letters 4, 1–4.

Woodland, A.B., Koch, M., 2003. Variation in oxygen fugacity with depth in the upper mantle beneath the Kaapvaal craton, Southern Africa. Earth Planet. Sci. Lett. 214 (1–2), 295–310.

Woodland, A.B., Ross, C.R., 1994. A Crystallographic and Mössbauer Spectroscopy Study of $Fe_3^{2+}Al_2Si_3O_{12}$- $Fe_3^{2+}Si_3O_{12}$, (Almandine-"Skiagite") and $Ca_3Fe_2^{3+}Si_3O_{12}$- $Fe_3^{2+}Fe_2^{3+}Si_3O_{12}$ (Andradite-"Skiagite") Garnet Solid Solutions. Phys. Chem. Miner. 117–132.

Xiong, X.-L., 2006. Trace element evidence for growth of early continental crust by melting of rutile-bearing hydrous eclogite. Geology 34, 945–948.

Yaxley, G.M., Sobolev, A.V., 2007. High-pressure partial melting of gabbro and its role in the Hawaiian magma source. Contrib. Mineral. Petrol. 154, 371–383.

Yaxley, G.M., Berry, A.J., Rosenthal, A., Woodland, A.B., Paterson, D., 2017. Redox preconditioning deep cratonic lithosphere for kimberlite genesis – evidence from the central Slave Craton. Sci. Rep. 7, 1–10.

Yuan, H., Romanowicz, B., 2010. Lithospheric layering in the North American craton. Nature 466, 1063–1068.

Zack, T., Foley, S.F., Jenner, G.A., 1997. A consistent partition coefficient set for clinopyroxene, amphibole and garnet from laser ablation microprobe analysis of garnet pyroxenites from Kakanui, New Zealand. N. Jb. Miner. Abh. 172, 23–41.

Zack, T., Kronz, A., Foley, S.F., Rivers, T., 2002. Trace element abundances in rutiles from eclogites and associated garnet mica schists. Chem. Geol. 184, 97–122.

Zanetti, A., Vannucci, R., Bottazzi, P., Oberti, R., Ottolini, L., 1996. Infiltration metasomatism at Lherz as monitored by systematic ion-microprobe investigations close to a hornblendite vein. Chem. Geol. 134, 113–133.

Zeh, A., Ovtcharova, M., Wilson, A.H., Schaltegger, U., 2015. The Bushveld Complex was emplaced and cooled in less than one million years–results of zirconology, and geotectonic implications. Earth Planet. Sci. Lett. 418, 103–114.